RHEOLOGY AND MAGNETIZATION OF DILUTE EMULSIONS OF SURFACTANT-COVERED FERROFLUID DROPLETS

Por: Paulo Henrique Neves Pimenta

Tese de doutorado
Doutorado em Ciências Mecânicas

Brasília, 19 de janeiro de 2023.

UNIVERSIDADE DE BRASÍLIA

Faculdade de Tecnologia
Departamento de Engenharia Mecânica

UNIVERSIDADE DE BRASÍLIA
FACULDADE DE TECNOLOGIA
DEPARTAMENTO DE ENGENHARIA MECÂNICA

RHEOLOGY AND MAGNETIZATION OF DILUTE EMULSIONS OF SURFACTANT-COVERED FERROFLUID DROPLETS

Paulo Henrique Neves Pimenta

Orientador: Taygoara Felamingo de Oliveira, Prof. Dr., UnB

TESE DE DOUTORADO

PUBLICAÇÃO: ENM.DM - XXX.XXX

BRASÍLIA/DF: 19 de janeiro de 2023

UNIVERSIDADE DE BRASÍLIA
FACULDADE DE TECNOLOGIA
DEPARTAMENTO DE ENGENHARIA MECÂNICA

Rheology and magnetization of dilute emulsions of surfactant-covered ferrofluid droplets

Paulo Henrique Neves Pimenta

TESE DE DOUTORADO SUBMETIDA AO DEPARTAMENTO DE ENGENHARIA MECÂNICA DA FACULDADE DE TECNOLOGIA DA UNIVERSIDADE DE BRASÍLIA COMO REQUISITO PARCIAL PARA A OBTENÇÃO DO GRAU DE DOUTOR EM CIÊNCIAS MECÂNICAS.

APROVADA POR:

Taygoara Felamingo de Oliveira, Prof. Dr., UnB
(Orientador)

Cássio Machiaveli Oishi, Prof. Dr., UNESP
(Examinador Externo)

Francisco José de Souza, Prof. Dr., UFU
(Examinador Externo)

Adriano Possebon Rosa, Prof. Dr., UnB
(Examinador Interno)

BRASÍLIA/DF, 19 DE JANEIRO DE 2023.

FICHA CATALOGRÁFICA

Pimenta, P. H. N.
Rheology and magnetization of dilute emulsions of surfactant-covered ferrofluid droplets
[Distrito Federal] 2023.
xxvi, 105p. (ENM/FT/UnB, Doutor, Doutorado em Ciências Mecânicas, 2023.
Tese de doutorado - Universidade de Brasília.
Faculdade de Tecnologia.
Departamento de Engenharia Mecânica.
Palavras-chave:

1. Surfactant	2. Magnetic field
3. Rheology	4. Level set
5. Closest point	
I. ENM/FT/UnB	II. Título (série)

REFERÊNCIA BIBLIOGRÁFICA

Pimenta, P. H. N.(2023). Rheology and magnetization of dilute emulsions of surfactant-covered ferrofluid droplets. Tese de doutorado, Publicação ENM.DM - XXX.XXX, Departamento de Engenharia Mecânica, Universidade de Brasília, Brasília, Distrito Federal, xxvi, 105p.

CESSÃO DE DIREITOS

NOME DO AUTOR: Paulo Henrique Neves Pimenta.

TÍTULO DA TESE DE DOUTORADO: Rheology and magnetization of dilute emulsions of surfactant-covered ferrofluid droplets.

GRAU / ANO: DOUTOR / 2023

Paulo Henrique Neves Pimenta

I DEDICATE,

To my father, Alfredo Cezar de Moraes Pimenta, and my mother, Rozileide de Faria Neves Pimenta, who educated me and made this achievement possible, fundamental examples to my personal and professional life. Mainly to my wife, Caroline Tavares Silva Pimenta, and my sons, Pedro Henrique Tavares Pimenta, and Laura Tavares Pimenta, for all their support in difficult moments and motivation to overcome all difficulties.

Acknowledgements

To all Professors of the Graduate Program in Mechanical Sciences at the University of Brasília who contributed to the realization of this work, especially to the Professors of the Energy and Environment Laboratory.

To the Federal Institute of Goiás for releasing my professor activities to dedicate myself exclusively to this work.

To my supervisor Prof. Dr. Taygoara Felamingo de Oliveira for the opportunity given, teachings, trust in my work, great patience, and above all for the friendship built during all these years.

To my parents, Alfredo Cezar de Moraes Pimenta and Rozileide de Faria Neves Pimenta, for the examples and teachings throughout my life.

And mainly to my wife, Caroline Tavares Silva Pimenta, for their unconditional support and understanding throughout the work performed.

Resumo

Reologia e magnetização de emulsões diluídas de gotas de ferrofluido cobertas por surfactante

Autor: Paulo Henrique Neves Pimenta

Orientador: Taygoara Felamingo de Oliveira, Prof. Dr., UnB

Doutorado em Ciências Mecânicas

Brasília, 2023

Neste trabalho, estudamos os efeitos combinados da elasticidade (E), do fator de cobertura (X) do surfactante, do número de Péclet (Pe) e do campo magnético no escoamento em escala de gotas, além de seus impactos na reologia da emulsão e na magnetização média do sistema. Nossa análise considera uma única gota bidimensional coberta por surfactante de um ferrofluido superparamagnético suspenso em um líquido imiscível e não magnetizável, confinado em um canal entre placas paralelas. O sistema é submetido simultaneamente a um cisalhamento simples e a um campo magnético externo uniforme. Uma metodologia alternativa é proposta aqui, combinando o método *level set*, para capturar a interface, e o método *closest point* para resolver a equação de transporte do surfactante. Separamos as contribuições das fases diluídas para a viscosidade da emulsão em: *viscosidade capilar* [η_c], associada ao salto de tensão normal, a *viscosidade de Marangoni* [η_m], relacionada à tensão tangente à interface, e a *viscosidade magnética* [η_{mag}], ligado à intensidade do campo magnético. Além disso, quando a gota é submetida a um campo externo, também separamos as partes simétrica e antissimétrica do tensor de tensões $\langle \boldsymbol{\sigma} \rangle$, dividindo a viscosidade da emulsão em duas contribuições distintas: viscosidade de cisalhamento [η_s] e rotacional [η_r], respectivamente. Nossos resultados mostram que, na ausência de campo magnético, E e X afetam a forma das gotas mais intensamente do que Pe. Por outro lado, Pe afeta diretamente a viscosidade da emulsão. Para $Pe \gg 1$, a viscosidade capilar diminui com X, enquanto a viscosidade Marangoni cresce com X. Tal mecanismo de compensação permite o aumento da viscosidade da emulsão com X. Apresentamos também resultados para a primeira diferença de tensões normais. Na presença de um campo magnético, o comportamento reológico da emulsão é fortemente alterado, principalmente em regimes

puramente advectivos ($Pe \gg 1$), onde o tensoativo é varrido, não mais para as pontas das gotas, mas para regiões posteriores ou anteriores, dependendo da direção do campo. Este comportamento, somado ao alinhamento das gotas em relação ao escoamento, resulta em grandes variações da reologia do sistema, principalmente da viscosidade de Marangoni, uma vez que os locais das gotas de maior $\nabla_s\sigma$ estão em regiões de alta e baixa taxa de cisalhamento local, respectivamente, quando o campo magnético é perpendicular e paralelo à direção do escoamento. Verificamos que embora as tensões de Marangoni não tenham efeito sobre a viscosidade rotacional, $[\eta_r] \neq [\eta_{mag}]$ and $[\eta_s] \neq [\eta_c] + [\eta_m]$. A diferença entre $[\eta_r]$ e $[\eta_{mag}]$ aumenta com a intensidade do campo magnético e X. Por sua vez, a distribuição do surfactante ao longo da superfície da gota tem um efeito maior na viscosidade de cisalhamento, aumentando-a à medida que Pe e X aumentam. Em relação à magnetização média do sistema, nossos resultados mostram que $|\mathbf{M}^*|$ é uma função mais forte do comprimento projetado na direção do campo externo, onde as variações ao longo da faixa X são devidas à forma da gota. Finalmente, mostramos que a magnitude do torque magnético aumenta com X quando o campo magnético é perpendicular e quando o campo é paralelo, X tem pequeno efeito sobre o torque magnético.

Palavras-chaves: Surfactante; Campo magnético; Reologia; *Level set*; *Closest point*.

Abstract

Rheology and magnetization of dilute emulsions of surfactant-covered ferrofluid droplets

Author: Paulo Henrique Neves Pimenta

Supervisor: Taygoara Felamingo de Oliveira, Prof. Dr., UnB

PhD in Mechanical Sciences

Brasília, 2023

In this work, we study the combined effects of surfactant elasticity (E), coverage factor (X), Péclet number (Pe), and the magnetic field on the flow at droplet's scale, in addition to its impacts on the emulsion's rheology and the mean magnetization of the system. Our analysis considers a single two-dimensional surfactant-covered droplet of a superparamagnetic ferrofluid suspended in an immiscible, non-magnetizable liquid confined in a channel between parallel plates. The system is simultaneously subjected to a simple shear flow and an external uniform magnetic field. An alternative methodology is proposed here, combining the level set method, to capture the interface and the closest point method to solve the surfactant transport equation. We separate the dilute phase contribution to emulsion viscosity in the *capillary viscosity* [η_c], associated to the normal stress jump, the *Marangoni viscosity* [η_m], related to the stress tangent to the interface, and the *magnetic viscosity* [η_{mag}], linked to the magnetic field intensity. In addition, when the droplet is subjected to an external field, we also separate the symmetric and antisymmetric parts of the stress tensor $\langle \boldsymbol{\sigma} \rangle$, dividing the emulsion viscosity into two distinct contributions: shear [η_s] and rotational [η_r] viscosities, respectively. Our results show that, in the absence of a magnetic field, E and X affect the droplet shape more intensely than the Pe. On the other hand, Pe directly affects the emulsion's bulk viscosity. For $Pe \gg 1$, the capillary viscosity decreases with X, while the Marangoni viscosity grows with X. Such a compensation mechanism allows the increase of the bulk viscosity with X. We also present results for the first normal stress difference. In the presence of a magnetic field, the emulsion rheological behavior is strongly altered, mainly in purely advective regimes ($Pe \gg 1$), where the surfactant is swept, no longer to the droplet tips, but to posterior or anterior regions to

these locations, depending on the direction of the field. This behavior added to the droplet alignment in relation to the flow, results in large variations of the system rheology, mainly regarding the Marangoni viscosity, since the droplet locations of larger $\nabla_s\sigma$ are in regions of high and low local shear rate when the magnetic field is perpendicular and parallel to the main flow direction, respectively. We found that, although Marangoni stresses have no effect on the rotational viscosity, however $[\eta_r] \neq [\eta_{mag}]$ and $[\eta_s] \neq [\eta_c] + [\eta_m]$. The difference between $[\eta_r]$ and $[\eta_{mag}]$ increases with the strength of the magnetic field and X. Additionally, the surfactant distribution along the droplet surface has a larger effect on shear viscosity, increasing it as Pe and X increase. Regarding the system mean magnetization, our results showed that $|\mathbf{M}^*|$ is a stronger function of the length projected in the direction of the external field, where the variations along of X range are due to the droplet shape. Finally, we show that the magnetic torque magnitude increases with X when the magnetic field is perpendicular and when the magnetic field is parallel, X has a small effect on the magnetic torque.

Keywords: Surfactant; Magnetic field; Rheology; Level set; Closest point.

Summary

1 INTRODUCTION 1
1.1 Objectives 10
1.2 Scope of the work 11

2 FORMULATION 12
2.1 Problem statement 12
2.1.1 Superparamagnetic emulsions 13
2.2 The governing equations 14
2.2.1 Surfactant transport 16
2.3 Model normalization 17
2.4 Bulk stress on a surfactant-covered droplet emulsion 18
2.5 Bulk magnetization of the emulsion 20
2.6 Magnetic emulsion viscosity 21

3 NUMERICAL METHODOLOGY 23
3.1 Finite difference method 23
3.2 Level set method 26
3.3 Closest point method 30
3.4 Coupling the level set method with the governing equations . . 32
3.5 Magnetic potential field numerical solution 33
3.6 Projection method 34
3.6.1 Spatial discretization of the projection method 36
3.7 Boundary and initial conditions 40
3.8 Surfactant concentration 43
3.9 Numerical methodology to compute the droplet shape 45

4 RESULTS AND DISCUSSIONS 47
4.1 Non-magnetic surfactant-covered droplets 47
4.1.1 Convergence rate and droplet shape comparison with results from the literature 48

4.1.2 Surfactant concentration and forces on the interface 48
4.1.3 Influence of the surfactant's elasticity and coverage factor in the droplet shape 51
4.1.4 Effects of the surfactant coverage, elasticity, and Péclet number on the emulsion's rheology 53
4.1.5 Surfactant-covered droplets first normal stress difference 56
4.2 Surfactant-covered ferrofluid droplets under external magnetic field 57
4.2.1 Surfactant-free ferrofluid droplet 58
4.2.2 Effects of the magnetic field and surfactants on the surface properties 61
4.2.3 Effects of the surfactant and magnetic field in the droplet shape . 66
4.2.4 Combined effect of surfactant and magnetic field on the emulsion rheology 69
4.2.4.1 Marangoni viscosity 69
4.2.4.2 Capillary viscosity 71
4.2.4.3 Magnetic viscosity 75
4.2.4.4 Reduced viscosity 76
4.2.4.5 Shear and rotational viscosities 78
4.2.5 Combined effect of surfactant and magnetic field on the emulsion magnetization 81

5 CONCLUSIONS 83

BIBLIOGRAPHY 86

APPENDIX 94

APPENDIX A – - SUGGESTION TO FUTURE WORK: MAGNETIC VESICLES 95
A.1 Physics formulation 96
A.2 Vesicles equations normalization 98
A.3 Projection method for magnetic vesicles 99
A.4 Implementation difficulties/suggestions 101

ANNEX 102

ANNEX A – - DIRECT SOLUTION VIA FOURIER ANALYSIS . . 103

ANNEX B – - BICONJUGATE GRADIENT METHOD 105

List of Figures

Figure 1 – Schematic illustration of a surfactant-covered droplet under simple shear flow. Ω_2 corresponds to the droplet region and Ω_1 corresponds to the continuous phase, Γ is the the interface, η is the continuous phase viscosity, $\lambda\eta$ is the droplet viscosity, ρ is the droplet and continuous phase density, a is the droplet radius, $\dot{\gamma}$ is the shear rate, c is the surfactant concentration, $U_n = \dot{\gamma}H_p/2 = -U_s$ is the canal walls velocity, $\mathbf{H}_0$ is the external uniform magnetic field ,H_p is the distance between the channel walls, and L is the length of the channel walls. 13

Figure 2 – Surface element used to derive equations at surface. $\hat{\mathbf{b}}$ is the unit binormal vector, $\hat{\mathbf{t}}$ is the unit tangential vector and $\hat{\mathbf{n}}$ is the unit normal vector. C represents the contour and dS is the finite surface element. . 15

Figure 3 – Staggered grid and cell structures. Vector components in the x and y directions are stored, respectively, at the empty squares and circles. Scalar quantities are stored at the black circles. 24

Figure 4 – One-dimensional discretization domain for finite difference method. . . 24

Figure 5 – Representation of the level set function. 26

Figure 6 – Representation of the local level set method. 28

Figure 7 – Closest point method: a geometrical representation. Yellow dots are grid points with their corresponding closest point on the surface as white square dots. Dots into the blue region are used for interpolation of the surface property value (white square dot). The interface normal vectors are drawn as arrow ended segments. 31

Figure 8 – Right boundary. The red dots correspond to points outside the domain, but which are used to solve Eq. (3.41). 34

Figure 9 – Upper and lower boundaries. The red dots correspond to points outside the solution domain, but which are used to solve the governing equations. 40

Figure 10 – Left and right boundaries. The red dots correspond to points outside the domain, but which are used to solve the governing equations. As in these boundaries, the boundary conditions are periodic, and the dots that are inside and outside the domain are inverted from one side to another. 42
Figure 11 – Geometrical representation of the droplet measure. Each yellow dot on the surface corresponds to an angle θ_i. 45
Figure 12 – Taylor deformation, D_T, as function of Ca for $X = 0.6$, $E = 0.1$ and $\alpha = Pe/Ca = 10$. Red curve and black line corresponds, respectively, to the present model and the work of Li and Pozrikidis (1997). The inset shows the dependence of the droplet inclination, θ, as functions of Ca. 49
Figure 13 – (a) Surfactant concentration and (b) surface tension coefficient over droplet surface for $Re = 10$, $Ca = 0.1$, $X = 0.6$, $E = 0.2$, $Pe = 10$ (red line), and $Pe = 1$ (blue line). The black dotted line corresponds to the work of Xu, Yang and Lowengrub (2012). The insets of (a) shows droplet contours colored by surfactant concentration for $Pe = 10$ and the droplet shapes for $Pe = 1$ and $Pe = 10$. 49
Figure 14 – Concentrated body forces for $Re = 10$, $Ca = 0.1$, $X = 0.6$, $E = 0.2$, $Pe = 10$ (red line), and $Pe = 1$ (blue line). (a) Signaled capillary force magnitude ($\mathbf{F}_c \cdot \hat{\mathbf{n}}$) and (b) signaled Marangoni force magnitude ($\mathbf{F}_m \cdot \hat{\mathbf{t}}$). The black dotted line corresponds to the work of Xu, Yang and Lowengrub (2012). The inset of (b) shows where $\mathbf{F}_m \cdot \hat{\mathbf{t}}$ is positive (red contour) or negative (black contour). 50
Figure 15 – (a) Taylor deformation parameter and (b) droplet inclination as functions of X for $E = 0.2$ (diamonds) and $E = 0.4$ (circles). $Pe = 10^3$ (red), $Pe = 1$ (green), and $Pe = 10^{-3}$ (blue). The insets show the variation of D_T and θ as functions of E for $X = 0.6$. 51
Figure 16 – Capillary viscosity (squares) and Marangoni viscosity (triangles) for (a) $E = 0.2$ and (b) $E = 0.4$. $Pe = 10^3$ (red), $Pe = 1$ (green), and $Pe = 10^{-3}$ (blue). The inset of (a) show the droplet contours colored by surfactant concentration for the same E and X. The inset of (b) show the parallel between the capillary viscosity and the reduced viscosity for $Pe = 10^{-3}$. 53
Figure 17 – Reduced viscosity as a function of X for (a) $E = 0.2$ and (b) $E = 0.4$. $Pe = 10^3$ (red), $Pe = 1$ (green), and $Pe = 10^{-3}$ (blue). The insets show droplets for all Péclet numbers. 54
Figure 18 – Stream lines and pressure field for $X = 0.6$, $E = 0.4$, (a) $Pe = 10^{-3}$, and (b) $Pe = 10^3$. 55
Figure 19 – (a) Capillary viscosity (squares) and Marangoni viscosity (triangles). (b) Reduced viscosity. $Pe = 10^3$, $X = 0.3$ (blue) and $X = 0.6$ (red). . . 56

Figure 20 – First normal stress difference as a function of X, for $E = 0.2$ (diamonds) and $E = 0.4$ (circles). $Pe = 10^3$ (red), $Pe = 1$ (green), and $Pe = 10^{-3}$ (blue). 57
Figure 21 – (a) Taylor deformation, (b) reduced viscosity, (c) normalized magnetic torque, and (d) normalized magnetization. The insets of (a), (c) and (d), show the droplet inclination, hydrodynamic torque, and the misalignment angle between the bulk magnetization and the external magnetic field, respectively. Circles and cross (+) correspond to parallel external field; squares and cross (×) correspond to perpendicular external field. Results of Cunha et al. (2020) are represented by circles and squares. . 59
Figure 22 – Droplet perimeter at steady state under perpendicular (red) and parallel (blue) external magnetic field for $Ca_{mag} = 0$ (crosses), $Ca_{mag} = 5$ (diamonds) and $Ca_{mag} = 10$ (circles), when $Pe = 10^3$ and $E = 0.2$. . . . 61
Figure 23 – Surfactant concentration under (a) vertical and (b) horizontal external magnetic field for $X = 0.3$ (dashed line) and $X = 0.6$ (continuous line), when $Pe = 10^3$, $E = 0.2$, $Ca_{mag} = 0$ (black), $Ca_{mag} = 5$ (green) and $Ca_{mag} = 10$ (red). The insets show droplets contours colored by surfactant concentration on a scale from (a) 0.1 (green) to 1.2 (red). . . 62
Figure 24 – Surface tension coefficient over droplet surface under (a) vertical and (b) horizontal external magnetic field for $X = 0.3$ (dashed line) and $X = 0.6$ (continuous line), when $Pe = 10^3$ and $E = 0.2$, $Ca_{mag} = 0$ (black), $Ca_{mag} = 5$ (green) and $Ca_{mag} = 10$ (red). 63
Figure 25 – Signaled Marangoni force magnitude under (a) vertical and (b) horizontal external magnetic field for $X = 0.3$ (dashed line) and $X = 0.6$ (continuous line), when $Pe = 10^3$, $E = 0.2$, $Ca_{mag} = 0$ (black), $Ca_{mag} = 5$ (green) and $Ca_{mag} = 10$ (red). The insets show droplets contours colored by Signaled Marangoni force on a scale from (a) -0.4 (blue) to 0.6 (red). 65
Figure 26 – Signaled capillary force magnitude under (a) vertical and (b) horizontal external magnetic field for $X = 0.3$ (dashed line) and $X = 0.6$ (continuous line), when $Pe = 10^3$, $E = 0.2$, $Ca_{mag} = 0$ (black), $Ca_{mag} = 5$ (green) and $Ca_{mag} = 10$ (red). The insets show droplets contours colored by Signaled capillary force on a scale from (a) -2.6 (red) to 0 (blue). . 66
Figure 27 – Taylor deformation and droplet inclination as functions of surfactant coverage X for $E = 0.2$. (a) and (c) perpendicular field, (b) and (d) parallel field; $Pe = 10^3$ (red), $Pe = 1$ (green), and $Pe = 10^{-3}$ (blue); $Ca_{mag} = 0$ (triangles), $Ca_{mag} = 5$ (squares), and $Ca_{mag} = 10$ (diamonds). 67
Figure 28 – Taylor deformation parameter as function of Ca_{mag} for $Pe = 10^3$ (red), $Pe = 1$ (green), and $Pe = 10^{-3}$ (blue) when $E = 0.4$, $X = 0.3$ (circles) $X = 0.6$ (diamonds), under (a) perpendicular and (b) parallel external magnetic field. The insets show the droplet inclination as function of Ca_{mag}. Black crosses corresponds to surfactant-free surface. 68

Figure 29 – Marangoni viscosity as function of (a) Ca_{mag} and (b) θ for $E = 0.4$, $X = 0.3$ (circles) and $X = 0.6$ (diamonds), $Pe = 10^{-3}$ (blue), $Pe = 1$ (green), and $Pe = 10^{3}$ (red) under a perpendicular external magnetic field. The insets show Marangoni viscosity as function of X, for $E = 0.2$, $Ca_{mag} = 0$ $(+)$, $Ca_{mag} = 5$ $(\times)$ and $Ca_{mag} = 10$ $(*)$; and some droplets contours colored by Signaled Marangoni force from -0.4 (blue) to 0.6 (red). 69
Figure 30 – Marangoni viscosity as function of (a) Ca_{mag} and (b) θ for $E = 0.4$, $X = 0.3$ (circles) and $X = 0.6$ (diamonds), $Pe = 10^{-3}$ (blue), $Pe = 1$ (green), and $Pe = 10^{3}$ (red) under a parallel external magnetic field. The insets show Marangoni viscosity as function of X, for $E = 0.2$, $Ca_{mag} = 0$ $(+)$, $Ca_{mag} = 5$ $(\times)$ and $Ca_{mag} = 10$ $(*)$; and some droplets contours colored by Signaled Marangoni force from -0.4 (blue) to 0.6 (red). 71
Figure 31 – Capillary viscosity as function of (a) Ca_{mag} and (b) D_T for $E = 0.4$, $X = 0.3$ (circles) and $X = 0.6$ (diamonds), $Pe = 10^{-3}$ (blue), $Pe = 1$ (green), and $Pe = 10^{3}$ (red) under a perpendicular external magnetic field. The insets show capillary viscosity as function of X, for $E = 0.2$, $Ca_{mag} = 0$ $(+)$, $Ca_{mag} = 5$ $(\times)$ and $Ca_{mag} = 10$ $(*)$; and some droplets contours colored by absolute capillary force from 0 (blue) to -2.6 (red). 72
Figure 32 – Capillary viscosity as function of (a) Ca_{mag} and (b) D_T for $E = 0.4$, $X = 0.3$ (circles) and $X = 0.6$ (diamonds), $Pe = 10^{-3}$ (blue), $Pe = 1$ (green), and $Pe = 10^{3}$ (red) under a parallel external magnetic field. The insets show capillary viscosity as function of X, for $E = 0.2$, $Ca_{mag} = 0$ $(+)$, $Ca_{mag} = 5$ $(\times)$ and $Ca_{mag} = 10$ $(*)$; and some droplets contours colored by absolute capillary force from 0 (blue) to -2.6 (red). 72
Figure 33 – Magnetic viscosity as function of (a) Ca_{mag} and (b) D_T for $E = 0.4$, $X = 0.3$ (circles) and $X = 0.6$ (diamonds), $Pe = 10^{-3}$ (blue), $Pe = 1$ (green), and $Pe = 10^{3}$ (red) under a perpendicular external magnetic field. The inset of (a) shows magnetic viscosity as function of X, for $E = 0.2$, $Ca_{mag} = 0$ $(+)$, $Ca_{mag} = 5$ $(\times)$ and $Ca_{mag} = 10$ $(*)$. 75
Figure 34 – Magnetic viscosity as function of (a) Ca_{mag} and (b) D_T for $E = 0.4$, $X = 0.3$ (circles) and $X = 0.6$ (diamonds), $Pe = 10^{-3}$ (blue), $Pe = 1$ (green), and $Pe = 10^{3}$ (red) under a parallel external magnetic field. The inset of (a) shows magnetic viscosity as function of X, for $E = 0.2$, $Ca_{mag} = 0$ $(+)$, $Ca_{mag} = 5$ $(\times)$ and $Ca_{mag} = 10$ $(*)$. 76
Figure 35 – (a) Reduced viscosity as function of Ca_{mag} for $E = 0.4$, $X = 0.3$ (circles) and $X = 0.6$ (diamonds). Black crosses corresponds to surfactant-free surface. (b) Reduced viscosity as function of X, for $E = 0.2$, $Ca_{mag} = 0$ $(+)$, $Ca_{mag} = 5$ $(\times)$ and $Ca_{mag} = 10$ $(*)$. Perpendicular field for $Pe = 10^{3}$ (red), $Pe = 1$ (green), and $Pe = 10^{-3}$ (blue). 77

Figure 36 – (a) Reduced viscosity as function of Ca_{mag} for $E = 0.4$, $X = 0.3$ (circles) and $X = 0.6$ (diamonds). Black crosses corresponds to surfactant-free surface. (b) Reduced viscosity as function of X, for $E = 0.2$, $Ca_{mag} = 0$ $(+)$, $Ca_{mag} = 5$ $(\times)$ and $Ca_{mag} = 10$ $(*)$. Parallel field for $Pe = 10^3$ (red), $Pe = 1$ (green), and $Pe = 10^{-3}$ (blue). 77
Figure 37 – Shear viscosity as functions of surfactant coverage, X, for $Pe = 10^3$ (red), $Pe = 1$ (green), and $Pe = 10^{-3}$ (blue) when $E = 0.2$, $Ca_{mag} = 0$ $(+)$, $Ca_{mag} = 5$ $(\times)$ and $Ca_{mag} = 10$ $(*)$. (a) and (b) correspond to perpendicular and parallel external magnetic field, respectively. 78
Figure 38 – Rotational viscosity as functions of surfactant coverage, X, for $Pe = 10^3$ (red), $Pe = 1$ (green), and $Pe = 10^{-3}$ (blue) when $E = 0.2$, $Ca_{mag} = 0$ $(+)$, $Ca_{mag} = 5$ $(\times)$ and $Ca_{mag} = 10$ $(*)$. (a) and (b) correspond to perpendicular and parallel external magnetic field, respectively. 79
Figure 39 – Difference between magnetic and rotational viscosities as functions of surfactant coverage, X, for $Pe = 10^3$ (red), $Pe = 1$ (green), and $Pe = 10^{-3}$ (blue) when $E = 0.2$, $Ca_{mag} = 0$ $(+)$, $Ca_{mag} = 5$ $(\times)$ and $Ca_{mag} = 10$ $(*)$. (a) and (b) correspond to perpendicular and parallel external magnetic field, respectively. 80
Figure 40 – Magnetization as function of surfactant coverage, X, for $Pe = 10^3$ (red), $Pe = 1$ (green), and $Pe = 10^{-3}$ (blue) when $E = 0.2$, $Ca_{mag} = 0$ $(+)$, $Ca_{mag} = 5$ $(\times)$ and $Ca_{mag} = 10$ $(*)$. (a) and (b) correspond to perpendicular and parallel external magnetic field, respectively. 81
Figure 41 – Magnetic torque as function of surfactant coverage, X, for $Pe = 10^3$ (red), $Pe = 1$ (green), and $Pe = 10^{-3}$ (blue) when $E = 0.2$, $Ca_{mag} = 0$ $(+)$, $Ca_{mag} = 5$ $(\times)$ and $Ca_{mag} = 10$ $(*)$. (a) and (b) correspond to perpendicular and parallel external magnetic field, respectively. The insets show the misalignment angle as function of X. 82
Figure 42 – Schematic illustration of a magnetic vesicle under simple shear flow. Ω_2 corresponds to the vesicle region and Ω_1 corresponds the continuous phase, Γ is the inextensible membrane, η is the continuous phase viscosity, $\lambda\eta$ is the vesicle viscosity, μ_0 is the continuous phase magnetic permeability, $\zeta\mu_0$ is the vesicle magnetic permeability, ρ is the vesicle and continuous phase density, $\dot{\gamma}$ is the shear rate $\dot{\gamma}$, $U_n = \dot{\gamma}H_p/2 = -U_s$ is the canal walls velocity, $\mathbf{H}_0$ is the external uniform magnetic field, H_p is the distance between the channel walls and L is the length of the channel walls. 96

List of Tables

Table 1 – Errors and convergence rate for the surfactant concentration at $t = 0.5$ for $X = 0.6$, $E = 0.2$, $\lambda = 1$, $Ca = 0.1$, $Pe = 10$ and $Re = 10$. 48
Table 2 – Average deviation for Taylor deformation, droplet inclination, reduced viscosity, normalized magnetic and hydrodynamics torque, normalized magnetization and angle between magnetic field and the emulsion's magnetization. 60

List of Algorithms

Algorithm 1 – : Biconjugate Gradient Stabilized method 105

List of abbreviations and acronyms

DEP	Dielectrophoresis
ENO	Essentially non-oscillatory
EOS	Equation of state
PDE	Partial differential equation
RBCs	Red blood cells
TVD	Total variation diminishing
WENO	Weighted essentially non-oscillatory

List of symbols

Latin symbols

A	Area
a	Not deformed droplet radius
$a_{i,j}$	Coefficient of the left node of the five-nodes stencil
$b_{i,j}$	Coefficient of the bottom node of the five-nodes stencil
b_n	Bending rigidity
$\mathbf{B}$	Magnetic induction
$\mathbf{b}$	Binormal vector
b_x	Binormal vector component in the x direction
b_y	Binormal vector component in the y direction
b_z	Binormal vector component in the z direction
C	Cut-off function
c	Surfactant concentration
c_∞	Surfactant concentration at the maximum packing
c_e	Initial average surfactant concentration
$c_{i,j}$	Coefficient of the center node of the five-nodes stencil
$(\mathbf{cp})$	Closest point
D_s	Surfactant diffusivity
D_T	Taylor deformation parameter
$d_{i,j}$	Coefficient of the right node of the five-nodes stencil
$e_{i,j}$	Coefficient of the upper node of the five-nodes stencil

E	Surfactant elasticity
$\mathbf{F}_b$	Bending Force
$\mathbf{F}_c$	Capillary force
$\mathbf{F}_m$	Marangoni force
$\mathbf{F}_{mag}$	Magnetic force
$\mathbf{F}_\sigma$	Force arising from the surface tension
$\mathbf{F}_s$	Singular force term
f	Generic continuous function used to describe the finite difference method
f'	first central differential derivatives
f''	Second central differential derivatives
$f_{i,j}$	Coefficient of the independent term of the five-nodes stencil
h	Cell size
H	Heavyside function
H_ε	Smoothed Heavyside function
H_p	Gap distance between the parallel plates
$\mathbf{H}$	Magnetic field
$\mathbf{H}_0$	External magnetic field
$\mathbf{I}$	Identity tensor
i	Cell counter in the horizontal direction
j	Cell counter in the vertical direction
k	Cell counter into the tube
L	Length of the channel walls
$\mathbf{L}$	Antisymmetric parts of the stress tensor
L_{yx}	Average shear stress of antisymmetric parts of the stress tensor on the two channel walls
$\mathbf{M}$	Magnetization
$\langle \mathbf{M} \rangle$	Bulk Magnetization

$\mathbf{n}$	Normal vector
n_x	Normal vector component in the x direction
n_y	Normal vector component in the y direction
n_z	Normal vector component in the z direction
N	Number of cells in a direction
N_x	Number of cells in the x direction
N_y	Number of cells in the y direction
$\mathcal{O}$	Order error
p	Pressure field
R	Constant of ideal gas
R_0	Characteristic length
S	Signed function
S_ε	Smoothed signed function
$\mathbf{S}$	Symmetric parts of the stress tensor
S_{yx}	Average shear stress of symmetric parts of the stress tensor on the two channel walls
t	Time
$\mathbf{t}$	Tangential vector
t_x	Tangential vector component in the x direction
t_y	Tangential vector component in the y direction
t_z	Tangential vector component in the z direction
T	Absolute temperature
$\mathbf{u}$	Velocity field
$\mathbf{u}_s$	Velocity field tangent to the interface
$\tilde{\mathbf{u}}$	Velocity field component extrapolated in time
$\mathbf{u}^*$	Intermediate velocity field
u	Velocity field component in the x direction

$\tilde{u}$	Velocity field component extrapolated on time in the x direction
u^*	Intermediate velocity field in the x direction
U_n	Top plate dislocation velocity
U_s	Bottom plate dislocation velocity
v	Velocity field component in the y direction
$\tilde{v}$	Velocity field component extrapolated on time in the y direction
v^*	Intermediate velocity field in the y direction
V	Volume
$\mathbf{x}$	Eulerian position vector
x	Position components in x-direction
$\mathbf{x}_\Gamma$	Closest point at the interface to a given point
w	Velocity field component in the z direction
y	Position components in y-direction
z	Position components in z-direction

Greek symbols

α	Generic two-dimensional scalar function
β_v	Dispersed to continuum phases volume fraction
Γ	Fluids interface or vesicle membrane
$\dot{\gamma}$	Shear rate
Δt	Time step
Δx	Cell size in the horizontal direction
Δy	Cell size in the vertical direction
$\Delta \tau$	Pseudo-time step
δ	Dirac delta function
δ_ε	Smoothed Dirac delta function
ϵ_1	First tube thickness

ϵ_2	Second tube thickness
ϵ_3	Third tube thickness
ε	Half of the artificial interface thickness
$\boldsymbol{\varepsilon}$	Levi-Civita permutation tensor
ζ	Magnetic permeability ratio between the ferrofluid and the free space
ζ_ε	Smoothed magnetic permeability ratio
η	Continuous phases viscosity
η_{eff}	Effective viscosity
η_ε	Smoothed viscosity ratio
$[\eta]$	Reduced viscosity
$[\eta_c]$	Capillary viscosity
$[\eta_m]$	Marangoni viscosity
$[\eta_{mag}]$	Magnetic viscosity
$[\eta_r]$	Rotational viscosity
$[\eta_s]$	Shear viscosity
θ	Droplet inclination angle
θ_m	Misalignment angle between the bulk magnetization and the external magnetic field
κ	Curvature
λ	Viscosity ratio
λ_m	Mass correction function
μ	Magnetic permeability
μ_0	Free magnetic permeability
ρ	Fluids density
σ	Surface tension
σ_0	Surface tension of a clean interface
$\langle \boldsymbol{\sigma} \rangle$	Volume-averaged stress tensor

$\langle \sigma_{xy} \rangle$	Average shear stress on the two channel walls
τ	Pseudo-time
$\boldsymbol{\tau}_{mag}$	Magnetic torque per unit volume
$\boldsymbol{\tau}_{hyd}$	Hydrodynamic torque per unit volume
ϕ	Level set function
ϕ_τ	Derivative of level set function in pseudo-time
χ	Auxiliary variable to compute the pressure
χ_m	Magnetic susceptibility
ψ	Magnetic potential
Ω_1	Continuous phase domain
Ω_2	Dispersed phase domain
Ω_T	Tube region

Mathematical symbols

$\frac{D}{Dt}$	Material derivative operator
∇	Gradient operator
∇_s	Surface gradient operator
$\nabla\cdot$	Divergence operator
$\nabla_s\cdot$	Surface divergence operator
$\nabla\times$	Curl operator
∇^2	Laplace operator
∇_s^2	Surface Laplace operator
$\cdot$	Scalar product

Non-dimensional groups

Ca	Capillary number
Ca_{b_n}	Capillary bending number
Ca_{mag}	Magnetic capillary number

Ca_{bmag}	Magnetic capillary bending number
E	Surfactant elasticity
Pe	Péclet number
Re	Reynolds number
X	Surfactant coverage

1 Introduction

Multiphase immiscible fluid systems, such as emulsions, foams, vesicle suspensions, and polymer mixtures, are found in engineering applications of many industries, such as food, oil, biomedical, and plastics. During the processing of these systems, the droplets of the dispersed phase are deformed, fragmented, and oriented in the continuous phase, producing an evolving morphology or microstructure defined in part by the droplets' density and viscosity, size distribution, shape, and orientation. The final morphology of the system helps determine the material, mechanical, chemical, thermal, and sensory properties of the final product.

The study of individual droplets under different conditions, for example, in the presence of surfactants or under the influence of magnetic fields (in the case of magnetic emulsions), is a crucial step to improve and control processes involving multiphase fluid systems. Magnetic emulsions are two-phase mixtures that consist of ferrofluid droplets suspended in a non-magnetic, immiscible liquid. This class of fluid systems represents a promising alternative to other ordinary materials in many technological applications (CUNHA et al., 2020). The macroscopic behavior of these emulsions is a function of complex physical phenomena that occur at the microscopic level, such as droplet deformation, rotation, and breakup, which, in turn, are ruled by the combined action of hydrodynamic and magnetic effects (CUNHA et al., 2018). Thus, emulsions of ferrofluid droplets are complex fluids whose response under flow can be controlled by external magnetic fields.

The interest in applications of magnetic fields to manipulate suspensions of deformable particles is growing. In biomedicine, these applications cover studies ranging from the manipulation of DNA molecules (MARTÍNEZ-SANTIAGO; QUIÑONES, 2019; TAMBASCO et al., 2020), hemorheology of red blood cells (RBCs) (JO et al., 2018), to the selective manipulation and drug delivery (MONDAL; SHIT, 2017; HEDAYATI; RAMIAR; LARIMI, 2018; SODAGAR et al., 2021), as for example to treat diseases such as cancer tumors, where the drug is directed to the localized area of disease by using a magnetic field (SODAGAR; SHAKIBA; NIAZMAND, 2020; LI et al., 2021). In addition, several industrial and production processes use the magnetic field, either to stabilize the emulsion (JALILI DARBANDI SOFLA; NOROUZI-APOURVARI; SCHAFFIE, 2020) or to isolate a specific material that makes it up (such as the demulsification of water-in-oil emulsions (ROMANOVA et al., 2019; GUO et al., 2019). In some of these processes,

natural surfactants such as asphaltenes, resins, waxes, and similar can be found. Still, in most cases, surfactants are added to the emulsion to act as an emulsifier (SORGENTONE; TORNBERG; VLAHOVSKA, 2019). These surface active agents reduce the surface tension, facilitating emulsification (LIU et al., 2018) and stabilizing the emulsion by avoiding direct contact among droplets.

Surfactants are molecules that have a hydrophilic head and a hydrophobic tail, that tend to migrate to the interfaces in the flow (XU; SHI; LAI, 2018). The presence of these substances on the droplet surface alters the local thermodynamic environment and, consequently, the mathematical nature of the dynamic boundary conditions. Surfactants might be soluble if their molecules can dissolve into the liquid around the interface, or insoluble if the surfactant's mass on the surface is conserved. The balance between diffusion and advection of insoluble surfactants produces surface tension gradients associated with Marangoni stresses (KRUIJT-STEGEMAN; VOSSE; MEIJER, 2004) which, like the droplets' shape and orientation, has a direct influence on the emulsion's rheology. It is well-known that parameters like concentration, viscosity ratio, density ratio, and droplet size distribution influence the mechanical behavior of surfactant-covered droplet emulsions (MILLIKEN; STONE; LEAL, 1992; LI; POZRIKIDIS, 1997; XU et al., 2006). However, the surfactant effects on the emulsion's rheology still require more thorough investigation, even more so when it comes to ferrofluid droplet emulsions subjected to magnetic fields. This is an unexplored subject, although individually, both the effects of surfactants and magnetic fields on droplet dynamics have been extensively studied.

There is a growing interest in the complex dynamics of ferrofluid emulsions under the influence of an external magnetic field and the hydrodynamic flow. Ahmed, Fleck and Waghmare (2018) presented a theoretical and experimental study of the effects of an external magnetic field on the maximum spreading of a ferrofluid droplet impacting a solid substrate. Jesus, Roma and Ceniceros (2018) used three-dimensional numerical simulations to study the dynamics and deformation of a sheared ferrofluid droplet immersed in a Newtonian viscous fluid subjected to a magnetic field. Just after, Hassan, Zhang and Wang (2018) and Capobianchi, Lappa and Oliveira (2018) expanded the study of Jesus, Roma and Ceniceros (2018) increasing knowledge about field-induced deformation of ferrofluid droplets in shear flows. Cunha et al. (2018) were the great innovators in the subject, being the first to explore the magnetic field effects on droplet breakup and emulsion rheology. They showed that the intensity and direction of the external magnetic field can be effectively used to induce or prevent the breakup of ferrofluid droplets under shear. In addition, as the field directly affects the droplet shape, it can be able to be adjusted to increase or decrease the viscosity of dilute magnetic emulsions. The results of Cunha et al. (2018) for the breakup control by the action of external magnetic fields were extended to shear flow at low Reynolds number by Hassan and Wang (2019). Recently, Cunha et al. (2020) and Ishida and Matsunaga (2020) extended, respectively, in 2D and 3D, the previous analysis of Cunha et al. (2018) to further investigate the dynamics of

ferrofluid droplets and the rheology of magnetic emulsions under shear. Abicalil et al. (2021) extended to 3D the 2D study of Cunha et al. (2020) getting results qualitatively similar on the magnetization of dilute magnetic emulsions subjected to shear flows and external magnetic fields. Other works considered the effects of the magnetic field on the lateral migration of a two-dimensional (2D) viscous ferrofluid droplet in a plane Poiseuille flow (HASSAN; WANG, 2020) and on the magnetofluidic mixing of a ferrofluid droplet (SHYAM; MONDAL; MEHTA, 2021). However, in all these cases, the surfactant effects weren't considered.

In turn, several numerical studies have been performed in the past three decades to account for the effects of insoluble surfactants on the droplet deformation, orientation, and breakup, in 2D (STONE; LEAL, 1990; MILLIKEN; STONE; LEAL, 1992; EGGLETON; TSAI; STEBE, 2001; VLAHOVSKA; BLAWZDZIEWICZ; LOEWENBERG, 2002; JAMES; LOWENGRUB, 2004) and in 3D (BAZHLEKOV; ANDERSON; MEIJER, 2006; FEIGL et al., 2007); on the unsteady behavior (KRUIJT-STEGEMAN; VOSSE; MEIJER, 2004); and on the emulsion's rheology (LI; POZRIKIDIS, 1997). A number of studies focused on the surfactant concentration evolution in different flow configurations (XU et al., 2006; XU; YANG; LOWENGRUB, 2012; MURADOGLU; TRYGGVASON, 2014), the dielectrophoresis (DEP) of a viscous droplet loaded with insoluble surfactant in the presence of a non-uniform electric field (MANDAL; BANDOPADHYAY; CHAKRABORTY, 2016), and the behavior of soluble surfactant-covered droplet (XU; SHI; LAI, 2018; SHI et al., 2019). More specifically, in the last six years, several researchers have studied the effect of the interfacial viscosity (PONCE-TORRES et al., 2017; LUO; SHANG; BAI, 2019; DANDEKAR; ARDEKANI, 2020; PANIGRAHI et al., 2021), Marangoni stress (LUO; SHANG; BAI, 2018; HILL; AFUWAPE, 2020), and electric field (PODDAR et al., 2018; PODDAR et al., 2019; SORGENTONE; TORNBERG; VLAHOVSKA, 2019; SORGENTONE; VLAHOVSKA, 2021; ZHANG; LIU; ZHANG, 2021) on the droplet dynamics under the simple shear, extensional, and Poiseuille flows. Other studies also evaluated the surfactant's effects on the deformation of viscoelastic droplets in a uniaxial extensional flow (PANIGRAHI; DAS; CHAKRABORTY, 2018), droplet migration in isothermal (DAS; MANDA; CHAKRABORTY, 2017) and non-isothermal Poiseuille flow (DAS et al., 2017), thermocapillary migration in microchannels (LUO; LUO; BAI, 2020), the droplet breakup, coalescence and size distribution in turbulent flow (SOLIGO; ROCCON; SOLDATI, 2019a; SOLIGO; ROCCON; SOLDATI, 2019b), the behavior of a surfactant-covered droplet on a solid surface subject to a three-dimensional shear flow (LIU et al., 2020), and the flow inside a surfactant-laden droplet (SHAIK; VASANI; ARDEKANI, 2018). These works produced a series of results, today, well-known:

- At low capillary and larger Péclet numbers (convection dominated the surfactant motion), the presence of surfactant causes larger deformation than would occur for a droplet with a constant interfacial tension equal to the initial equilibrium value. The increased deformation occurs owing to the surfactant being swept to the end

of the droplet where it acts to locally lower the interfacial tension, which therefore requires increased deformation to satisfy the normal stress balance. However, at larger capillary numbers and finite deformations, this convective effect competes with the surfactant dilution due to the interfacial area increasing. Furthermore, at low or larger capillary numbers and small Péclet numbers (diffusion dominated the surfactant motion), it occurs less droplet deformation than for larger Péclet numbers (STONE; LEAL, 1990; MILLIKEN; STONE; LEAL, 1992; BAZHLEKOV; ANDERSON; MEIJER, 2006; FEIGL et al., 2007). According to Milliken, Stone and Leal (1992) and Feigl et al. (2007), these effects are found to be most pronounced for small viscosity ratios, where Marangoni stresses substantially retard the interfacial velocity and cause the droplet to behave as though it were more viscous. Bazhlekov, Anderson and Meijer (2006) shows that this can happen locally as well as globally, depending on the amount of surfactant.

- At larger surfactant concentrations, the surfactant accumulates at the droplet tips and the surface tension drives near to zero. The droplet assumes a transient shape with highly pointed tips, from which, thin liquid threads are pulled out, emitting small surfactant-rich droplets from the termini of these threads. The scale of the shed droplets depends on the initial surfactant coverage. Dilute initial coverage leads to tip streaming, while high initial coverage leads to the tip-dropping breakup mode (EGGLETON; TSAI; STEBE, 2001). According to James and Lowengrub (2004), even when the initial surfactant distribution is dilute, the increases in surfactant concentration at the droplet's tips can result in a local deviation from the dilute limit. This can lead to differences in effective surface tension, the Marangoni forces, and the associated droplet dynamics between results using the linear and nonlinear equations of state.

- Under weak-flow conditions, deformation is enhanced by the presence of surfactant, but the leading-order perturbation of the droplet shape is independent of the nonzero surfactant elasticity. In strong flows, droplet deformation depends non-monotonically on surfactant elasticity. In the weak-flow limit with finite surfactant elasticity, the emulsion behaves as a suspension of rigid spheres. In strong flows, the stresses can approach the behavior for surfactant-free droplets (VLAHOVSKA; BLAWZDZIEWICZ; LOEWENBERG, 2002).

- The presence of surfactant results in more complex droplet–droplet interactions compared to the analogous cases for clean droplets. The effects of surfactants are found to be most significant in flows with multiple droplets (XU et al., 2006), where the surfactants can play a critical role in preventing droplet coalescence (XU; YANG; LOWENGRUB, 2012).

- In the breakup of a surfactant-covered droplet under shear flow, a significant amount of surfactant is trapped in the resulting satellite droplet. This result is directly linked

to the surface viscosities, which play a critical role to explain the accumulation of surfactant in the satellite droplet (PONCE-TORRES et al., 2017), since the shear surface viscosity inhibits local convection, due to its suppression on the droplet surface motion, and has remarkable influences on the droplet deformation (LUO; SHANG; BAI, 2019; DANDEKAR; ARDEKANI, 2020). According to Dandekar and Ardekani (2020), the inclusion of interfacial viscosities is important to accurately model the migration characteristics of droplets for experiments involving droplet manipulation in Poiseuille flow, because both the dilatational as well as the shear surface viscosities suppress the lateral migration velocity of the droplet (PANIGRAHI et al., 2021).

- In pressure-driven channel flow, surfactant-induced Marangoni stresses counteract the shear-induced lift force and can reverse the lateral bubble migration completely, i.e., to make the surfactant-covered bubble move away from the channel wall and stabilizes at the center line (MURADOGLU; TRYGGVASON, 2014).

- In Poiseuille flows, the droplet migration is directly linked to the relationship between surfactant diffusion and advection, where the direction and velocity of migration depend on the droplet viscosity. If diffusion is dominant, increasing surfactant elasticity reduces the axial velocity of the droplet. On the other hand, at larger surface advection, the droplet always moves towards the flow center line, and the axial velocity of the droplet is found to be independent of the surfactant distribution (DAS; MANDA; CHAKRABORTY, 2017). When the flow is non-isothermal so that temperature increases in the flow direction, surfactants retard the droplet motion as compared with the surfactant-free droplets. If the imposed temperature decreases in the flow direction, the presence of surfactants may increase or decrease the magnitude of droplet velocity, depending on the surfactant coverage and elasticity (DAS et al., 2017). The same is observed for surfactant-laden droplets inside microchannels, where the migration is significantly retarded by the thermal convection (LUO; LUO; BAI, 2020).

- The surfactant directly affects the additional pressure loss from the droplets in non-circular microchannels. The surfactant-induced reduction in droplet surface tension decreases the additional pressure loss, but this effect can be fully counteracted by the effect of the surface tension gradient (Marangoni stress). The increasing effect of the Marangoni stress is directly related to two surfactant-related dimensionless parameters, the surface Péclet number, and the elasticity number. Thus, the additional pressure loss significantly increases with either of them increasing. (LUO; SHANG; BAI, 2018).

- At low frequencies, nano-droplets behave like rigid spheres, but at the megahertz frequencies of electroacoustic (and other spectral-based) diagnostics, the interfacial concentration gradients are dynamic, coupling electromigration, advection, and diffu-

sion fluxes. In these conditions, the droplet interface transits from a rigid/immobile one to a fluid one (HILL; AFUWAPE, 2020).

- When either of the phases may exhibit a viscoelastic behavior, increasing Marangoni stress decreases the effect of viscoelasticity on the shape deformation of the droplet. Thus, in the limit of diffusion-dominated surfactant transport, the effect of the surfactant convection is to diminish the relative importance of the viscoelastic effects (PANIGRAHI; DAS; CHAKRABORTY, 2018).

- In turbulent flows, Marangoni stresses have a major role in restoring a uniform surfactant distribution over the interface. This restoring effect is proportional to the surfactant elasticity and is stronger for smaller droplets. Lower surface tension (higher ratio between inertial and surface tension forces or higher surfactant elasticity) increases the number of breakup events, but also the number of coalescence events (SOLIGO; ROCCON; SOLDATI, 2019a; SOLIGO; ROCCON; SOLDATI, 2019b).

- For droplets in contact with solid surfaces as presented by Xu and Ren (2014), the presence of surfactants not only increases droplet deformation but also promotes droplet motion. Increasing surfactant coverage enhances droplet deformation and motion, although the surfactant distribution becomes less non-uniform. The presence of surfactants always decreases the critical capillary number for the breakup. This effect is more pronounced at low viscosity ratio (LIU et al., 2020).

- For a perfectly conducting/dielectric droplet suspended in a perfectly dielectric medium, the Marangoni stress always retards the dielectrophoretic velocity of the droplet as compared with a surfactant-free droplet. For a leaky dielectric droplet suspended in another leaky dielectric medium, in the low Péclet number limit, depending on the electrical conductivity and permittivity of both the liquids, Marangoni stress may aid or retard the dielectrophoretic velocity of the droplet. Marangoni stress also has the ability to move the droplets with less viscosity in the opposite direction as compared with a surfactant-free droplet. This was observed for particular values of electrical conductivity and permittivity ratios. At larger Péclet number limit, the surfactants completely immobilize the fluid velocity at the droplet interface, making the droplet behaves like a solid sphere (MANDAL; BANDOPADHYAY; CHAKRABORTY, 2016).

- The surfactant weakens the electrohydrodynamic flow, and thus dielectrophoretic interactions play a more prominent role than surfactant-free droplets. If droplet conductivity is the same as the suspending fluid, a non-diffusing surfactant can arrest the droplets' relative motion thereby effectively preventing coalescence (SORGENTONE; VLAHOVSKA, 2021). If the droplet exhibits an oblate shape and the electrical forces are large, the presence of surfactants almost does not affect droplet deformation (ZHANG; LIU; ZHANG, 2021).

- The location of the peak surfactant accumulation on the droplet surface may get shifted from the plane of shear to a plane orthogonal to it, depending on the inclination angle of the applied electric field and the force of the electrical stresses relative to their hydrodynamic counterparts. This creates significant alterations in the Marangoni stress around the droplet, triggering modulations in the bulk shear viscosity. Thus, the balance between electrical and hydrodynamic stresses modulates the emulsion viscosity (PODDAR et al., 2019). When a leaky dielectric droplet is sedimenting in another leaky dielectric fluid at low Péclet number, the Marangoni stress can oppose the electrohydrodynamic motion severely, thereby causing corresponding changes in the internal flow pattern (PODDAR et al., 2018).

On the other hand, the effects of surfactants on the emulsion's rheology were initially studied by Li and Pozrikidis (1997) using a linear relationship between surface tension and surfactant concentration. They found that surfactants have a greater impact on the rheology of a suspension than on the deformation of individual droplets. The rheology of a dilute emulsion of surfactant-covered spherical droplets was investigated by Blawzdziewicz, Vlahovska and Loewenberg (2000) showing, like Li and Pozrikidis (1997), that the rheological contributions of the droplets can be significantly affected by small quantities of surfactant and the effects of droplet deformation and Marangoni stresses are additive. Vlahovska, Blawzdziewicz and Loewenberg (2002) studied the nonlinear rheology of a dilute emulsion of surfactant-covered spherical droplets in time-dependent flows, considering low capillary numbers (negligible droplet deformation) and creeping-flow conditions. Their results showed that the interplay between the Marangoni relaxation time, rotation time, and period of imposed flow oscillations gives rise to a rich rheological behavior in diluted emulsions with surfactant-covered spherical droplets, mainly manifesting in terms of the normal stress differences.

More recently, Zinchenko and Davis (2017) proposed and tested a general constitutive model for highly concentrated monodisperse emulsions of deformable droplets with insoluble surfactant through long-time, large-scale, and high-resolution droplet simulations. However, only the limit of small surfactant diffusivities (Péclet number tends to infinity) was addressed, besides assuming a linear relationship between surfactant concentration and surface tension. Mandal, Das and Chakraborty (2017) performed analytical investigations on the deformation and rheology of a dilute emulsion of surfactant-laden droplets suspended in linear flows. As opposed to the work of Zinchenko and Davis (2017), the analysis was carried out for situations dominated by surface diffusion (Péclet number tends to zero). Mandal, Das and Chakraborty (2017) showed that increasing the non-uniformity of the surfactant distribution results in larger droplet deformation and effective viscosity for either of the linear flows considered. Under simple shear flow, the surfactant distribution has no effects on the inclination angle. However, a higher viscosity ratio induces the droplet alignment towards the flow direction. Das, Bhattacharjee and Chakraborty (2018) studied the effect of the interfacial slip on the deformation and rheology of a dilute

suspension of droplets in a linear flow using the assumption of negligible inertia effects in both phases. In another work, Das and Chakraborty (2018) studied the effect of surface viscosity on the thermocapillary migration of a surfactant-laden droplet in the presence of non-isothermal Poiseuille flows. More recently Dandekar and Ardekani (2020) examined the effect of interfacial rheology on the droplet dynamics assuming a purely viscous surface with a small amount of surfactant, such that interfacial viscosity does not depend on the surfactant concentration. They considered a surfactant-covered non-deformable droplet in an unbounded Poiseuille at low surface Péclet numbers.

Most of the investigations in the literature assume a linear relationship between the surface tension and the surfactant concentration. To our knowledge, no works in the literature dedicated to the effects of surfactant elasticity (sensitivity of surface tension to variations in surfactant concentration), as well as the surfactant coverage (relationship between the initial average surfactant concentration and the surfactant concentration at the maximum packing) on the emulsion's rheology. In addition, these studies focused on specific cases, such as the low capillary number and small surfactant diffusivities. Most importantly, no studies report the combined effects of surfactant and magnetic field.

The combined action of surfactants and magnetic field adds a new dynamics to the individual droplets simulation. The major difficulty is dealing with the coupling between the velocity field and the surfactant's distribution since both are closely linked to the morphology and mobility of the droplet interface, which is also affected by the action of the magnetic field. In addition to mass and momentum equations, required to simulate the droplet's dynamics, it is now necessary to solve two extra equations, one for the surfactant's concentration (defined only on the surface) and another for the magnetic field. In this sense, numerical simulations provide great possibilities to understand the physics of these systems, making it possible to test from the simplest situations to the most difficult ones to be reproduced in laboratories.

Several numerical methods were used to approach the surfactant-covered droplet problems. In general, this can be divided into two paths: interface-tracking or interface-capturing methods. The first group includes the front-tracking method (MURADOGLU; TRYGGVASON, 2008; JESUS et al., 2015; MURADOGLU; TRYGGVASON, 2014; LU; MURADOGLU; TRYGGVASON, 2017; LUO; SHANG; BAI, 2019), the boundary integral method (BIM) (STONE; LEAL, 1990; MILLIKEN; STONE; LEAL, 1992; LI; POZRIKIDIS, 1997; EGGLETON; TSAI; STEBE, 2001; BAZHLEKOV; ANDERSON; MEIJER, 2006; FEIGL et al., 2007; SORGENTONE; TORNBERG, 2018; HSU et al., 2019; PÅLSSON; SIEGEL; TORNBERG, 2019; SORGENTONE; TORNBERG; VLAHOVSKA, 2019) and the immersed boundary method (IBM) (LAI; TSENG; HUANG, 2008). These use a separate mesh to trace the interface, which increases the complexity of discretizing the equations. Interface-capturing methods use an indicator function to implicitly represent the interface in an Eulerian mesh for better handling of large deformations and topological changes using regular cartesian discretizations. Among these methods, the following stand

out: volume-of-fluid (VOF) (HIRT; NICHOLS, 1981; JAMES; LOWENGRUB, 2004; DRUMRIGHT-CLARKE; RENARDY, 2004), (OSHER; SETHIAN, 1988; XU et al., 2006; XU; REN, 2014; LANGAVANT et al., 2017; TITTA et al., 2018; XU; SHI; LAI, 2018) phase-field method (LIU; ZHANG, 2010; SHI et al., 2019; SOLIGO; ROCCON; SOLDATI, 2019a; SOLIGO; ROCCON; SOLDATI, 2019b; ZHU et al., 2019; SOLIGO; ROCCON; SOLDATI, 2020).

The level set method was used to capture the surfactant-covered droplet interface for the first time by Xu et al. (2006). This approach has been improved to consider the flow dynamics (XU; YANG; LOWENGRUB, 2012) and the contact line for the cases of insoluble surfactant (XU; REN, 2014) and soluble surfactant (XU; SHI; LAI, 2018). In these studies, the surfactant concentration is extended to a small region around the interface, and the surface Laplacian is rewritten, as described by Xu and Zhao (2003). In addition, the level set method was also used by Cunha et al. (2018), Cunha et al. (2020), and Abicalil et al. (2021) to capture the interface of ferrofluid droplets.

In this sense, an alternative methodology is proposed here. We use the level set method to capture the interface, along with the closest point method (RUUTH; MERRIMAN, 2008; MACDONALD; RUUTH, 2010) to extend the surfactant concentration equation to a region around the interface. The closest point method has been applied in the solution of many distinct systems involving partial differential equations (PDEs) defined on surfaces (PETRAS; RUUTH, 2016; VOGL, 2017; PETRAS et al., 2019). One of the advantages of this approach is that conventional finite differences/element methods can be used for solving surface equations.

Up to the authors' knowledge, our numerical approach is unprecedented for surfactant-covered droplets and is used for the first time in this work. We consider a single two-dimensional surfactant-covered droplet of a superparamagnetic ferrofluid suspended in an immiscible, non-magnetizable liquid confined in a channel between parallel plates. The system is simultaneously subjected to a simple shear flow and an external uniform magnetic field. The model consists of an unsteady convection-diffusion equation to compute the evolution of the surfactant concentration over the droplet surface, along with the non-linear Langmuir equation of state to compute the surface tension, coupling the surfactant concentration with the incompressible Navier–Stokes equations, and Maxwell's equations at the magnetostatic limit coupled to model the magnetic problem. The level set method is used to capture the droplet interface and the closest point method to solve partial differential equations on the droplet surface. We present a theoretical formulation to calculate the stress tensor of a dilute emulsion of surfactant-covered ferrofluid droplets in which the stress jump across the droplet surface accounts for the Marangoni stresses, in addition to the usual capillary pressure jump and the magnetic stresses.

The main contribution of this work relies on the comprehension of the combined effects of surfactant elasticity, coverage factors, and the magnetic field on the flow at the droplet's scale and its impacts on the emulsion's rheology and bulk magnetization. We

use a non-linear equation of state to calculate the surface tension as a function of the surfactant concentration from diffusion-dominated to advection-dominated cases. Using a particle stress formulation to compute the average emulsion' stress tensor, we were able to calculate the emulsion's viscosity and separate the contributions from the normal stress jump, which we called *capillary viscosity*, the contribution from the tangential stress jump, which we called *Marangoni viscosity*, and the contribution of the magnetic field, which we called *magnetic viscosity*. Using these new definitions, we show how emulsions of droplets of the same shape display remarkably distinct rheological behavior. We found that capillary and Marangoni viscosities have opposite behavior concerning the surfactant coverage and elasticity. The magnetic field action evidences these differences and its direction (vertical or horizontal) can invert the behavior of these quantities. We show how the competition between these parcels of viscosity leads to a complex mechanical response of the emulsion to shear flow and the magnetic field. We also found that the droplet deformation and inclination depend more on the surfactant's coverage and elasticity factors than on the surface Péclet number. However, the Péclet number greatly influences the emulsion's rheology because it has a decisive impact on the Marangoni viscosity. The magnetic field action changes the regions of surfactant accumulation so that the behavior of viscosity parcels is strongly altered as a function of the magnetic field intensity and direction. We also show that the complex configuration of the droplet and the surfactant concentration makes the mean magnetization of the system become noncollinear with the external field, leading to internal torques in the suspension. Finally, we explore the rheology of this non-symmetric complex fluid in terms of the shear viscosity and rotational viscosities. The numerical approach, combining level set and closest point methods, is a novelty as well.

1.1 Objectives

The thesis proposal is to perform a numerical study on the combined effect of external magnetic fields and insoluble surfactants on the dynamics of ferrofluid droplets under shear flow, on the rheological properties of the ferrofluid emulsions, and the mean magnetization of the system, as well. Specific objectives are:

- To develop a numerical methodology based on the projection method for Navier-Stokes equations, finite differences, level set, and closest point methods to simulate surfactant-covered droplets under shear flow;
- To develop a numerical methodology to compute the droplet shape;
- To understand how magnetic fields and the surfactant can influence the kinematic flow of surfactant-covered ferrofluid droplets;
- To study the rheology of surfactant-covered ferrofluid droplets emulsions subjected (or not) to an external magnetic field;

- To elucidate the link between the rheology of ferrofluid emulsions and the microscopic dynamics of the constituent particles;
- To determine the feasibility of controlling the rheology and overall behavior of such emulsions using external magnetic fields;
- To explore the surfactant effects on the emulsion mean magnetization;
- To elucidate how the methodology developed can be used to solve vesicle problems. In addition to presenting the challenges of this innovation.

1.2 Scope of the work

This work is organized as follows. In chapter 2, the mathematical formulation of the physics behind the problem is performed. Then the incompressible Navier-Stokes equations with additional terms that take into account the influence of the surfactant concentration and magnetic field, are presented, as well as the non-dimensionalization of these equations. Chapter 3 is devoted to describing the numerical methodology used in this research, considering technical aspects of the finite difference, projection, level set, and closest point methods. In addition, a numerical methodology to compute the droplet shape is presented. In chapter 4, the mathematical and numerical methodologies developed are validated by comparisons with results available in the literature, the model is explored and the results are discussed. First, only the surfactant effects are considered. The combined effect of this surface active agent and the external magnetic field is evaluated in sequence. Finally, chapter 6 contains the conclusions of this work.

2 Formulation

In this chapter, the mathematical formulation of the physics behind a surfactant-covered ferrofluid droplet under shear flow and an external magnetic field is presented. The problem is detailed defining all relevant aspects and variables involved. Maxwell equations are presented, followed by the fluid magnetization and electromagnetism considerations used, leading to the so-called magnetostatic limit, where the magnetic field becomes irrotational and the problem can be described by a magnetic potential field. Then, the incompressible Navier-Stokes equations with additional terms that take into account the influence of the surfactant and magnetic field, are presented. There is still an unsteady convection-diffusion equation for computing the evolution of the surfactant concentration at the droplet surface and the non-linear Langmuir equation of state for computing the surface tension, coupling the surfactant concentration with the Navier-Stokes equations. Following, the governing equations are normalized and the particle stress formulation is explained to compute the average emulsion' stress tensor, separating *capillary*, *Marangoni* and *magnetic viscosities*. We also separate the symmetric and antisymmetric parts of the stress tensor, dividing the emulsion viscosity into two distinct contributions: shear and rotational viscosities, respectively. Finally, a brief discussion about bulk magnetization is presented.

2.1 Problem statement

The problem consists of a two-dimensional channel between two fluid-filled parallel plates in which there is a single surfactant-covered ferrofluid droplet placed at the center, as shown in Figure 1. The surfactant concentration on the droplet surface is c. The droplet is confined in the region Ω_2 and the continuous phase occupies the region Ω_1. The interface Γ separates both regions. The continuous phase has viscosity η and magnetic permeability μ_0, which is assumed to be equal to the magnetic permeability of the free space ($\mu_0 = 4\pi \times 10^{-7} \mathrm{H} \cdot \mathrm{m}^{-1}$). The ferrofluid droplet, which is initially circular with radius a and positioned at the domain center, has viscosity $\lambda\eta$ and magnetic permeability $\zeta\mu_0$. Thus, λ and ζ represent, respectively, the viscosity ratio and magnetic permeability ratio between the dispersed and continuous phases. Both phases are assumed Newtonian and incompressible, with the same density ρ. The system is subjected to an external uniform

magnetic field $\mathbf{H}_0$, which is applied either parallel or perpendicular to the plates, and a simple shear flow with shear rate $\dot{\gamma}$, driven by the motion of the channel walls in opposite directions with velocity $U_n = \dot{\gamma}H_p/2 = -U_s$, where H_p is the distance separating the walls.

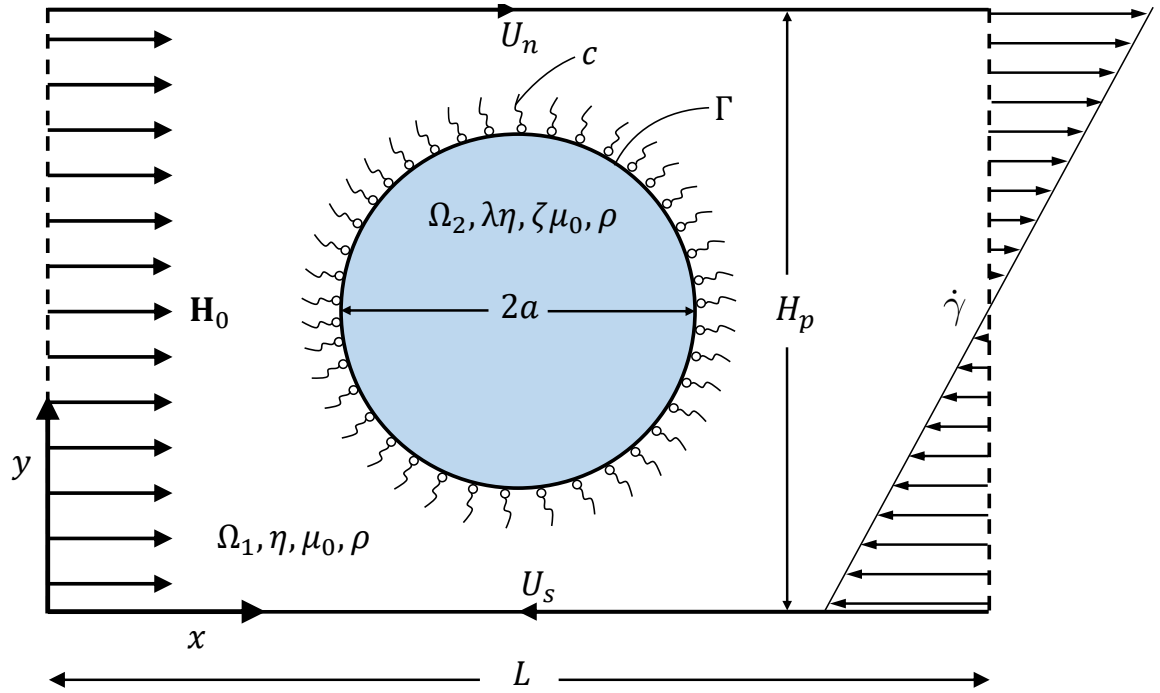

Figure 1 – Schematic illustration of a surfactant-covered droplet under simple shear flow. Ω_2 corresponds to the droplet region and Ω_1 corresponds to the continuous phase, Γ is the the interface, η is the continuous phase viscosity, $\lambda\eta$ is the droplet viscosity, ρ is the droplet and continuous phase density, a is the droplet radius, $\dot{\gamma}$ is the shear rate, c is the surfactant concentration, $U_n = \dot{\gamma}H_p/2 = -U_s$ is the canal walls velocity, $\mathbf{H}_0$ is the external uniform magnetic field ,H_p is the distance between the channel walls, and L is the length of the channel walls.

The surfactant molecules consist of a hydrophilic head and a hydrophobic tail, as shown in Figure 1. For insoluble surfactants, the molecules remain at the droplet surface, now for soluble surfactants, the molecules can be adsorbed from the bulk fluid to the interface and desorbed from the interface to the bulk fluid. In general, the surfactant reduces the surface tension and as the flow develops and the droplet deforms, the non-uniform distribution of the surfactant concentration gives rise to the surface tension gradient, i.e., the so-called Marangoni effect.

2.1.1 Superparamagnetic emulsions

Superparamagnetic materials can be much more magnetizable for the same magnetic field than paramagnetic materials. As presented by Cunha et al. (2020), applied magnetic field affects the magnetization $\mathbf{M}$ of the ferrofluid, which, in turn, contributes to the magnetic induction as $\mathbf{B} = \mu_0(\mathbf{H}+\mathbf{M})$. In the absence of electric currents, $\mathbf{H}$ and $\mathbf{B}$ satisfy magnetostatic Maxwell's equations, $\nabla\cdot\mathbf{B} = 0$ and $\nabla\times\mathbf{H} = 0$. We assume that the ferrofluid is superparamagnetic such that $\mathbf{M} = \chi_m\mathbf{H}$, where χ_m is the magnetic susceptibility. This

assumption leads to $\mathbf{B} = \mu_0\zeta\mathbf{H}$, where $\mu_0\zeta = \mu_0(1 + \chi_m)$ is the magnetic permeability of the dispersed ferrofluid phase. Since $\mathbf{H}$ is an irrotational field, there is a scalar potential ψ that satisfies $\mathbf{H} = -\nabla\psi$. Then, the magnetic problem is reduced to

$$\nabla \cdot [\mu_0\zeta(\mathbf{x})\nabla\psi] = 0, \tag{2.1}$$

where $\mathbf{x}$ is the position vector, and $\zeta(\mathbf{x})$ is the ratio between the local and the vacuum magnetic permeabilities, $\zeta(\mathbf{x}) = \mu(\mathbf{x})/\mu_0$, being equal to the unit for the continuous phase.

2.2 The governing equations

In this section, the governing equations are presented and discussed. The fluid motion is governed by the Navier-Stokes equations in the single-fluid formulation, as follows:

$$\nabla \cdot \mathbf{u} = 0, \tag{2.2}$$

$$\rho\frac{D\mathbf{u}}{Dt} = -\nabla p + \nabla \cdot [\lambda(\mathbf{x})\eta(\nabla\mathbf{u} + \nabla\mathbf{u}^T)] + \mathbf{F}_s + \mathbf{F}_{mag}, \tag{2.3}$$

where,

$$\frac{D\mathbf{u}}{Dt} = \frac{\partial\mathbf{u}}{\partial t} + \mathbf{u} \cdot \nabla\mathbf{u} \tag{2.4}$$

is the material derivative operator, ∇ is the gradient operator, $\nabla\cdot$ is the divergence operator, $\mathbf{u}$ is the velocity field, which has components u, v and w, respectively, in the x, y and z directions, t is the time, $\lambda(\mathbf{x})$ is the viscosity ratio between the local and continuous phases, p is the pressure field, $\mathbf{F}_{mag}$ is the magnetic force per unit of volume arising from the magnetic field, given by

$$\mathbf{F}_{mag} = \mu_0 \left(\zeta(\mathbf{x}) - 1\right) \mathbf{H} \cdot \nabla\mathbf{H}, \tag{2.5}$$

and $\mathbf{F}_s$ is a body force per unit of volume accounting for the stress jump across the interface.

Balancing forces on a finite surface element dS at the droplet surface, as presented in Figure 2, the effect associated with surface tension (energy per unit area) is reflected in a force per unit length in the element's contour C. That way, if the surface is in equilibrium,

$$-\int_S \Delta p\ \hat{\mathbf{n}}\ dS = \oint_C \sigma\hat{\mathbf{b}}\ d\Gamma, \tag{2.6}$$

in which the term on the left is the force due to pressure field action, $\hat{\mathbf{b}}$ is the unit binormal vector, perpendicular to tangential and normal unit vectors, $\hat{\mathbf{t}}$ and $\hat{\mathbf{n}}$, respectively, that

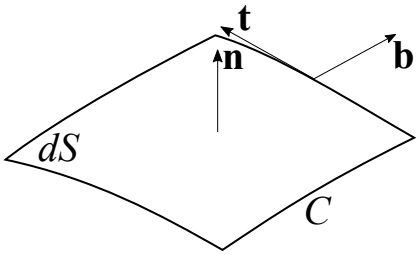

Figure 2 – Surface element used to derive equations at surface. $\hat{\mathbf{b}}$ is the unit binormal vector, $\hat{\mathbf{t}}$ is the unit tangential vector and $\hat{\mathbf{n}}$ is the unit normal vector. C represents the contour and dS is the finite surface element.

is $\hat{\mathbf{b}} = \hat{\mathbf{t}} \times \hat{\mathbf{n}}$ and $d\Gamma$ is the differential arc length along C. Using a variation of Stokes theorem, the right side of Eq. (2.6) can be rewritten as:

$$\oint_C \sigma\hat{\mathbf{n}} \times \hat{\mathbf{t}}\, d\Gamma = \int_S \left\{\hat{\mathbf{n}}\left[\nabla \cdot (\sigma\hat{\mathbf{n}})\right] - \left[\nabla\left(\sigma\hat{\mathbf{n}}\right) \cdot \hat{\mathbf{n}}\right]\right\} dS, \tag{2.7}$$

where $\hat{\mathbf{n}} \times \hat{\mathbf{t}} = -\hat{\mathbf{b}}$. These contributions are localized around the interface through the use of a Dirac-delta function, therefore, from Eqs. (2.6) and (2.7), it can be shown that

$$\mathbf{F}_s = (\nabla_s\sigma - \sigma\kappa\hat{\mathbf{n}})\delta(\|\mathbf{x} - \mathbf{x}_\Gamma\|). \tag{2.8}$$

In Eq.(2.8), σ is the surface tension coefficient, $\kappa = \nabla \cdot \hat{\mathbf{n}}$ is the local mean curvature, δ is the Dirac delta function, $\nabla_s = (\mathbf{I} - \hat{\mathbf{n}}\hat{\mathbf{n}}) \cdot \nabla$ is the surface gradient operator, and $\mathbf{I}$ is the unity tensor. The Dirac delta function is computed at $\|\mathbf{x} - \mathbf{x}_\Gamma\|$, where $\mathbf{x}_\Gamma$ is a point on the interface, such that $\mathbf{F}_s$ is concentrated at the droplet surface. Splitting $\mathbf{F}_s$ into normal and tangential components, we write

$$\mathbf{F}_s = \mathbf{F}_m + \mathbf{F}_c, \tag{2.9}$$

where $\mathbf{F}_m$ will be called the *Marangoni force* and $\mathbf{F}_c$, the *capillary force*, respectively, given by

$$\mathbf{F}_m = (\nabla_s\sigma)\delta(\|\mathbf{x} - \mathbf{x}_\Gamma\|), \tag{2.10}$$

end

$$\mathbf{F}_c = -(\sigma\kappa\hat{\mathbf{n}})\delta(\|\mathbf{x} - \mathbf{x}_\Gamma\|). \tag{2.11}$$

The concentrated body forces per unity of volume $\mathbf{F}_m$ and $\mathbf{F}_c$ can be interpreted as "stresses per unit of thickness" of the interface, due to the tangential and normal stress jumps, respectively.

Finally, replacing Eqs. (2.8) and (2.5) in Eq. (2.3), the fluid motion equation becomes:

$$\begin{aligned}\rho\frac{D\mathbf{u}}{Dt} = -\nabla p + \nabla \cdot [\lambda(\mathbf{x})\eta(\nabla\mathbf{u} + \nabla\mathbf{u}^T)] + (\nabla_s\sigma - \sigma\kappa\hat{\mathbf{n}})\delta(\|\mathbf{x} - \mathbf{x}_\Gamma\|) \\ +\mu_0\left(\zeta(\mathbf{x}) - 1\right)\mathbf{H} \cdot \nabla\mathbf{H}.\end{aligned} \tag{2.12}$$

2.2.1 Surfactant transport

The relationship between surface tension and local surfactant concentration is given by constitutive equations, here it is computed via the non-linear Langmuir equation of state (EOS),

$$\sigma(c) = \sigma_0 + RTc_\infty \ln\left(1 - \frac{c}{c_\infty}\right), \tag{2.13}$$

where σ_0 is the surface tension of a clean interface (no surfactant), R is the constant of the ideal gas, T is the absolute temperature, c is the local interfacial surfactant concentration and c_∞ is the maximum packing concentration.

To develop an evolution equation for the concentration of an insoluble surfactant, consider a material surface element $S(t)$ with differential surface area dS that lies on a two-dimensional curved surface embedded in the deformable three-dimensional space, as presented in Figure 2. In the absence of a chemical reaction or flux to the surface from either of the surrounding bulk phases, a mass balance of the surfactant concentration per unit area, c, require the conservation law:

$$\frac{D}{Dt}\int_S c\, dS = -\oint_C \hat{\mathbf{b}} \cdot \mathbf{j}\, d\Gamma, \tag{2.14}$$

where $\mathbf{j}$ is the tangential diffusion-flux vector, which is determined by Fick's law of diffusion. Since c is only defined along the surface, this law is written as:

$$\mathbf{j} = -D_s \nabla_s c, \tag{2.15}$$

where D_s is the surface diffusivity of the surfactant. If the surfactant were soluble, an additional term expressing absorption or adsorption from the bulk of the fluid to or from the interface would have to be added to the right-hand side of Eq. (2.14). Thus, substituting Eq. (2.15) in Eq. (2.14),

$$\frac{D}{Dt}\int_S c\, dS = D_s \oint_C \hat{\mathbf{b}} \cdot \nabla_s c\, d\Gamma. \tag{2.16}$$

The left side of Eq. (2.16) can be rewritten as

$$\frac{D}{Dt}\int_S c\, dS = \int_S \left(\frac{Dc}{Dt} dS + c\frac{D(dS)}{Dt}\right). \tag{2.17}$$

Batchelor (1970) shows that the time rate of change of a material surface element with vector area $d\mathbf{S} = \hat{\mathbf{n}} dS$ is

$$\frac{D(d\mathbf{S})}{Dt} = d\mathbf{S}\nabla \cdot \mathbf{u} - (\nabla \mathbf{u}) \cdot d\mathbf{S}, \tag{2.18}$$

performing the dot product of $\hat{\mathbf{n}}$ with Eq. (2.18),

$$\frac{D(dS)}{Dt} = dS\left[\nabla\cdot\mathbf{u} - \hat{\mathbf{n}}\cdot(\nabla\mathbf{u})\cdot\hat{\mathbf{n}}\right] = dS\nabla_s\cdot\mathbf{u}, \tag{2.19}$$

Using Eq. (2.19) and knowing that c is only defined along the surface, Eq. (2.16) can be rewritten as:

$$\int_S\left[\frac{\partial c}{\partial t} + \nabla_s\cdot(\mathbf{u}c)\right]dS = D_s\oint_c\hat{\mathbf{b}}\cdot\nabla_s c\;d\Gamma. \tag{2.20}$$

Using another variation of Stokes theorem, the integral on the right side of Eq. (2.20) can be rewritten as:

$$\oint_c(\mathbf{f}\times\mathbf{g})\cdot\hat{\mathbf{t}}\;d\Gamma = \int_S\left[\mathbf{f}\,(\nabla\cdot\mathbf{g}) - \mathbf{g}\,(\nabla\cdot\mathbf{f}) + (\mathbf{g}\cdot\nabla)\,\mathbf{f} - (\mathbf{f}\cdot\nabla)\,\mathbf{g}\right]\cdot\hat{\mathbf{n}}\;dS, \tag{2.21}$$

in which $\mathbf{f}=\mathbf{n}$ and $\mathbf{g}=\nabla c$. Thus, using the localization theorem (CHANDRASEKHARAIAH; DEBNATH, 1994) , the Eq. (2.20) can be rewritten as:

$$\frac{\partial c}{\partial t} + \nabla_s\cdot(\mathbf{u}c) = D_s\nabla_s^2 c, \tag{2.22}$$

where $\nabla_s^2 = \nabla_s\cdot\nabla_s$ is the surface Laplacian operator.

Finally, decomposing $\mathbf{u}$ into components along the surface, $\mathbf{u}_s = (\mathbf{I}-\hat{\mathbf{n}}\hat{\mathbf{n}})\cdot\mathbf{u}$ that represents the velocity field tangent to the interface, and $(\mathbf{u}\cdot\hat{\mathbf{n}})\,\mathbf{u}$ normal to the surface, the evolution of the interfacial surfactant concentration for the case of insoluble surfactants is governed by

$$\frac{\partial c}{\partial t} + \nabla_s\cdot(c\mathbf{u}_s) + c(\nabla_s\cdot\hat{\mathbf{n}})(\mathbf{u}\cdot\hat{\mathbf{n}}) = D_s\nabla_s^2 c. \tag{2.23}$$

Eq. (2.23) includes the standard convective and diffusive terms, but the term $c(\nabla_s\cdot\mathbf{n})(\mathbf{u}\cdot\hat{\mathbf{n}})$ is a contribution accounting for variation in surfactant concentration resulting from local changes in the interfacial area, being a function of the product of the mean curvature and the normal velocity.

2.3 Model normalization

The model is normalized using the dimensionless variables $t^* = t\dot{\gamma}$, $\mathbf{x}^* = \mathbf{x}/a$, $\mathbf{u}^* = \mathbf{u}/(\dot{\gamma}a)$, $p^* = p/(\rho a^2\dot{\gamma}^2)$, $\mathbf{H}^* = \mathbf{H}/|\mathbf{H}_0|$, $\sigma^* = \sigma/\sigma_0$ and $c^* = c/c_e$, where c_e is the initial average surfactant concentration, such that the dimensionless form of Eqs. (2.2), (2.12), (2.13) and (2.23) are, respectively,

$$\nabla^*\cdot\mathbf{u}^* = 0, \tag{2.24}$$

$$\begin{aligned}\frac{D\mathbf{u}^*}{Dt^*} = & -\nabla p^* \frac{1}{Re}\nabla^* \cdot [\lambda(\mathbf{x}^*)(\nabla^*\mathbf{u}^* + \nabla^*\mathbf{u}^{*T})] \\ + & \frac{1}{CaRe}\delta(\|\mathbf{x}^* - \mathbf{x}_\Gamma^*\|)(\nabla_s^*\sigma^* - \kappa^*\sigma^*\hat{\mathbf{n}}) \\ + & \frac{Ca_{mag}}{CaRe}\left(\zeta(\mathbf{x}) - 1\right)\mathbf{H}^* \cdot \nabla^*\mathbf{H}^*,\end{aligned} \tag{2.25}$$

$$\sigma^*(c^*) = 1 + E\ln\left(1 - X\,c^*\right) \tag{2.26}$$

and

$$\frac{\partial c^*}{\partial t^*} = -\nabla_s^* \cdot (c^*\mathbf{u}_s^*) + \frac{1}{Pe}\nabla_s^{*2}c^* - c^*(\nabla_s^* \cdot \hat{\mathbf{n}})(\mathbf{u}^* \cdot \hat{\mathbf{n}}), \tag{2.27}$$

where the surfactant elasticity, E, and the surfactant coverage, X, are, respectively,

$$E = \frac{RTc_\infty}{\sigma_0} \quad \text{and} \quad X = \frac{c_e}{c_\infty}. \tag{2.28}$$

The dimensionless groups are

$$Re = \frac{\rho\dot{\gamma}a^2}{\eta}, \quad Ca = \frac{\eta\dot{\gamma}a}{\sigma_0}, \quad Pe = \frac{a^2\dot{\gamma}}{D_s}, \quad Ca_{mag} = \frac{\mu_0 a|\mathbf{H}_0|^2}{\sigma_0} \tag{2.29}$$

where the Reynolds number, Re, expresses the ratio between inertia and viscous force; the capillary number, Ca, is the ratio between viscous and capillary forces; the surface Péclet number, Pe, expresses the ratio between the surfactant advection and diffusion rates on the droplet surface; and the magnetic capillary number, Ca_{mag} is the ratio between the magnetic and capillary forces.

2.4 Bulk stress on a surfactant-covered droplet emulsion

The bulk stress tensor of a suspension of solid or fluid particles, viewed as a homogeneous equivalent fluid, is the volume-averaged stress tensor (the *Stresslet*) defined by Batchelor (1970)

$$\langle\boldsymbol{\sigma}\rangle = -\langle p\rangle\mathbf{I} + \eta\left(\langle\nabla\mathbf{u}\rangle + \langle\nabla\mathbf{u}^T\rangle\right) + \langle\boldsymbol{\sigma}^d\rangle, \tag{2.30}$$

where $\langle\bullet\rangle$ represents the volumetric average and $\langle\boldsymbol{\sigma}^d\rangle$ is the contribution of the disperse phase to the bulk stress tensor, also known as *particle stress*. For dilute suspensions and emulsions, the hydrodynamic interaction among the particles is negligible, where it is possible to show that (KENNEDY; POZRIKIDIS; SKALAK, 1994)

$$\langle\boldsymbol{\sigma}^d\rangle = \frac{1}{V}\int_S \left[\mathbf{x}\Delta\mathbf{f} + \eta(\lambda - 1)(\mathbf{u}\hat{\mathbf{n}} + \hat{\mathbf{n}}\mathbf{u})\right] dS, \tag{2.31}$$

where V is the volume of the system (dispersed and continuous phases), S is the droplet surface, and $\Delta\mathbf{f}$ is the stress jump across the interface between the fluids.

In the presence of surfactants and magnetic fields, the ferrofluid droplet surface undergoes capillary, tangential (Marangoni), and magnetic stress jumps, called Δf_c, Δf_m and Δf_{mag}, respectively. According to Li and Pozrikidis (1997) and Cunha et al. (2020), $\Delta f_c = \sigma\kappa\hat{\mathbf{n}}$, $\Delta f_m = -\nabla_s\sigma$, and $\Delta f_{mag} = -\frac{1}{2}\mu_0(\zeta(\mathbf{x})-1)H^2\hat{\mathbf{n}}$. Therefore,

$$\Delta\mathbf{f} = \sigma\kappa\hat{\mathbf{n}} - \nabla_s\sigma - \frac{1}{2}\mu_0(\zeta(\mathbf{x})-1)|\mathbf{H}|^2\hat{\mathbf{n}}, \tag{2.32}$$

where $|\mathbf{H}|$ is the intensity of the magnetic field.

Using $\eta\dot{\gamma}$ as the characteristic tension scale to normalize $\langle\boldsymbol{\sigma}\rangle$ and $\langle\boldsymbol{\sigma}^d\rangle$, and combining Eqs. (2.32) and (2.31), the non-dimensional form of the particle stress of a dilute emulsion is given by

$$\begin{aligned}\langle\boldsymbol{\sigma}^{d*}\rangle = \frac{1}{V^*}\int_S \Big[&\frac{\sigma^*\kappa^*}{Ca}\mathbf{x}^*\hat{\mathbf{n}} - \frac{1}{Ca}\mathbf{x}^*\nabla_s^*\sigma^* - \frac{Ca_{mag}}{2Ca}(\zeta-1)|\mathbf{H}^*|^2\mathbf{x}^*\hat{\mathbf{n}} \\ &+ (\lambda-1)(\mathbf{u}^*\hat{\mathbf{n}} + \hat{\mathbf{n}}\mathbf{u}^*)\Big]\, dS^*.\end{aligned} \tag{2.33}$$

To isolate the contribution of the disperse phase to the bulk viscosity of the emulsion, we use the *reduced viscosity* defined as

$$[\eta] = \frac{\langle\boldsymbol{\sigma}_{yx}\rangle - \eta\dot{\gamma}}{\beta\eta\dot{\gamma}} = \frac{\langle\boldsymbol{\sigma}^{d*}_{yx}\rangle}{\beta}. \tag{2.34}$$

In addition, considering the different contributions of the stress jump, we define the *reduced capillary viscosity* as

$$[\eta_c] = \langle\boldsymbol{\sigma}^{d*}_{c,yx}\rangle/\beta, \tag{2.35}$$

where

$$\langle\boldsymbol{\sigma}^{d*}_{c}\rangle = \frac{1}{V^*}\int_S \frac{\sigma^*\kappa^*}{Ca}\mathbf{x}^*\hat{\mathbf{n}}dS^*, \tag{2.36}$$

the *reduced Marangoni viscosity* as

$$[\eta_m] = \langle\boldsymbol{\sigma}^{d*}_{m,yx}\rangle/\beta, \tag{2.37}$$

where

$$\langle\boldsymbol{\sigma}^{d*}_{m}\rangle = \frac{1}{V^*}\int_S -\frac{1}{Ca}\mathbf{x}^*\nabla_s^*\sigma^* dS^*, \tag{2.38}$$

and the *reduced magnetic viscosity* as

$$[\eta_{mag}] = \langle\boldsymbol{\sigma}^{d*}_{mag,yx}\rangle/\beta, \tag{2.39}$$

where

$$\langle\boldsymbol{\sigma}^{d*}_{mag}\rangle = \frac{1}{V^*}\int_S -\frac{Ca_{mag}}{2Ca}(\zeta-1)|\mathbf{H}^*|^2\mathbf{x}^*\hat{\mathbf{n}}dS^*. \tag{2.40}$$

In the particular case of $\lambda = 1$, when the sole contribution of the disperse phase to the emulsion's viscosity comes from $\Delta\mathbf{f}$, the reduced viscosity is the sum of the capillary, Marangoni, and the magnetic parts, such that

$$[\eta] = [\eta_c] + [\eta_m] + [\eta_{mag}]. \tag{2.41}$$

The capillary, Marangoni, and magnetic viscosities separate the contributions of the normal, tangential, and magnetic stress jumps across the interface to the reduced viscosity, respectively, providing a new tool to analyze the influence of the interface dynamics on the bulk stress tensor of the emulsion. Such a separation cannot be easily made in laboratory experiments (in fact, the authors believe it could be impossible nowadays), but the particle stress formulation allows the calculation of these quantities from numerical data, as done in the present work. As it will become clear along with this paper, these definitions are useful to the comprehension of the effects of surfactants on the interface of the droplets to the macroscopic mechanical behavior of the emulsion.

2.5 Bulk magnetization of the emulsion

The bulk magnetization of the system can be calculated from the magnetization of a single droplet as (CUNHA et al., 2020):

$$\langle \mathbf{M} \rangle = \frac{1}{V} \int_V (\zeta(\mathbf{x}) - 1)\, \mathbf{H} dV, \tag{2.42}$$

where the non-magnetizable phase does not account to mean magnetization, since $\zeta_\varepsilon(\phi) = 1$. Eq. (2.42) essentially shows that $\langle \mathbf{M} \rangle$ is a function of its geometry and the external magnetic field. Thus, the normalized form of Eq. (2.42) is:

$$\langle \mathbf{M}^* \rangle = \frac{1}{V^*} \int_V \frac{(\zeta(\mathbf{x}) - 1)\, \mathbf{H}^*}{\beta} dV. \tag{2.43}$$

Under shear flow, the emulsion magnetization does not perfectly align to the external magnetic field. This misalignment produces internal torques that ultimately lead to a non-symmetric stress tensor (CUNHA et al., 2020), which rotates the droplet toward the external magnetic field direction. According to Rosensweig (2013), the magnetic torque (per unit volume) is computed by

$$\boldsymbol{\tau}_{mag} = \mu_0 \langle \mathbf{M} \rangle \times \mathbf{H}_0, \tag{2.44}$$

or, normalizing by $\eta\dot{\gamma}\beta$,

$$\boldsymbol{\tau}^*_{mag} = \frac{Ca_{mag}}{Ca} \langle \mathbf{M}^* \rangle \times \mathbf{H}^*_0. \tag{2.45}$$

Eq. (2.45) shows that this magnetic torque is proportional to $\langle \mathbf{M} \rangle$ and $\sin(\theta_m)$, where θ_m is the misalignment angle between the bulk magnetization and the external magnetic field.

The angular momentum conservation law requires an opposite hydrodynamic torque of the same magnitude, which manifests itself as an asymmetry in the particle stress tensor. Thus, rewriting Eq. (2.30) as the sum of the symmetric and antisymmetric parts, respectively, we have:

$$\langle \boldsymbol{\sigma} \rangle = sym\langle \boldsymbol{\sigma} \rangle + asym\langle \boldsymbol{\sigma} \rangle, \tag{2.46}$$

where the antisymmetric part can be written in terms of the Levi- Civita permutation tensor, $\boldsymbol{\varepsilon}$ and the dual vector, $\boldsymbol{\omega}$ (CHANDRASEKHARAIAH; DEBNATH, 1994), as follows:

$$\langle \boldsymbol{\sigma} \rangle = sym\langle \boldsymbol{\sigma} \rangle + \frac{1}{2}\boldsymbol{\varepsilon}\mathfrak{L} \tag{2.47}$$

where,

$$\mathfrak{L} = -\boldsymbol{\varepsilon} : \langle \boldsymbol{\sigma}^d \rangle. \tag{2.48}$$

Thus, the normalized hydrodynamic torque is given by

$$\boldsymbol{\tau}^*_{hyd} = \mathfrak{L}^* = -\boldsymbol{\varepsilon} : \langle \boldsymbol{\sigma}^{d*} \rangle. \tag{2.49}$$

From this point in this work, all quantities are dimensionless and the asterisk will be suppressed to alleviate the nomenclature unless stated otherwise.

2.6 Magnetic emulsion viscosity

The results of Cunha et al. (2020) showed that external magnetic fields dramatically affect the droplet configuration in the flow, the bulk magnetization of the system. The internal magnetic torques that appear change the viscosity of the equivalent magnetic emulsion under shear, once the stress tensor becomes non-symmetrical, given by:

$$\langle \boldsymbol{\sigma} \rangle = \mathbf{S} + \mathbf{L}, \tag{2.50}$$

where $\mathbf{S}$ and $\mathbf{L}$ are the symmetric and antisymmetric parts of the stress tensor $\langle \boldsymbol{\sigma} \rangle$, respectively.

In this sense, it is convenient to split the viscosity into two distinct contributions: a shear viscosity, η_s, related with $\mathbf{S}$ and a rotational viscosity, associated with $\mathbf{L}$. These viscosities are defined, respectively, as

$$\eta_s = \frac{S_{yx}}{\eta\dot{\gamma}} - 1 \tag{2.51}$$

and

$$\eta_r = \frac{L_{yx}}{\eta\dot{\gamma}}. \tag{2.52}$$

In Eq. (2.51), the -1 term is used because η_s accounts only for the contribution of the dispersed phase to the emulsion shear viscosity. The same does not occur in Eq. (2.52) because the rotational viscosity arises exclusively from the non-linear effects. Thus, the emulsion's reduced viscosity can be determined both by the sum of capillary, Marangoni, and magnetic viscosities and by the sum of the reduced viscosities corresponding to η_s and η_r, as follows:

$$[\eta] = [\eta_s] + [\eta_r], \tag{2.53}$$

in which $[\eta_s] = \eta_s/\beta$ and $[\eta_r] = \eta_r/\beta$.

3 Numerical Methodology

This chapter presents the numerical methodology employed in this work, describing: aspects of the finite difference method for a uniform staggered grid; the level set method and the tube technology developed by Peng et al. (1999); aspects of the closest point method; the projection method and finite difference discretization of the governing equations to the flow; the boundary and initial conditions; a semi-implicit temporal discretization developed by Xu and Zhao (2003) in conjunction with a spatial discretization via closest point and finite differences methods to solve the surfactant transport equation; and a numerical methodology to compute the droplet shape.

3.1 Finite difference method

The finite difference is a numerical method based on the expansion of Taylor's series to discretize differential equations by rewriting the derivatives as finite differences. In this technique, equations relating to unknown functions are generated at a finite number of points in the computational domain, known as grid. At each point, the function value is related to the values at neighboring points, resulting in a linear system of equations after the proper application of the problem boundary conditions. The solution of this system gives the problem solution at each point of the grid.

The two-dimensional discretization used in the present work is based on a staggered grid, as illustrated in Figure 3, in which the variables are not defined at the same position. Here, the vectors fields components in x and y direction are evaluated on the right (empty squares) and upper (empty triangles) faces of the cells, respectively. The fluid properties and scalar fields are evaluated at the center of the cell (black circles). The position of the cells in the x and y directions are determined, respectively, by i and j. The grid is composed of N_x cells in the x-direction and N_y cells in the y-direction. Therefore, there is $[N_x \times N_y]$ points for scalar fields (central points), $[N_x + 1 \times N_y]$ points for vector components in x-direction and $[N_x \times N_y + 1]$ points for vector components in y-direction.

The Taylor's series states that the value of a generic continuous function with all

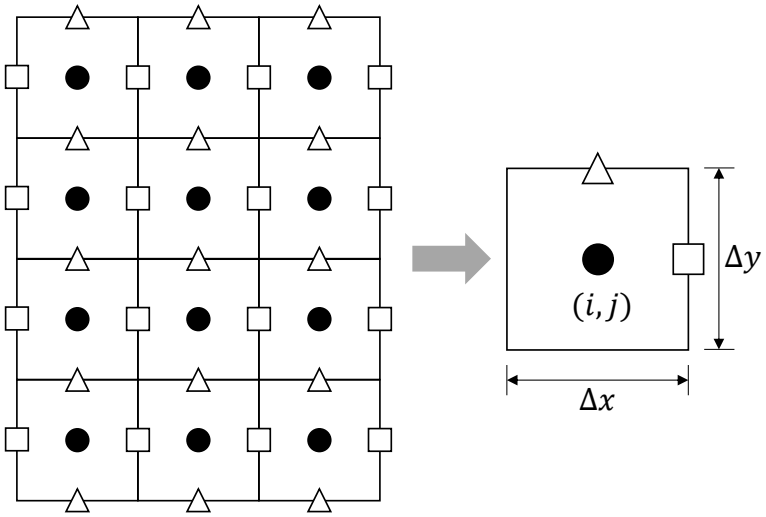

Figure 3 – Staggered grid and cell structures. Vector components in the x and y directions are stored, respectively, at the empty squares and circles. Scalar quantities are stored at the black circles.

derivatives also continuous, $f = f(x)$, at a point x in the neighbor of x_0 may be given by

$$f(x) = f(x_0) + \frac{f'(x_0)}{1!}(x - x_0) + \frac{f''(x_0)}{2!}(x - x_0)^2 + \frac{f'''(x_0)}{3!}(x - x_0)^3 + ..., \tag{3.1}$$

which can be rewritten in the more compact sigma notation as follows:

$$f(x) = \sum_{n=0}^{\infty} \frac{f^{(n)}(x_0)}{n!}(x - x_0)^n. \tag{3.2}$$

Consider the discretized one-dimensional domain as presented in Figure 4, is used the Taylor's series to predict the value of f at the node $i + 1$ and $i - 1$, respectively as,

$$f_{i+1} = f_i + \frac{f'_i}{1!}\Delta x + \frac{f''_i}{2!}\Delta x^2 + \mathcal{O}(\Delta x^3) \tag{3.3}$$

and

$$f_{i-1} = f_i - \frac{f'_i}{1!}\Delta x + \frac{f''_i}{2!}\Delta x^2 + \mathcal{O}(\Delta x^3). \tag{3.4}$$

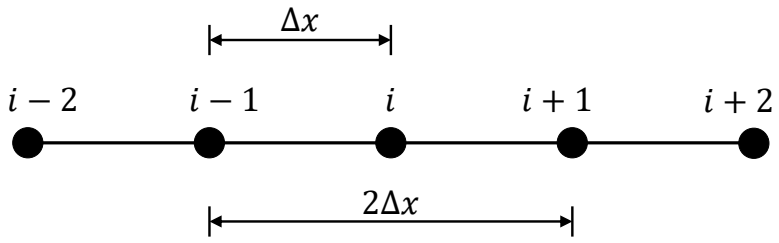

Figure 4 – One-dimensional discretization domain for finite difference method.

Note that in Eqs. (3.3) and (3.4) there is a loss in the prediction of the order $\mathcal{O}(\Delta x^3)$. Subtracting and adding both equations, the first and second central differential derivatives are obtained, respectively,

$$f_i' = \frac{f_{i+1} - f_{i-1}}{2\Delta x} + \mathcal{O}(\Delta x^2) \tag{3.5}$$

and

$$f_i'' = \frac{f_{i+1} - 2f_i + f_{i-1}}{\Delta x^2} + \mathcal{O}(\Delta x^2), \tag{3.6}$$

with order error $\mathcal{O}(\Delta x^2)$.

The staggered grid has some advantages for solving fluid motion equations because inhibits pressure fluctuations due to the independence between pressure and velocity at the same point. The derivative of velocity and pressure terms are computed over a distance of only Δx or Δy, equivalent to doubling the resolution of the grid whose properties were evaluated in the same position. For example, this scheme allows the computation of the partial derivatives of scalar fields on the right (empty squares) and upper (empty triangles) faces of the cells shown in Figure 3. Therefore,

$$\left.\frac{\partial f}{\partial x}\right|_{i,j} = \left.\frac{\partial f}{\partial x}\right|_{\text{right}} = \frac{f_{i+1,j} - f_{i,j}}{\Delta x} \quad \text{and,} \quad \left.\frac{\partial f}{\partial y}\right|_{i,j} = \left.\frac{\partial f}{\partial y}\right|_{\text{upper}} = \frac{f_{i,j+1} - f_{i,j}}{\Delta y}. \tag{3.7}$$

Similarly, this scheme allows the computation of the partial derivatives of vector field components at the center of the cell, black circles in Figure 3. Thus, considering the velocity vector $\mathbf{u}$,

$$\left.\frac{\partial u}{\partial x}\right|_{i,j} = \left.\frac{\partial u}{\partial x}\right|_{\text{center}} = \frac{u_{i,j} - u_{i-1,j}}{\Delta x} \quad \text{and,} \quad \left.\frac{\partial v}{\partial y}\right|_{i,j} = \left.\frac{\partial v}{\partial y}\right|_{\text{center}} = \frac{v_{i,j} - v_{i,j-1}}{\Delta y}. \tag{3.8}$$

This form will be very useful in the section 3.6.1 for the discretization of governing equations. However, the use of simple forward and backward differencing schemes with a two-point stencil is not suitable for the convective term of the Navier-Stokes equations as well as for the transport and reset equations of the level set function, considering that these schemes are first-order only. Therefore, the derivatives used in upwind schemes require the use of higher order and, therefore, more complex schemes. For this, ENO (Essentially Non-Oscillatory) and WENO (Weighted Essentially Non-Oscillatory) schemes (OSHER; FEDKIW, 2003) are used.

3.2 Level set method

To capture the interface, we use the level set method (OSHER; SETHIAN, 1988). In this approach, a level set function, $\phi(\mathbf{x}, t)$, is defined as the signaled distance from a point $\mathbf{x}$ to the interface $\mathbf{x}_\Gamma$, as presented in Figure 5, such that:

$$\phi(\mathbf{x}, t) = \begin{cases} \|\mathbf{x} - \mathbf{x}_\Gamma\|, & \mathbf{x} \in \Omega_1, \\ -\|\mathbf{x} - \mathbf{x}_\Gamma\|, & \mathbf{x} \in \Omega_2, \\ 0, & \mathbf{x} \in \Gamma. \end{cases} \tag{3.9}$$

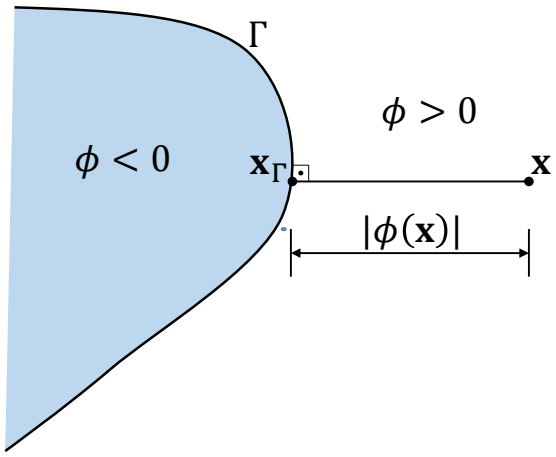

Figure 5 – Representation of the level set function.

Therefore, in the level set method, the interface is implicitly given by the equation $\phi(\mathbf{x}, t) = 0$. The level set function is assumed to be a conservative material property, advected by the velocity field, such that the evolution of ϕ is given by

$$\frac{\partial \phi}{\partial t} + \mathbf{u} \cdot \nabla \phi = 0. \tag{3.10}$$

The level set function can also be used to smooth a constant and avoid an abrupt transition between both regions (external and internal to Γ). For example, to evaluate the viscosity and permeability ratios between the dispersed and the continuous phases, λ and ζ, respectively, $\lambda(\mathbf{x}) = \lambda(\phi)$ and $\zeta(\mathbf{x}) = \lambda(\phi)$, such that the discontinuities across the liquid-liquid interface are replaced by smooth transitions occurring in a thin region of thickness ε. To this purpose, a smoothed Heaviside function is used, as follows:

$$H_\varepsilon(\phi) = \begin{cases} 0, & \text{if } \phi < -\varepsilon, \\ \frac{1}{2}\left[1 + \frac{\phi}{\varepsilon} + \frac{1}{\pi}\sin\left(\frac{\pi\phi}{\varepsilon}\right)\right], & \text{if } |\phi| \leq \varepsilon, \\ 1, & \text{if } \phi > \varepsilon. \end{cases} \tag{3.11}$$

Thus, the viscosity and permeability ratios are given, respectively, by:

$$\lambda_\varepsilon(\phi) = \lambda + (1 - \lambda) H_\varepsilon(\phi) \tag{3.12}$$

and

$$\zeta_\varepsilon(\phi) = \zeta + (1-\zeta)H_\varepsilon(\phi). \tag{3.13}$$

Using the definition of the Dirac delta in terms of the directional derivative of the Heaviside function, it is possible to show that (OSHER; FEDKIW, 2003)

$$\delta(\|\mathbf{x}-\mathbf{x}_\Gamma\|) = \nabla H(\phi)\cdot\hat{\mathbf{n}} = \frac{\partial H}{\partial\phi}|\nabla\phi| = \delta(\phi)|\nabla\phi|. \tag{3.14}$$

Thus, from the smoothed Heaviside function it is possible to define a smoothed Dirac delta distribution,

$$\delta_\varepsilon(\phi) = \frac{\partial H_\varepsilon(\phi)}{\partial\phi} = \begin{cases} 0, & \text{if } |\phi| > \varepsilon; \\ \frac{1}{2\varepsilon}\left[1+\cos\left(\frac{\pi\phi}{\varepsilon}\right)\right], & \text{if } |\phi| \le \varepsilon. \end{cases} \tag{3.15}$$

It is also possible to compute the unit normal vector outward of the droplet surface, the unit tangential vector, and the local mean curvature, respectively, as follows

$$\hat{\mathbf{n}} = \frac{\nabla\phi}{|\nabla\phi|}, \tag{3.16}$$

$$\hat{\mathbf{n}}\times\hat{\mathbf{t}} = \hat{\mathbf{b}}, \tag{3.17}$$

$$\kappa = \nabla\cdot\left(\frac{\nabla\phi}{|\nabla\phi|}\right). \tag{3.18}$$

The solution of Eq. (3.10) gives the evolution of surface $\Gamma(t)$ over time and, that is, the fluids interface propagation. Although the zero of the level set function, ϕ, continues to represent the surface, this evolution does not guarantee ϕ as the signed distance function of the interface for all the domain. Sussman (1994) proposed a technique to re-initialize the level set function in order to continue being a signed distance function of $\Gamma(t)$. Thus, the level set function ϕ is re-initialized to be a distance function, so that $|\nabla\phi| \approx 1$, by solving the following Hamilton–Jacobi equation until steady:

$$\frac{\partial\phi}{\partial\tau} = \phi_\tau = S(\phi)(1-|\nabla\phi|), \tag{3.19}$$

where τ is the pseudo-time and $S(\phi)$ is the sign function of ϕ.

Every time Eq. (3.19) is solved, the zero level set has to be redefined. Although this equation alone does not affect the position of the interface, in numerical computation, every time the interface is re-initialized, errors are accumulated. In this context, Sussman and Fatemi (1999) developed a constraint that significantly improves the accuracy of

solving (3.19), that is, since the interface should not move, the volume should not change either. therefore, Eq. (3.19) is modified:

$$\frac{\partial \phi}{\partial \tau} = \phi_\tau = S(\phi)(1 - |\nabla \phi|) + \lambda_m \delta_\varepsilon(\phi)|\nabla \phi|, \tag{3.20}$$

where and λ_m is a function of τ, which is obtained by imposing that

$$\partial_\tau \int_\Omega H(\phi) = \int_\Omega \delta(\phi)\phi_\tau = \int_\Omega \delta_\varepsilon(\phi) S(\phi)(1 - |\nabla \phi|) + \lambda_m \delta_\varepsilon^2(\phi)|\nabla \phi| = 0. \tag{3.21}$$

Therefore,

$$\lambda_m = -\frac{\int_\Omega \delta_\varepsilon(\phi) S(\phi)(1 - |\nabla \phi|)}{\int_\Omega \delta_\varepsilon^2(\phi)|\nabla \phi|}. \tag{3.22}$$

The level set function is updated by the local level set method (PENG et al., 1999) which consists in to delimit the regions Ω_T in the domain where the equations will be solved, as presented in Figure 6. The use of this technology strongly decreases the computational efforts related to the solution of the advection and re-initialization equations of the level set function and also avoids numerical problems close to the boundaries.

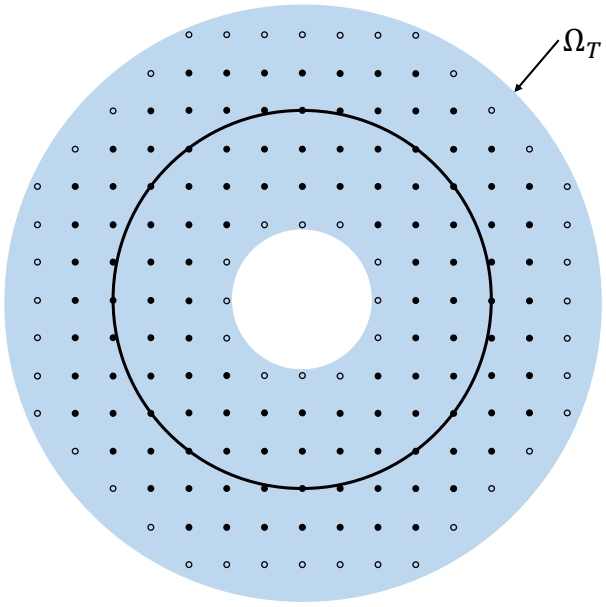

Figure 6 – Representation of the local level set method.

Accordingly, three tubes are constructed around the interface in which PDEs for the level set function is solved, such as $T_i = \{\mathbf{x} : |\phi(\mathbf{x}, t)| \leq \epsilon_i\}$, $i = 1, ..., 3$ where for $h = \min(\Delta x, \Delta y)$, $\epsilon_1 = 12h$, $\epsilon_2 = 8h$ and $\epsilon_3 = 4h$. A cut-off function $c(\phi)$ is also introduced in Eq. (3.10), as follows:

$$\frac{\partial \phi}{\partial t} + c(\phi)\mathbf{u} \cdot \nabla \phi = 0, \tag{3.23}$$

where,

$$c(\phi) = \begin{cases} 1, & \text{if } |\phi| \leq \epsilon_2; \\ (|\phi| - \epsilon_1)^2(2|\phi| + \epsilon_1 - 3\epsilon_2)/(\epsilon_1 - \epsilon_2), & \text{if } \epsilon_2 < |\phi| \leq \epsilon_1; \\ 0, & \text{if } |\phi| > \epsilon_1. \end{cases} \tag{3.24}$$

The temporal evolution of the level set function is performed using a Total Variation Diminishing (TVD) Runge Kutta (RK) method of third-order, as described by Shu and Osher (1988). This method guarantees that this solution will not affect the method's overall order. In addition, this method presents great stability due to the reduction of error accumulation over the iterations. This Runge-Kutta method is performed in three steps,

$$\begin{cases} \tilde{\phi}_{i,j}^{n+1} = \phi_{i,j}^{n} - \Delta t \; c\left(\phi_{i,j}^{n}\right) \mathbf{u}_{i,j}^{n} \cdot \nabla \phi_{i,j}^{n} \\ \tilde{\phi}_{i,j}^{n+\frac{1}{2}} = \frac{3}{4}\phi_{i,j}^{n} + \frac{1}{4}\tilde{\phi}_{i,j}^{n+1} - \frac{1}{4}\Delta t \; c\left(\tilde{\phi}_{i,j}^{n+1}\right) \mathbf{u}_{i,j}^{n+1} \cdot \nabla \tilde{\phi}_{i,j}^{n+1} \\ \phi_{i,j}^{n+1} = \frac{1}{3}\phi_{i,j}^{n} + \frac{2}{3}\tilde{\phi}_{i,j}^{n+\frac{1}{2}} - \frac{2}{3}\Delta t \; c\left(\tilde{\phi}_{i,j}^{n+\frac{1}{2}}\right) \mathbf{u}_{i,j}^{n+\frac{1}{2}} \cdot \nabla \tilde{\phi}_{i,j}^{+\frac{1}{2}} \end{cases} \tag{3.25}$$

where, the superscript $n+1$ represents the current time, n represents the previous time and $n+\frac{1}{2}$ is the mean time between n and $n+1$.

In order to guarantee a great approximation of the spatial derivatives, the convective term, $\mathbf{u}_{i,j}^{(k)} \cdot \nabla \phi_{i,j}^{(k)}$, are computed using a fifth-order Weighted Essentially Non-Oscillatory (WENO) method for biased derivative approximations, in conjunction with Godunov and upwind schemes (OSHER; FEDKIW, 2003), in which the choice of an approximation for spatial derivatives is based on the sign of u and v. For example, if $u > 0$, the values of ϕ are moving from left to right, therefore values to the left of $x_{i,j}$ must be used to determine the derivative of ϕ. Similarly, if $u < 0$, the values of ϕ are moving from right to left, therefore values to the right of $x_{i,j}$ must be used to determine the derivative of ϕ. Thus,

$$\begin{aligned} \mathbf{u}_{i,j}^{(k)} \cdot \nabla \phi_{i,j}^{(k)} = \min\left(\bar{u}_{i,j}^{(k)}, 0\right) D_x^{+} \phi_{i,j}^{(k)} + \max\left(\bar{u}_{i,j}^{(k)}, 0\right) D_x^{-} \phi_{i,j}^{(k)} + \\ \min\left(\bar{v}_{i,j}^{(k)}, 0\right) D_y^{+} \phi_{i,j}^{(k)} + \max\left(\bar{v}_{i,j}^{(k)}, 0\right) D_y^{-} \phi_{i,j}^{(k)}, \end{aligned} \tag{3.26}$$

where $D_x^{+}\phi$, $D_x^{-}\phi$, D_y^{+} and $D_y^{-}\phi$ are spatial derivatives from the level set function in the x and y directions obtained by fifth-order WENO; $\bar{u}_{i,j}^{(k)}$ and $\bar{v}_{i,j}^{(k)}$ are the components of the velocity field, computed at the cell's center via third-order Lagrange interpolation.

The re-initialization of the level set function follows the same steps as the advection. This strategy is similar to the one used by Sussman (1994). Here, t is exchanged for τ, and

$\phi_{i,j}^{(0)} = \phi_{i,j}^{n+1}$ is the level set function after advection by Eq. (3.23) via Eq. (3.25). Therefore,

$$\begin{cases} \tilde{\phi}_{i,j}^{(1)} = \tilde{\phi}_{i,j}^{(0)} - \Delta\tau L\left(\tilde{\phi}_{i,j}^{(0)}\right) \\ \tilde{\phi}_{i,j}^{(2)} = \frac{3}{4}\tilde{\phi}_{i,j}^{(0)} + \frac{1}{4}\tilde{\phi}_{i,j}^{(1)} - \frac{1}{4}\Delta\tau L\left(\tilde{\phi}_{i,j}^{(1)}\right) \\ \tilde{\phi}_{i,j}^{(3)} = \frac{1}{3}\tilde{\phi}_{i,j}^{(0)} + \frac{2}{3}\tilde{\phi}_{i,j}^{(2)} - \frac{2}{3}\Delta\tau L\left(\tilde{\phi}_{i,j}^{(2)}\right) \end{cases} \tag{3.27}$$

where,

$$\begin{aligned} L\left(\tilde{\phi}_{i,j}^{(k)}\right) = S_{\varepsilon}^{+}\left(\tilde{\phi}_{i,j}^{(0)}\right)\left(\sqrt{\max\left[\left(a_{i,j}^{+}\right)^2, \left(b_{i,j}^{-}\right)^2\right] + \max\left[\left(c_{i,j}^{+}\right)^2, \left(d_{i,j}^{-}\right)^2\right]} - 1\right) \\ + S_{\varepsilon}^{-}\left(\tilde{\phi}_{i,j}^{(0)}\right)\left(\sqrt{\max\left[\left(a_{i,j}^{-}\right)^2, \left(b_{i,j}^{+}\right)^2\right] + \max\left[\left(c_{i,j}^{-}\right)^2, \left(d_{i,j}^{+}\right)^2\right]} - 1\right), \end{aligned} \tag{3.28}$$

the sign function is

$$S_{\varepsilon}(\phi_{i,j}) = \frac{\phi_{i,j}}{\sqrt{\phi_{i,j}^2 + |\nabla\phi|_{i,j}^2 \min(\Delta x, \Delta y)^2}}, \tag{3.29}$$

and the coefficients are:

$$\begin{aligned} a_{i,j}\left(\tilde{\phi}_{i,j}^{(k)}\right) &= D_x^{-}\tilde{\phi}_{i,j}^{(k)}, \\ b_{i,j}\left(\tilde{\phi}_{i,j}^{(k)}\right) &= D_x^{+}\tilde{\phi}_{i,j}^{(k)}, \\ c_{i,j}\left(\tilde{\phi}_{i,j}^{(k)}\right) &= D_y^{-}\tilde{\phi}_{i,j}^{(k)}, \\ d_{i,j}\left(\tilde{\phi}_{i,j}^{(k)}\right) &= D_y^{+}\tilde{\phi}_{i,j}^{(k)}. \end{aligned} \tag{3.30}$$

Finally, the conservation of the droplet area is computed from the Eq. (3.27), as follows:

$$\phi_{i,j}^{n+1} = \tilde{\phi}_{i,j}^{(3)} + \Delta\tau\lambda_{mi,j}\delta_{\varepsilon}\left(\tilde{\phi}_{i,j}^{(0)}\right)\left|\nabla\tilde{\phi}_{i,j}^{(0)}\right|. \tag{3.31}$$

This procedure is repeated until the $|\nabla\phi| \approx 1$ in the tube regions, i.e. the steady state of Eq. (3.20).

3.3 Closest point method

The closest point method is used to solve partial differential equations on the surfaces. This method uses standard numerical approaches, such as finite differences, finite volumes, or finite elements, in order to solve an embedding partial differential equation that is a natural extension of the original surface equation. The closest point method consists of precisely extending the functions defined on surfaces to their neighborhood (tube) so

that these functions remain constant along the normal direction (RUUTH; MERRIMAN, 2008). Thus, the embedding PDE is formed by replacing intrinsic surface gradients with standard gradients and the solution is computed on the tube surrounding the surface. For instance,

$$\nabla_s(f(\mathbf{x}_{i,j})) = \nabla(f(\mathbf{cp}(\mathbf{x}_{i,j}))) \tag{3.32}$$

and

$$\nabla_s \cdot (\nabla_s(f(\mathbf{x}_{i,j}))) = \nabla \cdot [\nabla(f(\mathbf{cp}(\mathbf{x}_{i,j})))] = \nabla^2(f(\mathbf{cp}(\mathbf{x}_{i,j}))). \tag{3.33}$$

The principles of equivalence of gradients and other differential operators yield a way of dealing with surface differential operators by evaluating the corresponding differential operator in the embedding space (MACDONALD; RUUTH, 2010). Thus, the constant extension of surface properties in the normal direction is done by using the closest point representation of the surface. For any point $\mathbf{x}$ in Ω, let $\mathbf{cp}(\mathbf{x})$ denote the closest point to $\mathbf{x}$ in the surface Γ (RUUTH; MERRIMAN, 2008).

In Figure 7, note that the closest point to $\mathbf{x}_1$ at the interface, $\mathbf{cp}(\mathbf{x}_1)$ corresponds to the position in the normal direction of $\mathbf{x}_1$, where $\phi(\mathbf{cp}(\mathbf{x}_1), t) = 0$. Another important note is that the distance between $\mathbf{x}_1$ and $\mathbf{cp}(\mathbf{x}_1)$ corresponds to the shortest distance between $\mathbf{x}_1$ and the interface, in other words, it is the level set function $\phi(\mathbf{x}_1, t)$.

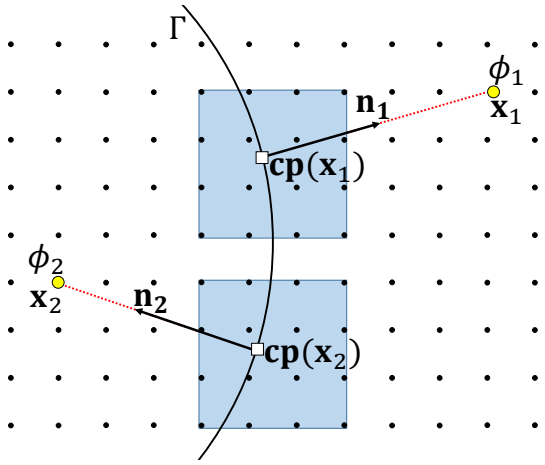

Figure 7 – Closest point method: a geometrical representation. Yellow dots are grid points with their corresponding closest point on the surface as white square dots. Dots into the blue region are used for interpolation of the surface property value (white square dot). The interface normal vectors are drawn as arrow ended segments.

Thus, considering the unit normal vector in a two-dimensional domain, the coordinates of the closest points to all points of the domain, $\mathbf{cp}(\mathbf{x}_{i,j})$, can be determined by

similarity of triangles, as follows:

$$x\left(\mathbf{cp}\left(\mathbf{x}_{i,j}\right)\right) = x_{i,j} - \phi\left(\mathbf{x}_{i,j}, t\right) n_x, \tag{3.34}$$

$$y\left(\mathbf{cp}\left(\mathbf{x}_{i,j}\right)\right) = y_{i,j} - \phi\left(\mathbf{x}_{i,j}, t\right) n_y, \tag{3.35}$$

where n_x and n_y are the unit normal vector components in x and y directions, respectively.

The $\mathbf{cp}\left(\mathbf{x}_{i,j}\right)$ coordinates obtained from Eqs. (3.34) and (3.35) will hardly match with discretized points of the computational mesh. Therefore, the closest point extension needs an interpolation step, and the order of the interpolation should be sufficiently high so that the interpolation errors do not dominate the solution (RUUTH; MERRIMAN, 2008). In this work, the Lagrange two-dimensional interpolation of third order is used, as illustrated by dots into the blue region in Figure 7.

The closest point method is applied in the following steps:

- To set the computational domain, Ω_T, as a tube around the surface;
- To replace surface gradients and divergences by gradients and divergent patterns;
- To extend the initial surface data to the computational domain, Ω_T, using the closest point method;
- To discretize the embedding PDE using standard finite differences in a Cartesian mesh at the computational domain Ω_T.

For convenience, the nomenclature to refer to the closest point of any mesh point, $\mathbf{cp}\left(\mathbf{x}_{i,j}\right)$ is replaced by just, $\mathbf{cp}_{i,j}$. For example, $\nabla_s f = \nabla f\left(\mathbf{cp}_{i,j}\right)$.

3.4 Coupling the level set method with the governing equations

In the simulation of multiphase systems, discontinuities can occur due to differences between the properties of the fluids and the stress jump across the interface, for example. However, the use of the level set method allows to smooth out these discontinuities by using the Heaviside and Dirac delta functions. Applying the Eqs. (3.12), (3.13), (3.14) and (3.16) in Eqs. (2.1) (2.24), (2.25), (2.26) and (2.27), it is obtained, respectively:

$$\nabla \cdot [\zeta_\varepsilon(\phi)\nabla\psi] = 0, \tag{3.36}$$

$$\nabla \cdot \mathbf{u} = 0, \tag{3.37}$$

$$\frac{D\mathbf{u}}{Dt} = -\nabla p + \frac{1}{Re}\nabla \cdot [\lambda_\varepsilon(\phi)(\nabla \mathbf{u} + \nabla \mathbf{u}^T)] + \frac{1}{CaRe}\delta_\varepsilon(\phi)(|\nabla\phi|\nabla_s\sigma - \kappa\sigma\nabla\phi) + \frac{Ca_{mag}}{CaRe}\left(\zeta_\varepsilon(\phi) - 1\right)\mathbf{H}\cdot\nabla\mathbf{H}, \tag{3.38}$$

$$\sigma(c) = 1 + E\ln\left(1 - Xc\right), \tag{3.39}$$

and

$$\frac{\partial c}{\partial t} = -\nabla_s \cdot (c\mathbf{u}_s) + \frac{1}{Pe}\nabla_s^2 c - c(\nabla_s \cdot \mathbf{n})(\mathbf{u}\cdot\mathbf{n}). \tag{3.40}$$

3.5 Magnetic potential field numerical solution

The Eq. (3.36) is discretized using the finite difference method, as described in section 3.1. Thus,

$$a_{\psi_{i,j}}\psi_{i-1,j} + b_{\psi_{i,j}}\psi_{i,j-1} + c_{\psi_{i,j}}\psi_{i,j} + d_{\psi_{i,j}}\psi_{i+1,j} + e_{\psi_{i,j}}\psi_{i,j+1} = 0 \tag{3.41}$$

where, the coefficients are

$$a_{\psi_{i,j}} = \frac{\zeta_\varepsilon(\phi)_{i-1/2,j}}{\Delta x^2}, \tag{3.42}$$

$$b_{\psi_{i,j}} = \frac{\zeta_\varepsilon(\phi)_{i,j-1/2}}{\Delta y^2}, \tag{3.43}$$

$$c_{\psi_{i,j}} = -\frac{\zeta_\varepsilon(\phi)_{i-1/2,j} + \zeta_\varepsilon(\phi)_{i+1/2,j}}{\Delta x^2} - \frac{\zeta_\varepsilon(\phi)_{i,j-1/2} + \zeta_\varepsilon(\phi)_{i,j+1/2}}{\Delta y^2}, \tag{3.44}$$

$$d_{\psi_{i,j}} = \frac{\zeta_\varepsilon(\phi)_{i+1/2,j}}{\Delta x^2} \tag{3.45}$$

and

$$e_{\psi_{i,j}} = \frac{\zeta_\varepsilon(\phi)_{i,j+1/2}}{\Delta y^2}. \tag{3.46}$$

The index $(i-1/2, j)$, $(i+1/2, j)$, $(i, j-1/2)$ and $(i, j+1/2)$ refers, respectively, to the left, right, bottom, and top boundaries of the cell presented in Fig. 3. Thus, in these positions, $\zeta_\varepsilon(\phi)$ is computed by the harmonic average of neighboring points, in order to avoid instabilities. For example, $\zeta_\varepsilon(\phi)_{i+1/2,j}$ is computed by harmonic average between $\zeta_\varepsilon(\phi)_{i+1,j}$ and $\zeta_\varepsilon(\phi)_{i,j}$.

The boundary conditions for the potential field are applied as heterogeneous Neumann conditions, representing a Dirichlet condition for the magnetic field, $\nabla\phi = -\mathbf{H}_0$.

At the right boundary, Fig. 8, this condition is represented by $\partial\psi/\partial x = -\mathrm{H}_{0x}$, which is discretized by finite differences, as follows:

$$\frac{\psi_{N_x+1,1:N_y} - \psi_{N_x,1:N_y}}{\Delta x} = -\mathrm{H}_{0x}, \tag{3.47}$$

therefore,

$$\psi_{N_x+1,1:N_y} = \psi_{N_x,1:N_y} - \Delta x \mathrm{H}_{0x}. \tag{3.48}$$

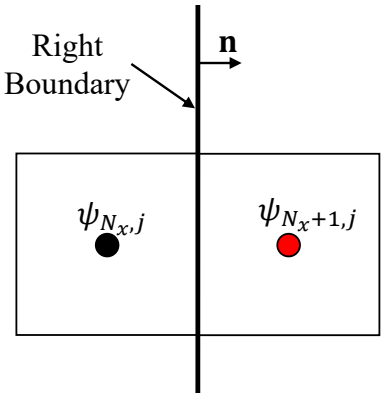

Figure 8 – Right boundary. The red dots correspond to points outside the domain, but which are used to solve Eq. (3.41).

Applying the boundary condition of Eq. (3.48) in Eq. (3.41) for all right border of the domain $[N_x, 1 : N_y]$ it is obtained that:

$$\begin{cases} c_{\psi_{i,j}} = c_{\psi_{i,j}} + d_{\psi_{i,j}}, \\ \psi_{i+1,j} = -\Delta x \mathrm{H}_{0x}. \end{cases} \tag{3.49}$$

For other surfaces, the boundary conditions can be easily obtained in a similar way.

3.6 Projection method

One of the major difficulties in solving transient incompressible flow problems is the fact that there is no explicit equation for pressure. When the flow is compressible, the pressure field is a function of two independent thermodynamic properties (such as temperature and density, for example). In this case, it is necessary to solve a state equation to compute the pressure, which then enters in the motion equation. In incompressible flows, pressure has no thermodynamic meaning and, therefore, there is no constitutive equation to determine it. Thus, the velocity field must satisfy the condition of incompressibility. To work around this problem, one alternative is to use projection methods, which consist of decoupling the pressure and velocity computation in the motion equation.

In the projection method presented here, velocity and pressure fields are computed in two stages. First, a trial velocity field is computed using the motion equation neglecting the effects of the pressure field and the incompressibility condition, obtaining an intermediate velocity field $\mathbf{u}^*$. In the second stage, the trial velocity field is projected in the space of the vector fields with zero divergences to calculate the trial pressure. From there, the correction of the pressure and velocity fields is made satisfying the incompressibility condition, obtaining p and $\mathbf{u}$.

A semi-explicit strategy is adopted to address the non-linearity of the diffusive term when the viscosity ratio λ is not constant. This strategy, already presented by Xu, Yang and Lowengrub (2012), Xu and Ren (2014), Xu, Shi and Lai (2018), Cunha et al. (2018), consists of add the viscous term $\left(\bar{\lambda}/2Re\right)\nabla^2\mathbf{u}^*$ and subtract $\left(\bar{\lambda}/2Re\right)\nabla^2\tilde{\mathbf{u}}^{n+1}$ in the motion equation, in which $\bar{\lambda} = \max\{1, \lambda_\varepsilon(\phi)\}$ and $\tilde{\mathbf{u}}^{n+1}$ is the extrapolated velocity from the previous time. It should be noted that both $\mathbf{u}^*$ and $\tilde{\mathbf{u}}$ are trial velocities at the current time. This approach preserves the symmetric of the equations of $\mathbf{u}^*$, which would happen naturally if the viscosity were constant, without the need for this approximation.

Here, Eqs. (3.37) and (3.38) are broken down into three steps. First, the Eq. (3.38) is divided into two equations using a modified semi-implicit Crank–Nicolson scheme and the second-order-explicit Adams-Bashforth scheme for the convective terms, as follows:

$$\begin{aligned}\frac{\mathbf{u}^* - \mathbf{u}^n}{\Delta t} = -[(\mathbf{u}\cdot\nabla)\mathbf{u}]^{n+1/2} + \frac{1}{Re}\nabla\cdot\left[\lambda_\varepsilon(\phi)(\nabla\mathbf{u} + \nabla\mathbf{u}^T)\right]^{n+1/2} \\ + \frac{\bar{\lambda}}{2Re}\nabla^2\mathbf{u}^* - \frac{\bar{\lambda}}{2Re}\nabla^2\tilde{\mathbf{u}}^{n+1} + \frac{1}{CaRe}\left[\delta_\varepsilon(\phi)\left(|\nabla\phi|\nabla_s\sigma - \sigma\kappa\nabla\phi\right)\right]^{n+1/2} \\ + \frac{Ca_{mag}}{CaRe}\left[\left(\zeta_\varepsilon(\phi) - 1\right)\mathbf{H}\cdot\nabla\mathbf{H}\right]^{n+1/2},\end{aligned} \tag{3.50}$$

and

$$\frac{\mathbf{u}^{n+1} - \mathbf{u}^*}{\Delta t} = -\nabla\chi^{n+1}, \tag{3.51}$$

in which Δt is the time step, χ is the auxiliary variable to compute the pressure field,

$$\nabla^2\tilde{\mathbf{u}}^{n+1} = 2\nabla^2\mathbf{u}^n - \nabla^2\mathbf{u}^{n-1} \tag{3.52}$$

and

$$[(\mathbf{u}\cdot\nabla)\mathbf{u}]^{n+1/2} = \frac{3}{2}[(\mathbf{u}\cdot\nabla)\mathbf{u}]^n - \frac{1}{2}[(\mathbf{u}\cdot\nabla)\mathbf{u}]^{n-1}. \tag{3.53}$$

Thus, an intermediate velocity field is solved by Eq. (3.50).

In the second step, we take the divergent of Eq. (3.51) and force $\mathbf{u}^{n+1}$ to be incompressible to provide a Poisson equation for the trial pressure χ of the form

$$\nabla^2\chi^{n+1} = \frac{\nabla\cdot\mathbf{u}^*}{\Delta t}. \tag{3.54}$$

After solving Eq.(3.54), one computes $\mathbf{u}^{n+1}$ using Eq.(3.51). Finally, substituting Eq. (3.51) in Eq. (3.50), the pressure field equation is obtained as follows

$$p^{n+1/2} = \chi^{n+1} - \frac{1}{2Re}\nabla \cdot \mathbf{u}^*. \tag{3.55}$$

3.6.1 Spatial discretization of the projection method

The governing equations are spatially discretized using the finite difference method and the closest point method for the surface operators and quantities, as described in sections 3.1 and 3.3, respectively. These equations have terms in common and therefore are rewritten as a function of those terms. Thus, the Eqs. (3.50), (3.54) and (3.51) become, respectively:

$$\mathbf{u}^*_{i,j} - \frac{\bar{\lambda}\Delta t}{2Re}\nabla^2\mathbf{u}^*_{i,j} = \mathbf{u}^n_{i,j} + \Delta t\left(\boldsymbol{\mathcal{G}}\left(\mathbf{u}^n\right)_{i,j} + \frac{1}{CaRe}\mathbf{F}_{si,j}^{n+1/2} + \frac{Ca_{mag}}{CaRe}\mathbf{F}_{magi,j}^{n+1/2}\right), \tag{3.56}$$

$$\left(\frac{\chi^{n+1}_{i+1,j} + \chi^{n+1}_{i-1,j} - 2\chi^{n+1}_{i,j}}{\Delta x^2}\right) + \left(\frac{\chi^{n+1}_{i,j+1} + \chi^{n+1}_{i,j-1} - 2\chi^{n+1}_{i,j}}{\Delta y^2}\right) = \frac{\nabla \cdot \mathbf{u}^*_{i,j}}{\Delta t}, \tag{3.57}$$

$$\mathbf{u}^{n+1}_{i,j} = \mathbf{u}^*_{i,j} - \Delta t\nabla\chi^{n+1}_{i,j}, \tag{3.58}$$

where the most complex terms,

$$\boldsymbol{\mathcal{G}}\left(\mathbf{u}^n\right)_{i,j} = -[(\mathbf{u}\cdot\nabla)\mathbf{u}]^{n+1/2}_{i,j} + \frac{1}{Re}\nabla\cdot[\lambda_\varepsilon(\phi)(\nabla\mathbf{u} + \nabla\mathbf{u}^T)]^{n+1/2}_{i,j} - \frac{\bar{\lambda}}{2Re}\nabla^2\tilde{\mathbf{u}}^{n+1}_{i,j}, \tag{3.59}$$

$$\mathbf{F}_{si,j}^{n+1/2} = \delta_\varepsilon\left(\phi^{n+1/2}_{i,j}\right)\left(|\nabla\phi|^{n+1/2}_{i,j}\nabla\sigma\left(\mathbf{cp}^{n+1/2}_{i,j}\right) - \sigma^{n+1/2}_{i,j}\kappa^{n+1/2}_{i,j}\nabla\phi^{n+1/2}_{i,j}\right), \tag{3.60}$$

and

$$\mathbf{F}_{magi,j}^{n+1/2} = \left(\zeta_\varepsilon\left(\phi^{n+1/2}_{i,j}\right) - 1\right)\left(\mathbf{H}\cdot\nabla\mathbf{H}\right)^{n+1/2}_{i,j}, \tag{3.61}$$

are discretized in the sequence. For convenience, only the x-direction components (subscript "x") are presented, since for y-direction, the components can be easily obtained by following the same steps. Thus, the component $\mathcal{G}\left(u^n_{i,j}\right)$ in Eq. (3.59) is determined using the Eqs. (3.52), (3.53), as follows:

$$
\begin{aligned}
\mathcal{G}\left(u_{i,j}^{n}\right) = & -\frac{3}{2}\left[u_{i,j}^{n}\left(\frac{\partial u^{n}}{\partial x}\right)+\frac{\left(v_{i,j}^{n}+v_{i+1,j}^{n}+v_{i+1,j-1}^{n}+v_{i,j-1}^{n}\right)}{4}\left(\frac{\partial u^{n}}{\partial y}\right)\right] \\
& +\frac{1}{2}\left[u_{i,j}^{n-1}\left(\frac{\partial u^{n-1}}{\partial x}\right)+\frac{\left(v_{i,j}^{n-1}+v_{i+1,j}^{n-1}+v_{i+1,j-1}^{n-1}+v_{i,j-1}^{n-1}\right)}{4}\left(\frac{\partial u^{n-1}}{\partial y}\right)\right] \\
& +\frac{3}{2Re}\left[\frac{2\lambda_{\varepsilon}(\phi_{i+1/2,j}^{n})(u_{i+1,j}^{n}-u_{i,j}^{n})-2\lambda_{\varepsilon}(\phi_{i-1/2,j}^{n})(u_{i,j}^{n}-u_{i-1,j}^{n})}{\Delta x^{2}}\right] \\
& +\frac{3}{2Re}\left[\frac{\lambda_{\varepsilon}(\phi_{i,j+1/2}^{n})(u_{i,j+1}^{n}-u_{i,j}^{n})-\lambda_{\varepsilon}(\phi_{i,j-1/2}^{n})(u_{i,j}^{n}-u_{i,j-1}^{n})}{\Delta y^{2}}\right] \\
& +\frac{3}{2Re}\left[\frac{\lambda_{\varepsilon}(\phi_{i,j+1/2}^{n})(v_{i+1,j}^{n}-v_{i,j}^{n})-\lambda_{\varepsilon}(\phi_{i,j-1/2}^{n})(v_{i+1,j-1}^{n}-v_{i,j-1}^{n})}{\Delta y\Delta x}\right] \\
& -\frac{1}{2Re}\left[\frac{2\lambda_{\varepsilon}(\phi_{i+1/2,j}^{n-1})(u_{i+1,j}^{n-1}-u_{i,j}^{n-1})-2\lambda_{\varepsilon}(\phi_{i-1/2,j}^{n-1})(u_{i,j}^{n-1}-u_{i-1,j}^{n-1})}{\Delta x^{2}}\right] \\
& -\frac{1}{2Re}\left[\frac{\lambda_{\varepsilon}(\phi_{i,j+1/2}^{n-1})(u_{i,j+1}^{n-1}-u_{i,j}^{n-1})-\lambda_{\varepsilon}(\phi_{i,j-1/2}^{n-1})(u_{i,j}^{n-1}-u_{i,j-1}^{n-1})}{\Delta y^{2}}\right] \\
& -\frac{1}{2Re}\left[\frac{\lambda_{\varepsilon}(\phi_{i,j+1/2}^{n-1})(v_{i+1,j}^{n-1}-v_{i,j}^{n-1})-\lambda_{\varepsilon}(\phi_{i,j-1/2}^{n-1})(v_{i+1,j-1}^{n-1}-v_{i,j-1}^{n-1})}{\Delta y\Delta x}\right] \\
& -\frac{\bar{\lambda}}{Re}\left(\frac{u_{i+1,j}^{n}+u_{i-1,j}^{n}-2u_{i,j}^{n}}{\Delta x^{2}}+\frac{u_{i,j+1}^{n}+u_{i,j-1}^{n}-2u_{i,j}^{n}}{\Delta y^{2}}\right) \\
& +\frac{\bar{\lambda}}{2Re}\left(\frac{u_{i+1,j}^{n-1}+u_{i-1,j}^{n-1}-2u_{i,j}^{n-1}}{\Delta x^{2}}+\frac{u_{i,j+1}^{n-1}+u_{i,j-1}^{n-1}-2u_{i,j}^{n-1}}{\Delta y^{2}}\right),
\end{aligned}
\tag{3.62}
$$

The convective term in Eq. (3.62) presents unwanted oscillations since its numerical computation is not always numerically accurate. Therefore $\partial u/\partial x$ and $\partial u/\partial y$ are computed by second order ENO, as described by Osher and Fedkiw (2003).

The component ${F_{s_x}}_{i,j}^{n+1/2}$ of the Eq. (3.60) is discretized in conjunction with the closest point method, described in section 3.3. Therefore,

$$
\begin{aligned}
{F_{s_x}}_{i,j}^{n+1/2} = & \,\delta_{\varepsilon}\left(\frac{\phi_{i,j}^{n+1/2}+\phi_{i+1,j}^{n+1/2}}{2}\right) \\
& \left[\left(\frac{|\nabla\phi|_{i,j}^{n+1/2}+|\nabla\phi|_{i+1,j}^{n+1/2}}{2}\right)\left(\frac{\sigma\left(\mathbf{cp}_{i+1,j}^{n+1/2}\right)-\sigma\left(\mathbf{cp}_{i,j}^{n+1/2}\right)}{\Delta x}\right)\right. \\
& \left.-\left(\frac{\sigma_{i+1,j}^{n+1/2}+\sigma_{i,j}^{n+1/2}}{2}\right)\left(\frac{\kappa_{i+1,j}^{n+1/2}+\kappa_{i,j}^{n+1/2}}{2}\right)\left(\frac{\phi_{i+1,j}^{n+1/2}-\phi_{i,j}^{n+1/2}}{\Delta x}\right)\right],
\end{aligned}
\tag{3.63}
$$

where the curvature is

$$
\kappa_{i,j} = \frac{n_{x_{i+1,j}}-n_{x_{i-1,j}}}{2\Delta x}+\frac{n_{y_{i,j+1}}-n_{y_{i,j-1}}}{2\Delta y},
\tag{3.64}
$$

in which

$$n_{xi,j} = \frac{\phi_{xi,j}}{|\nabla\phi_{i,j}|}, \tag{3.65}$$

$$n_{y_{i,j}} = \frac{\phi_{y_{i,j}}}{|\nabla\phi_{i,j}|}, \tag{3.66}$$

$$\phi_{xi,j} = \frac{\phi_{i+1,j} - \phi_{i-1,j}}{2\Delta x}, \tag{3.67}$$

$$\phi_{y_{i,j}} = \frac{\phi_{i,j+1} - \phi_{i,j-1}}{2\Delta y}, \tag{3.68}$$

and

$$|\nabla\phi|_{i,j}^{n+1/2} = \sqrt{\left(\frac{\phi_{i+1,j}^{n+1/2} - \phi_{i-1,j}^{n+1/2}}{2\Delta x}\right)^2 + \left(\frac{\phi_{i,j+1}^{n+1/2} - \phi_{i,j-1}^{n+1/2}}{2\Delta y}\right)^2}. \tag{3.69}$$

To discretize the component ${F_{mag_x}}_{i,j}^{n+1/2}$ of the Eq. (3.61) it is necessary to define $\mathbf{H}_{i,j} = \left(H_{xi,j}, H_{y_{i,j}}\right)$, where $\mathbf{H}_{i,j} = -\nabla\psi_{i,j}$. Therefore,

$$H_{xi,j} = -\left.\frac{\partial\psi}{\partial x}\right|_{i+1/2,j} = -\frac{\psi_{i+1,j} - \psi_{i,j}}{\Delta x}, \tag{3.70}$$

$$H_{y_{i,j}} = -\left.\frac{\partial\psi}{\partial y}\right|_{i,j+1/2} = -\frac{\psi_{i,j+1} - \psi_{i,j}}{\Delta y}, \tag{3.71}$$

and

$$\begin{aligned} {F_{mag_x}}_{i,j}^{n+1/2} = \left(\frac{\zeta_\varepsilon\left(\phi_{i,j}^{n+1/2}\right) + \zeta_\varepsilon\left(\phi_{i+1,j}^{n+1/2}\right)}{2} - 1\right)\Bigg[{H_{xi,j}}^{n+1/2}\left(\frac{{H_{xi+1,j}}^{n+1/2} - {H_{xi-1,j}}^{n+1/2}}{2\Delta x}\right) + \\ \frac{\left({H_{y_{i,j}}}^{n+1/2} + {H_{y_{i+1,j}}}^{n+1/2} + {H_{y_{i+1,j-1}}}^{n+1/2} + {H_{y_{i,j-1}}}^{n+1/2}\right)}{4}\left(\frac{{H_{xi,j+1}}^{n+1/2} - {H_{xi,j-1}}^{n+1/2}}{2\Delta y}\right)\Bigg]. \end{aligned} \tag{3.72}$$

Discretizing the left side of Eq. (3.56), using Eqs. (3.62), (3.63), and (3.72), reordering and grouping the terms in the x-direction,

$$a_{u_{i,j}}u_{i-1,j}^* + b_{u_{i,j}}u_{i,j-1}^* + c_{u_{i,j}}u_{i,j}^* + d_{u_{i,j}}u_{i+1,j}^* + e_{u_{i,j}}u_{i,j+1}^* = f_{u_{i,j}} \tag{3.73}$$

where, the coefficients are,

$$a_{u_{i,j}} = d_{u_{i,j}} = -\frac{\bar{\lambda}\Delta t}{2Re\Delta x^2}, \tag{3.74}$$

$$b_{u_{i,j}} = e_{u_{i,j}} = -\frac{\bar{\lambda}\Delta t}{2Re\Delta y^2}, \tag{3.75}$$

$$c_{u_{i,j}} = 1 + \frac{\bar{\lambda}\Delta t}{Re\Delta x^2} + \frac{\bar{\lambda}\Delta t}{Re\Delta y^2}, \tag{3.76}$$

and

$$f_{u_{i,j}} = u^n_{i,j} + \Delta t \left(\mathcal{G}\left(u^n_{i,j}\right) + \frac{1}{CaRe} F_{s_x}{}^{n+1/2}_{i,j} + \frac{Ca_{mag}}{CaRe} F_{mag_x}{}^{n+1/2}_{i,j} \right). \tag{3.77}$$

Now, discretizing Eq. (3.57), we have:

$$a_{\chi_{i,j}} \chi^{n+1/2}_{i-1,j} + b_{\chi_{i,j}} \chi^{n+1/2}_{i,j-1} + c_{\chi_{i,j}} \chi^{n+1/2}_{i,j} + d_{\chi_{i,j}} \chi^{n+1/2}_{i+1,j} + e_{\chi_{i,j}} \chi^{n+1/2}_{i,j+1} = f_{\chi_{i,j}}, \tag{3.78}$$

where the coefficients are,

$$a_{\chi_{i,j}} = d_{\chi_{i,j}} = \frac{1}{\Delta x^2}, \tag{3.79}$$

$$b_{\chi_{i,j}} = d_{\chi_{i,j}} = \frac{1}{\Delta y^2}, \tag{3.80}$$

$$c_{\chi_{i,j}} = -\frac{2}{\Delta x^2} - \frac{2}{\Delta y^2}, \tag{3.81}$$

and

$$f_{\chi_{i,j}} = \frac{1}{\Delta t} \left(\frac{u^*_{i,j} - u^*_{i-1,j}}{\Delta x} + \frac{v^*_{i,j} - v^*_{i,j-1}}{\Delta y} \right). \tag{3.82}$$

Discretizing the x-components of Eq. (3.58), it is obtained

$$u^{n+1}_{i,j} = u^*_{i,j} - \Delta t \left(\frac{\chi^{n+1}_{i+1,j} - \chi^{n+1}_{i,j}}{\Delta x} \right). \tag{3.83}$$

Finally, Eq. (3.55) is discretized, obtaining

$$p^{n+1/2}_{i,j} = \chi^{n+1}_{i,j} - \frac{1}{2Re} \left(\frac{u^*_{i,j} - u^*_{i-1,j}}{\Delta x} + \frac{v^*_{i,j} - v^*_{i,j-1}}{\Delta y} \right). \tag{3.84}$$

Thus, the equations for fluid motion are solved in the following order: Eqs. (3.73) and a similar equation for y-direction, to compute the trial velocity field, $\mathbf{u}^*$; Eq. (3.78) to compute χ^{n+1}; Eq. (3.83) and a similar equation for y-direction, to compute velocity field, $\mathbf{u}^{n+1}$; and finally, Eq. (3.84) to compute pressure field, $p^{n+1/2}$. All linear systems presented so far are solved by the Direct solution via Fourier Analysis, as shown in Annex A.

3.7 Boundary and initial conditions

Considering simple shear flow, the periodic boundary condition for velocity and pressure fields are used at the side boundaries. At the top and bottom boundaries, are considered the no-slip condition at the channel walls, and the non-homogeneous Dirichlet boundary condition is applied to the velocity field **u**. For the pressure field, Homogeneous Neumann boundary conditions are used.

As shown in Figure 3, for cells located at the top and bottom boundaries, the velocity components v and v^* coincide with the boundaries (positions where $j = 0$ or $j = N_y$) and have the same wall velocity. Therefore, such points are not part of the solution domain of v and v^*. However, there are no points to evaluate any other properties coinciding with the upper and lower boundaries. Thus, all fields, except v and v^* that are computed in a domain $[N_x \times N_y - 1]$, are evaluated in a domain $[N_x \times N_y]$, with $i = 1, 2, 3, ..., N_x$ and $j = 1, 2, 3, ..., N_y$.

By Eqs. (3.73) and (3.78), it can be seen that for any cell of the boundaries ($i = 1$ or $i = N_x$ or $j = 1$ or $j = N_y$), at least one neighboring cell will be outside the domain $[N_x \times N_y]$. Therefore, at borders it is necessary to use ghost nodes, i.e. nodes out of the domain, as the red dots in Figure 9. The ghost nodes are commonly used for the application of boundary conditions as will be further explained.

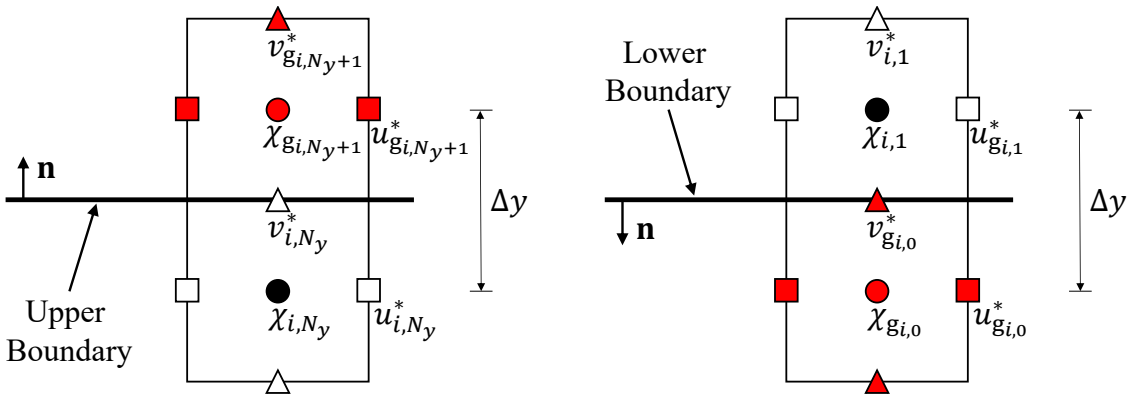

Figure 9 – Upper and lower boundaries. The red dots correspond to points outside the solution domain, but which are used to solve the governing equations.

For χ and pressure field the boundary conditions on the upper and lower walls are, respectively, $\nabla\chi \cdot \mathbf{n} = 0$ and $\nabla p \cdot \mathbf{n} = 0$, that is, in a domain $[N_x \times N_y]$ according to the Figure 9,

$$\begin{cases} \chi_{1:N_x,0} = \chi_{1:N_x,1} & \text{, lower;} \\ p_{1:N_x,0} = p_{1:N_x,1} & \text{, lower;} \\ \chi_{1:N_x,N_y+1} = \chi_{1:N_x,N_y} & \text{, upper;} \\ p_{1:N_x,N_y+1} = p_{1:N_x,N_y} & \text{, upper.} \end{cases} \tag{3.85}$$

For the velocity field component u, the ghost nodes in the upper and lower contours are determined based on the upper and lower wall velocities. From Figure 9, note that the top wall is between nodes $[1 : N_x, N_y]$ and $[1 : N_x, N_y + 1]$ at a distance $\Delta y/2$ of both, the same happens in the lower wall, between the nodes $[1 : N_x, 0]$ and $[1 : N_x, 1]$. Therefore, on the upper and lower walls, respectively, the following condition is used:

$$U_s = \frac{u_{1:N_x,0} + u_{1:N_x,1}}{2} \tag{3.86}$$

and

$$U_n = \frac{u_{1:N_x,N_y} + u_{1:N_x,N_y+1}}{2}. \tag{3.87}$$

Thus, the ghosts nodes for u and v are:

$$\begin{cases} [l]u_{1:N_x,N_y+1} = 2U_n - u_{1:N_x,N_y} & \text{, upper;} \\ u_{1:N_x,0} = 2U_s - u_{1:N_x,1} & \text{, lower;} \\ v_{1:N_x,N_y+1} = v_{1:N_x,N_y} = 0 & \text{, upper;} \\ v_{1:N_x,0} = 0 & \text{, lower.} \end{cases} \tag{3.88}$$

For the intermediate velocity field $\mathbf{u}^*$, it is necessary to relate the conditions of $\mathbf{u}$ and $\mathbf{u}^*$ by Eq. (3.51), so that, on the normal direction the walls,

$$\mathbf{u}^{n+1} \cdot \mathbf{n} = \mathbf{u}^* \cdot \mathbf{n} - \Delta t(\nabla\chi \cdot \mathbf{n})^{n+1} \tag{3.89}$$

being $\nabla\chi \cdot \mathbf{n} = 0$, $\mathbf{u}^{n+1} \cdot \mathbf{n} = \mathbf{u}^* \cdot \mathbf{n}$, that is, the boundary conditions known for $\mathbf{u}$ can be directly applied to $\mathbf{u}^*$ when the velocity component is normal to the wall. In the tangential direction to the wall,

$$\mathbf{u}^{n+1} \cdot \mathbf{t} = \mathbf{u}^* \cdot \mathbf{t} - \Delta t(\nabla\chi \cdot \mathbf{t})^{n+1}. \tag{3.90}$$

Thus, based on Eqs. (3.86) and (3.87), the ghost nodes of $\mathbf{u}^*$ when the velocity component is tangential to the wall are:

$$\begin{cases} u^*_{1:N_x,N_y+1} = 2U^*_n - u^*_{1:N_x,N_y} & \text{, upper;} \\ u^*_{1:N_x,0} = 2U^*_s - u^*_{1:N_x,1} & \text{, lower;} \end{cases} \tag{3.91}$$

where,

$$U^* = U + \Delta t \left(\frac{\chi^{n+1}_{i+1,j} - \chi^{n+1}_{i,j}}{\Delta x} \right) \tag{3.92}$$

and

$$\chi^{n+1}_{i,j} = 2\chi^n_{i,j} - \chi^{n-1}_{i,j}. \tag{3.93}$$

The boundary conditions applied on the upper and lower walls change the coefficients of the governing equations of fluid motion, Eqs. (3.73) and (3.78), so that on the upper wall $[1 : N_x, N_y]$,

$$\begin{cases} c_{ui,j} = c_{ui,j} - e_{ui,j}, \\ u^*_{i,j+1} = 2U^*_n, \\ c_{\chi i,j} = c_{\chi i,j} + e_{\chi i,j}, \\ e_{\chi i,j} = 0. \end{cases} \tag{3.94}$$

and on the lower wall $[1 : N_x, 1]$,

$$\begin{cases} c_{ui,j} = c_{ui,j} - b_{ui,j}, \\ u^*_{i,j-1} = 2U^*_s, \\ c_{\chi i,j} = c_{\chi i,j} + b_{\chi i,j}, \\ b_{\chi i,j} = 0. \end{cases} \tag{3.95}$$

On the domain sides, the boundary conditions are periodic, this means that, for a given boundary, all flow properties must be identical to the properties on the opposite boundary, including their respective derivatives. For the case of discretization presented here, this is done by assigning values to the ghosts equal to the values of the internal nodes adjacent to the opposite border, as shown in Figure 10.

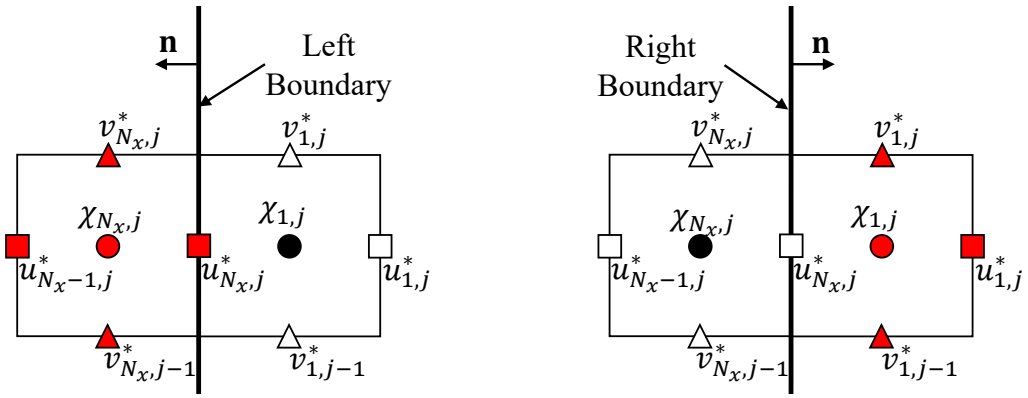

Figure 10 – Left and right boundaries. The red dots correspond to points outside the domain, but which are used to solve the governing equations. As in these boundaries, the boundary conditions are periodic, and the dots that are inside and outside the domain are inverted from one side to another.

Therefore, the ghost nodes for the domain sides are:

$$\begin{cases} u^*_{0,1:N_y} = u^*_{N_x,1:N_y} & \text{, left;} \\ u^*_{N_x+1,1:N_y} = u^*_{1,1:N_y} & \text{, right;} \\ v^*_{0,1:N_y} = v^*_{N_x,1:N_y} & \text{, left;} \\ v^*_{N_x+1,1:N_y} = v^*_{1,1:N_y} & \text{, right;} \\ \chi_{0,1:N_y} = \chi_{N_x,1:N_y} & \text{, left;} \\ \chi_{N_x+1,1:N_y} = \chi_{1,1:N_y} & \text{, right.} \end{cases} \tag{3.96}$$

All conditions described in Eq. (3.96) for u^*, v^* and χ are also valid, respectively, for u, v and p.

3.8 Surfactant concentration

The surfactant concentration, Eq. (3.40) is evolved by a semi-implicit Crank–Nicholson scheme, similar to that developed by Xu and Zhao (2003), as follows:

$$\begin{aligned} \frac{c^{n+1}-c^n}{\Delta t} = &\frac{3}{2}\left[-\nabla_s\cdot(c\mathbf{u}_s) - c(\nabla_s\cdot\mathbf{n})(\mathbf{u}\cdot\mathbf{n})\right]^n \\ &-\frac{1}{2}\left[-\nabla_s\cdot(c\mathbf{u}_s) - c(\nabla_s\cdot\mathbf{n})(\mathbf{u}\cdot\mathbf{n})\right]^{n-1} \\ &+\frac{1}{2Pe}\left(\nabla_s^2 c^{n+1} + \nabla_s^2 c^n\right), \end{aligned} \tag{3.97}$$

the difference is that here, the Eq. (3.97) is changed by the closest point method as presented by Ruuth and Merriman (2008), thus

$$\nabla_s\cdot(c\mathbf{u}_s) = \nabla\cdot\left[c\left(\mathbf{cp}_{i,j}\right)\mathbf{u}_s\left(\mathbf{cp}_{i,j}\right)\right], \tag{3.98}$$

$$c(\nabla_s\cdot\mathbf{n})(\mathbf{u}\cdot\mathbf{n}) = c\left(\mathbf{cp}_{i,j}\right)\left[\nabla\cdot\mathbf{n}\left(\mathbf{cp}_{i,j}\right)\right]\left[\mathbf{u}\left(\mathbf{cp}_{i,j}\right)\cdot\mathbf{n}\left(\mathbf{cp}_{i,j}\right)\right] \tag{3.99}$$

and

$$\nabla_s^2 c = \nabla^2 c\left(\mathbf{cp}_{i,j}\right). \tag{3.100}$$

Discretizing the Eq. (3.97) by finite differences and using the closest point method,

$$\begin{aligned} a_{ci,j}c\left(\mathbf{cp}^{n+1}_{i-1,j}\right) + b_{ci,j}c\left(\mathbf{cp}^{n+1}_{i,j-1}\right) + c_{ci,j}c\left(\mathbf{cp}^{n+1}_{i,j}\right) \\ +d_{ci,j}c^{n+1}\left(\mathbf{cp}_{i+1,j}\right) + d_{ci,j}c\left(\mathbf{cp}^{n+1}_{i,j+1}\right) = f_{ci,j} \end{aligned} \tag{3.101}$$

where the coefficients $a_{ci,j}$, $b_{ci,j}$, $c_{ci,j}$ and $d_{ci,j}$ are, respectively,

$$a_{ci,j} = d_{ci,j} = -\frac{\Delta t}{2Pe\Delta x^2}, \tag{3.102}$$

$$b_{ci,j} = e_{ci,j} = -\frac{\Delta t}{2Pe\Delta y^2}, \tag{3.103}$$

$$d_{ci,j} = 1 + \frac{\Delta t}{Pe\Delta x^2} + \frac{\Delta t}{Pe\Delta y^2} \tag{3.104}$$

and

$$\begin{aligned} f_{ci,j} = \frac{3\Delta t}{2}\left\{-\nabla\cdot\left[c\left(\mathbf{cp}_{i,j}^{n}\right)\mathbf{u}_s^{n}\left(\mathbf{cp}_{i,j}^{n}\right)\right]\right. \\ \left.-c\left(\mathbf{cp}_{i,j}^{n}\right)\left[\nabla\cdot\mathbf{n}\left(\mathbf{cp}_{i,j}^{n}\right)\right]\left[\mathbf{u}\left(\mathbf{cp}_{i,j}^{n}\right)\cdot\mathbf{n}\left(\mathbf{cp}_{i,j}^{n}\right)\right]\right\} \\ -\frac{\Delta t}{2}\left\{-\nabla\cdot\left[c\left(\mathbf{cp}_{i,j}^{n-1}\right)\mathbf{u}_s\left(\mathbf{cp}_{i,j}^{n-1}\right)\right]\right. \\ \left.-c\left(\mathbf{cp}_{i,j}^{n-1}\right)\left[\nabla\cdot\mathbf{n}\left(\mathbf{cp}_{i,j}^{n-1}\right)\right]\left[\mathbf{u}\left(\mathbf{cp}_{i,j}^{n-1}\right)\cdot\mathbf{n}\left(\mathbf{cp}_{i,j}^{n-1}\right)\right]\right\}^{n-1} \\ +\frac{\Delta t}{2Pe}\nabla^2 c\left(\mathbf{cp}_{i,j}^{n}\right) + c_{i,j}^{n}. \end{aligned} \tag{3.105}$$

in which, regardless of the time step,

$$\begin{aligned} -\nabla\cdot\left[c\left(\mathbf{cp}_{i,j}\right)\mathbf{u}_s\left(\mathbf{cp}_{i,j}\right)\right] = \\ -\frac{\left(c\left(\mathbf{cp}_{i+1,j}\right)u_s\left(\mathbf{cp}_{i+1,j}\right)\right) - \left(c\left(\mathbf{cp}_{i-1,j}\right)u_s\left(\mathbf{cp}_{i-1,j}\right)\right)}{2\Delta x} \\ -\frac{\left(c\left(\mathbf{cp}_{i,j+1}\right)v_s\left(\mathbf{cp}_{i,j+1}\right)\right) - \left(c\left(\mathbf{cp}_{i,j-1}\right)v_s\left(\mathbf{cp}_{i,j-1}\right)\right)}{2\Delta y}, \end{aligned} \tag{3.106}$$

$$\begin{aligned} -c\left(\mathbf{cp}_{i,j}\right)\left[\nabla\cdot\mathbf{n}\left(\mathbf{cp}_{i,j}\right)\right]\left[\mathbf{u}\left(\mathbf{cp}_{i,j}\right)\cdot\mathbf{n}\left(\mathbf{cp}_{i,j}\right)\right] = \\ -c\left(\mathbf{cp}_{i,j}\right)\kappa\left(\mathbf{cp}_{i,j}\right)\left[u\left(\mathbf{cp}_{i,j}\right)n_x\left(\mathbf{cp}_{i,j}\right) + v\left(\mathbf{cp}_{i,j}\right)n_y\left(\mathbf{cp}_{i,j}\right)\right], \end{aligned} \tag{3.107}$$

and

$$\begin{aligned} \nabla^2 c\left(\mathbf{cp}_{i,j}^{n}\right) = \left(\frac{c\left(\mathbf{cp}_{i-1,j}\right) + c\left(\mathbf{cp}_{i+1,j}\right) - 2c\left(\mathbf{cp}_{i,j}\right)}{\Delta x^2}\right) \\ + \left(\frac{c\left(\mathbf{cp}_{i,j-1}\right) + c\left(\mathbf{cp}_{i,j+1}\right) - 2c\left(\mathbf{cp}_{i,j}\right)}{\Delta y^2}\right). \end{aligned} \tag{3.108}$$

Eq. (3.101) is solved by the biconjugate gradient stabilized method, as shown in Annex B.

3.9 Numerical methodology to compute the droplet shape

The droplet deformation is measured by Taylor deformation parameter (TAYLOR, 1934), as follows:

$$D_T = \frac{L - B}{L + B}, \tag{3.109}$$

where L is the droplet length (largest dimension) and B is the height (smallest dimension). Note that Taylor deformation is zero for the case where $L = B$ (spherical drop) and converges to 1 when $L \gg B$.

In order to determine the droplet dimensions and inclination, a methodology is developed to compute the surface points $\mathbf{x}_\Gamma$ sequentially in the counter-clockwise direction. From these points, it is possible to determine both the droplet size and the length of its surface. This methodology is illustrated in Figure 11, consisting of firstly determining the droplet center $\mathbf{x}_c$ (black dot). Then the droplet contour is divided in n_θ points (yellow dots), so that the position vector of each point, $\mathbf{x}_\Gamma = (x_{\theta_i}, y_{\theta_i})$, which originates on the droplet center, forms an angle θ_i, $i = 1, ..., n_\theta$ with the vector $\mathbf{x}_{\Gamma_{n_\theta}} = (0, L_x)$. These points have the same angular spacing from each other, that is $\theta_{i+1} = \theta_i + \Delta\theta$ where $\Delta\theta = 2\pi/n_\theta$.

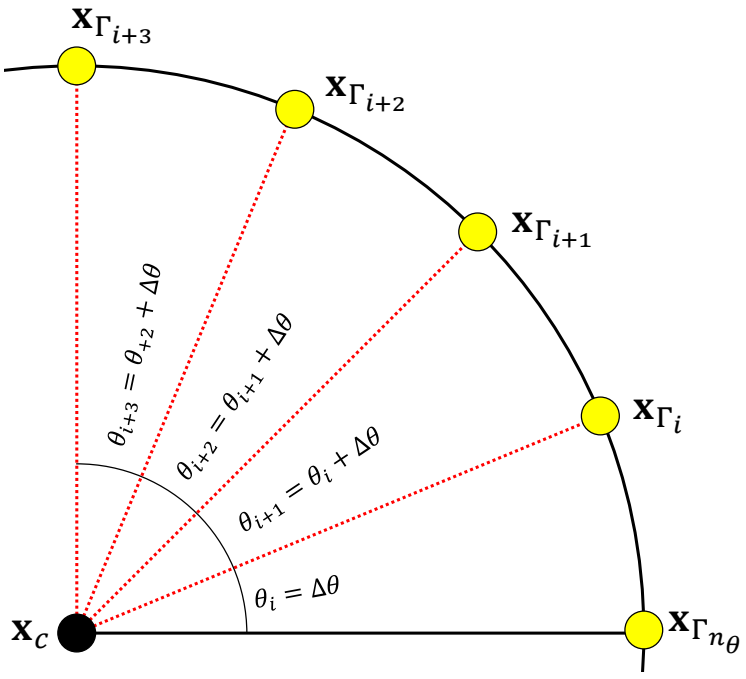

Figure 11 – Geometrical representation of the droplet measure. Each yellow dot on the surface corresponds to an angle θ_i.

For each value of θ_i, $\mathbf{x}_{\Gamma_i}$ is determined by following system,

$$\begin{cases} \phi(\mathbf{x}_{\Gamma_i}) = 0 \\ (\mathbf{x}_{\Gamma_i} - \mathbf{x}_c) \times \mathbf{x}_{\theta_i} = 0, \end{cases} \tag{3.110}$$

which is solved by Newton-Raphson method considering,

$$\begin{cases} f_1 = \phi(x_{\Gamma_i}, y_{\Gamma_i}) = 0 \\ f_2 = x_{\Gamma_i} y_{\theta_i} - y_{\Gamma_i} x_{\theta_i} - x_c y_{\theta_i} + y_c x_{\theta_i} \end{cases}, \tag{3.111}$$

where $x_{\theta_i} = \cos\theta_i$ and $y_{\theta_i} = \sin\theta_i$.

Therefore, the discrete points of the droplet surface for each θ_i are obtained by the following steps:

1. $\text{tol} = 10^{-10}$, $i = 0$, $\theta_0 = 0$;
2. $\theta_{i+1} = \theta_i + \Delta\theta$, $k = 0$, $x^k_{\Gamma_i} = x_{\Gamma_{i0}}$ and $y^k_{\Gamma_i} = y_{\Gamma_{i0}}$. where, k represents the iteration of the Newton-Raphson method, $x_{\Gamma_{i0}}$ and $y_{\Gamma_{i0}}$ are the interface coordinates corresponding to θ_i determined in the last droplet measurement. In the first iteration, $x_{\Gamma_{i0}}$ and $y_{\Gamma_{i0}}$ are estimated considering a spherical droplet;
3. Rewrite the system of equations using the Newton-Raphson method so that:

$$\begin{pmatrix} \frac{\partial f_1}{\partial x} & \frac{\partial f_1}{\partial y} \\ \frac{\partial f_2}{\partial x} & \frac{\partial f_2}{\partial y} \end{pmatrix} \begin{pmatrix} \delta x_{\Gamma_i} \\ \delta y_{\Gamma_i} \end{pmatrix} = \begin{pmatrix} -f_1 \\ -f_2 \end{pmatrix}, \tag{3.112}$$

   or

$$\begin{pmatrix} \frac{\partial \phi}{\partial x}\left(x^k_{\Gamma_i}, y^k_{\Gamma_i}\right) & \frac{\partial \phi}{\partial y}\left(x^k_{\Gamma_i}, y^k_{\Gamma_i}\right) \\ y_{\theta_i} & -x_{\theta_i} \end{pmatrix} \begin{pmatrix} \delta x^k_{\Gamma_i} \\ \delta y^k_{\Gamma_i} \end{pmatrix} = \begin{pmatrix} -f^k_1 \\ -f^k_2 \end{pmatrix}, \tag{3.113}$$

   where $\delta x^k_{\Gamma_i}$ and $\delta y^k_{\Gamma_i}$ are, respectively, the corrections of $x^k_{\Gamma_i}$ and $y^k_{\Gamma_i}$;
4. Solve the system in Eq. (3.113) by Cramer's rule to obtain: $\delta x^k_{\Gamma_i}$ and $\delta y^k_{\Gamma_i}$;
5. Correct $x^k_{\Gamma_i}$ and $y^k_{\Gamma_i}$ by:

$$\begin{cases} x^{k+1}_{\Gamma_i} = x^k_{\Gamma_i} + \delta x^k_{\Gamma_i}, \\ y^{k+1}_{\Gamma_i} = y^k_{\Gamma_i} + \delta y^k_{\Gamma_i}; \end{cases} \tag{3.114}$$

6. If $|f^{k+1}_1| + |f^{k+1}_2| < \text{tol}$, go to step 7, else $k = k + 1$ and return to step 3;
7. If $i = n_\theta$, go to step 8, else $i = i + 1$ and return to step 2;
8. Finish.

Thus, the arc-length (the contour length) is computed by the sum of the distance between the points $\mathbf{x}_{\Gamma_i}$ obtained by Eq. (3.110), the largest and smallest droplet dimensions are, respectively, the largest and the smallest distance between $\mathbf{x}_{\Gamma_i}$ and the center of the droplet, $\mathbf{x}_c$.

4 Results and discussions

This chapter is divided into two main parts. The first part deals only with the effects of the surfactant, while the second deals with the combined effect of this surface active agent and the action of an external magnetic field. The results are presented both in terms of the individual properties of each droplet and the emulsion rheology, being explored in terms of the droplet deformation and inclination, surfactant concentration and forces on the interface, contributions of capillary and Marangoni stresses, and magnetic field to the droplet shape, emulsion reduced viscosity, the first normal stress difference and the bulk emulsion magnetization (only for ferrofluid droplets emulsions). For this purpose, we fixed the Reynolds and capillary numbers to $Re = 10^{-2}$ and $Ca = 0.1$ (except for some special cases for comparison with literature results) and used a range of Péclet numbers that contemplates the dominance of the surfactant advection ($Pe = 10^{3}$), diffusion ($Pe = 10^{-3}$) and the equivalence of both ($Pe = 1$). The low Reynolds number mitigates the inertial effects so that the emulsion can be considered a rheological material.

In all simulations, the dispersed and continuous phases are assumed to have the same viscosity, $\lambda = 1$. In addition, we set $h = \Delta x = \Delta y$. Due to the diversity of tests performed and the reproduction of some results present in the literature, the individual characteristics of each simulation, such as domain, mesh, time step, surfactant coverage and elasticity, and magnetic field intensity, are presented in each section.

4.1 Non-magnetic surfactant-covered droplets

In this section, we perform a rate of convergence test of the numerical model and verification by comparison with the numerical results of Li and Pozrikidis (1997) for a surfactant-covered droplet, as well. In addition, we investigate the surfactant concentration, surface tension coefficient, and signed magnitude of capillary and Marangoni forces over the droplet surface. Our results are compared to those of Xu, Yang and Lowengrub (2012). These studies are performed to verify the accuracy of the proposed model. Then, results on the effects of elasticity and surfactant coverage on the emulsion rheology are presented. It is well-known that the macroscopic rheological properties of emulsions are closely related to the flow at the droplet scale. Here, we present cases in which the rheological properties are more affected by the presence of the surfactant than by the droplet shape.

Table 1 – Errors and convergence rate for the surfactant concentration at $t = 0.5$ for $X = 0.6$, $E = 0.2$, $\lambda = 1$, $Ca = 0.1$, $Pe = 10$ and $Re = 10$.

h	c_h	$c_h - c_{h/2}$	r
0.08	0.9194190291	0.0027084028	0.6850475492
0.04	0.9221274319	0.0016845868	0.9221863430
0.02	0.9238120187	0.0008889711	0.9741642078
0.01	0.9247009898	0.0004525171	1.0003880508
0.005	0.9251535069	0.0002261977	-
0.0025	0.9253797046	-	-

4.1.1 Convergence rate and droplet shape comparison with results from the literature

In Table 1 results of the convergence rate study for the surfactant concentration are presented. We consider a simulation until the instant $t = 0.5$ in a $[10 \times 4]$ non-dimensional domain, discretized by a regular 500×200 cells mesh, for $X = 0.6$, $E = 0.2$, $\lambda = 1$, $Ca = 0.1$, $Pe = 10$ and $Re = 10$. The concentration was computed in the droplet surface at $x = 6$ and $y = 2$ using a third-order Lagrange interpolation. The convergence rate, r was calculated using Richardson extrapolation by $r = \log_2\left(\frac{c_h - c_{h/2}}{c_{h/2} - c_{h/4}}\right) + \mathcal{O}(h)$, resulting in first order convergence rate for concentration. This result is compatible with the work of Xu, Yang and Lowengrub (2012), which has used an Adams-Bashford formula combined with normally extended values of concentration, around the interface. The same convergence rate is commonly obtained in conventional continuum surface force methods like Immersed Boundary (see e.g. Li and Ito (2006)).

In Figure 12 we present the deformation and inclination (inset) of a surfactant-laden three-dimensional droplet subjected to a simple shear flow as a function of Ca (red curves). We considered a square domain, $[8 \times 8]$, discretized by a regular 400×400 cells mesh and minimized the inertia effects by setting $Re = 10^{-2}$. We compared our results for droplet deformation and inclination with data from the work of Li and Pozrikidis (1997) (black line) for $\lambda = 1$, $Pe = 10^3$, $X = 0.6$, and $E = 0.1$, obtained using 3D Boundary Integral Simulations. We found a good agreement for D_T, at $Ca < 0.15$, and for inclination at the entire range. At larger Ca, results begin to diverge due to the increasing importance of 3D deformation mechanisms, which become more important at higher deformations (SOLIGO; ROCCON; SOLDATI, 2019b).

4.1.2 Surfactant concentration and forces on the interface

Figures 13 and 14 present interface quantities as functions of the arc-length at the steady state in a $[10 \times 4]$ non-dimensional domain, discretized by a regular 500×200 cell mesh. For these simulations, we have considered $Re = 10$, $Ca = 0.1$, $X = 0.6$, $E = 0.2$,

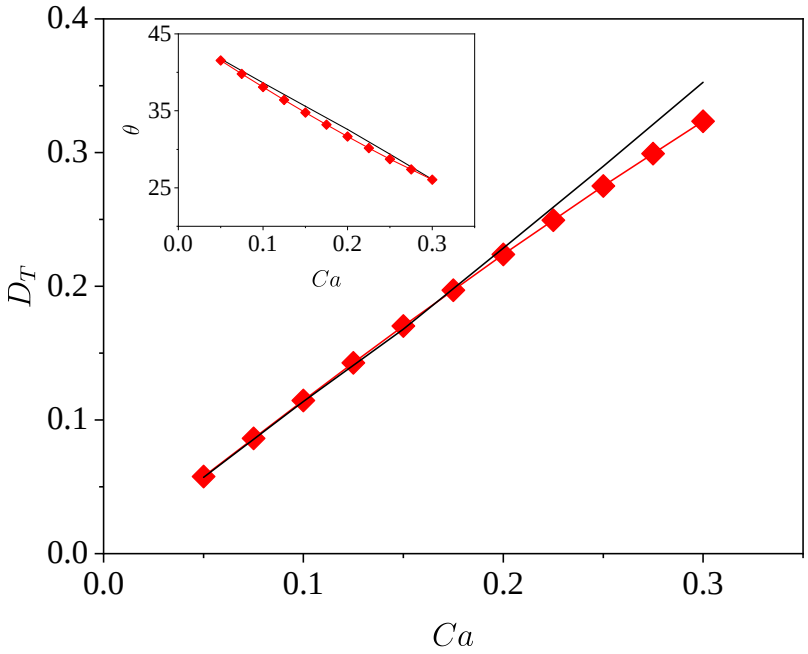

Figure 12 – Taylor deformation, D_T, as function of Ca for $X = 0.6$, $E = 0.1$ and $\alpha = Pe/Ca = 10$. Red curve and black line corresponds, respectively, to the present model and the work of Li and Pozrikidis (1997). The inset shows the dependence of the droplet inclination, θ, as functions of Ca.

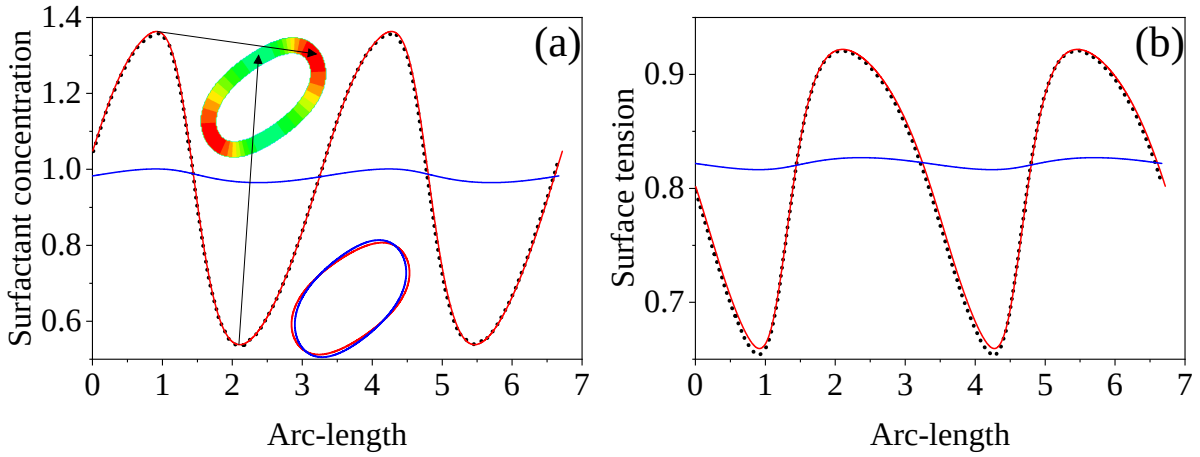

Figure 13 – (a) Surfactant concentration and (b) surface tension coefficient over droplet surface for $Re = 10$, $Ca = 0.1$, $X = 0.6$, $E = 0.2$, $Pe = 10$ (red line), and $Pe = 1$ (blue line). The black dotted line corresponds to the work of Xu, Yang and Lowengrub (2012). The insets of (a) shows droplet contours colored by surfactant concentration for $Pe = 10$ and the droplet shapes for $Pe = 1$ and $Pe = 10$.

$Pe = 10$ (red line) and $Pe = 1$ (blue line). The arc-length coordinate starts at the point on the surface that crosses the x-axis and increases in the counterclockwise direction. The black dotted line corresponds to data from the work of Xu, Yang and Lowengrub (2012), which are in close agreement with ours, suggesting good accuracy of both methodologies.

Figures 13(a) and (b) present the surfactant concentration and the surface tension coefficient as functions of the arc-length. In Figure 13(a) it is clear that the surfactant

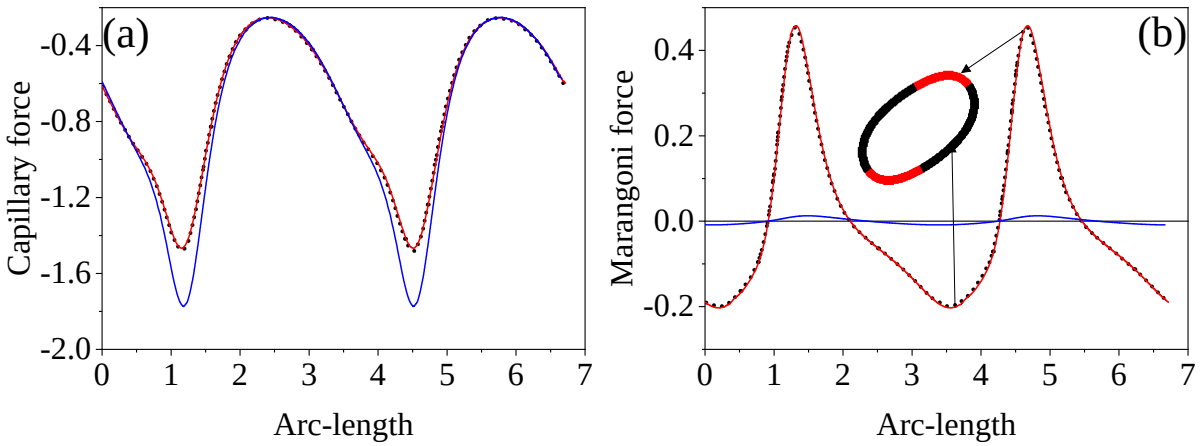

Figure 14 – Concentrated body forces for $Re = 10$, $Ca = 0.1$, $X = 0.6$, $E = 0.2$, $Pe = 10$ (red line), and $Pe = 1$ (blue line). (a) Signaled capillary force magnitude ($\mathbf{F}_c \cdot \hat{\mathbf{n}}$) and (b) signaled Marangoni force magnitude ($\mathbf{F}_m \cdot \hat{\mathbf{t}}$). The black dotted line corresponds to the work of Xu, Yang and Lowengrub (2012). The inset of (b) shows where $\mathbf{F}_m \cdot \hat{\mathbf{t}}$ is positive (red contour) or negative (black contour).

concentration increases at the droplet tips and decreases at the more elongated surface. This is due to the flow action, which sweeps the surfactant to the droplet tips. In addition, we show the contour of the droplet for $Pe = 1$ and $Pe = 10$. The shapes are remarkably similar, indicating that Péclet variations alone do not significantly affect the droplet geometry; even drastic variations of surfactant concentration and surface tension coefficient are visibly more pronounced for $Pe = 10$. In fact, for $Pe = 1$, diffusion almost uniformly distributes the surfactant over the droplet surface, leading to a maximal variation of σ of 0.76%, around the mean value. In these situations, Marangoni forces are very small, and the interface behaves as in a clean droplet, with mean surface tension uniformly reduced by the covering substance.

The curves in Figure 14(a) show the signaled magnitude of the capillary force, defined as $\mathbf{F}_c \cdot \hat{\mathbf{n}}$, as a function of the arc-length. Negative values of this quantity can be considered as forces compressing the fluid inside the droplet. The maximum absolute value of $\mathbf{F}_c \cdot \hat{\mathbf{n}}$ are considerably higher for $Pe = 1$ when compared to $Pe = 10$. For $Pe = 1$, diffusion is able to remove the surfactant from the tips, such that surface tension, and consequently the capillary forces, became higher in these regions.

Figure 14(b) shows the signaled magnitude of the Marangoni force, defined as $\mathbf{F}_m \cdot \hat{\mathbf{t}}$, as a function of the arc-length. In contrast to the capillary forces, the signal of the Marangoni forces varies along the interface. The inset in Figure 14(b) show where the signal of $\mathbf{F}_m \cdot \hat{\mathbf{t}}$ is positive (red lines) or negative (black lines). At the locations where $\mathbf{F}_m \cdot \hat{\mathbf{t}} > 0$, the Marangoni force is in the opposite direction of the vorticity, meaning that in these regions $\mathbf{F}_m$ resists the flow. On the other hand, if $\mathbf{F}_m \cdot \hat{\mathbf{t}} < 0$, then $\mathbf{F}_m$ favors the flow field, contributing to drive the rotation of the droplet in the same direction of the vorticity.

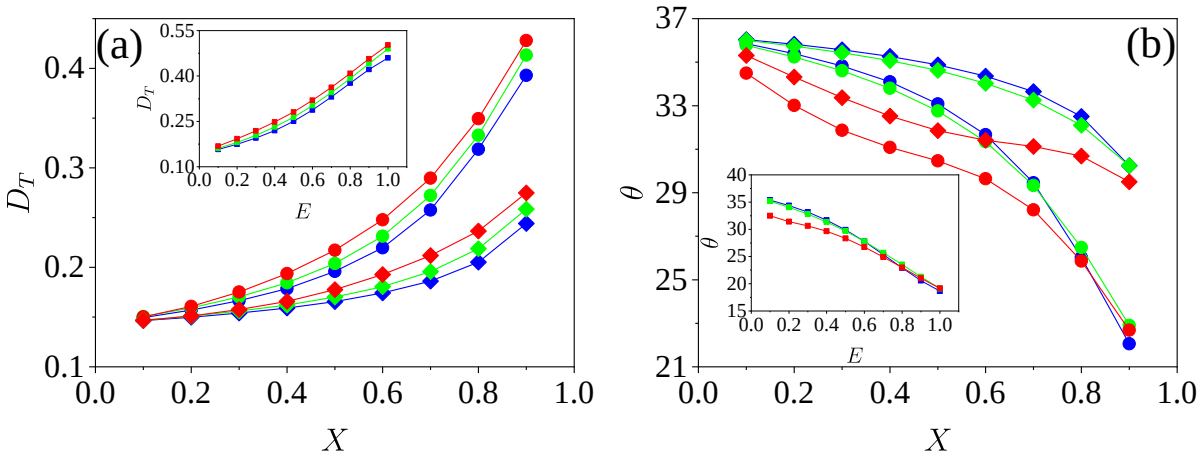

Figure 15 – (a) Taylor deformation parameter and (b) droplet inclination as functions of X for $E = 0.2$ (diamonds) and $E = 0.4$ (circles). $Pe = 10^3$ (red), $Pe = 1$ (green), and $Pe = 10^{-3}$ (blue). The insets show the variation of D_T and θ as functions of E for $X = 0.6$.

4.1.3 Influence of the surfactant's elasticity and coverage factor in the droplet shape

The droplet shape is influenced by the parameters related to the surfactant and its distribution over the droplet surface. In this section, we use the same domain and mesh considered in the preceding section to study the influence of the elasticity and coverage parameters on the droplet deformation (D_T), and inclination angle (θ), defined between the principal deformation axis of the droplet and the vertical. We considered $Ca = 0.1$ and $\lambda = 1$, allowing moderate deformation, but avoiding droplet breakup. We set $Re = 10^{-2}$ to minimize inertia effects on the flow at the droplet scale.

Figure 15(a) and (b) present the Taylor deformation parameter and droplet inclination angle, as functions of the coverage parameter, respectively. We present results for $Pe = 10^3$ (red), $Pe = 1$ (green), and $Pe = 10^{-3}$ (blue). The diamonds represent $E = 0.2$, and the circles, $E = 0.4$.

Regarding Figs.15(a) and (b), the results show that, as coverage increases, D_T increases and θ decreases, regardless of the Pe or E. Such behavior is a direct consequence of the overall diminishing of the surface tension as the amount of surfactant on the interface increases. As the surface became less stiff, the shear flow causes higher deformations, and bent the droplet in the direction of the main flow (decreasing the θ). The deformation varied more significantly as a function of the elasticity than the Péclet number. The inset of Figure 15(a) shows the curves of D_T as a function of E, for $X = 0.6$ and the same Péclet numbers. The curves are very similar, with a small vertical displacement.

The droplet deformation depends strongly on X and E, and the influence of Pe is less significant. It turns out that the elasticity and coverage factors directly impact the value of the surface tension coefficient (X accounting for the amount of surfactant and E

for the sensibility of σ on the concentration) and, consequently, on the normal forces on the surface, which are capable of changing the droplet's shape. The Péclet number, in turn, alters the surfactant distribution, and its effect on the surface tension coefficient elapses from a more elaborate mechanism. In a diffusion dominating situation (low Pe), surfactant tends to uniformly distribute, reducing the surface tension on the entire interface. On the other hand, for advective dominating regimes (high Pe), the surfactant concentrates on the high curvature regions, leaving the less curved sections partially uncovered. Our results indicate that concentrating the surfactant in the high curvature regions allows slightly more deformed droplets than in the situation where σ is reduced in the entire interface.

In general, the droplet inclination angle θ is a monotonic decreasing function of X, as can be seen in Fig.15(b). For a fixed E, the green and blue curves are very close in the entire range of X, indicating that for $Pe \leq 1$, θ is only a weak function of Pe and much more sensitive to variations of X. The inset in Fig.15(b) show the dependence of θ on E for $X = 0.6$. One can note that the inclination angle does not depend on Pe for very elastic surfactants. The relationship between the inclination angle, θ, and the parameters Pe, E, and X is more intricate than what is observed in the case of Taylor deformation. In a situation where the surfactant is uniformly distributed over the surface, it is expected that a higher elasticity causes the deformed droplet to bend towards the main flow direction (smaller θ), as a consequence of the more intense reduction of the surface tension. This is actually observed for high coverage factors ($X \geq 0.6$, approximately), regardless of the Pe. However, for $X < 0.6$, the balance between diffusion and advection might change this relation, and surfactants with $E = 0.4$ (more elastic) for $Pe = 1$ and $Pe = 10^{-3}$ (a lot of diffusion) are less aligned to the flow (higher θ) than surfactants with $E = 0.2$ (less elastic) for $Pe = 10^3$ (advection-dominated).

As a general rule, the addition of surfactant in the droplet surface, which causes a reduction of the surface tension coefficient, implies in higher deformation and droplet alignment with the flow. The same is observed in clean droplets, for increasingly higher capillary numbers. This is not surprising since the droplet shape should be directly related to forces and displacements in the normal direction of the interface, and lowering σ, thus reducing the normal stress jump. The tangential forces, which arise from non-uniform surfactant distribution over the surface, cannot move material fluid particles out of the current interface region. In this manner, Marangoni stresses affect the droplet shape only indirectly. The rheology, however, depends on the stresses on the surface, which are strongly affected by the surfactant's dynamics. In the next section, we present results which show that, in the presence of surfactants, emulsion rheology cannot be directly associated to the droplet shape, as is the case in clean droplet emulsions.

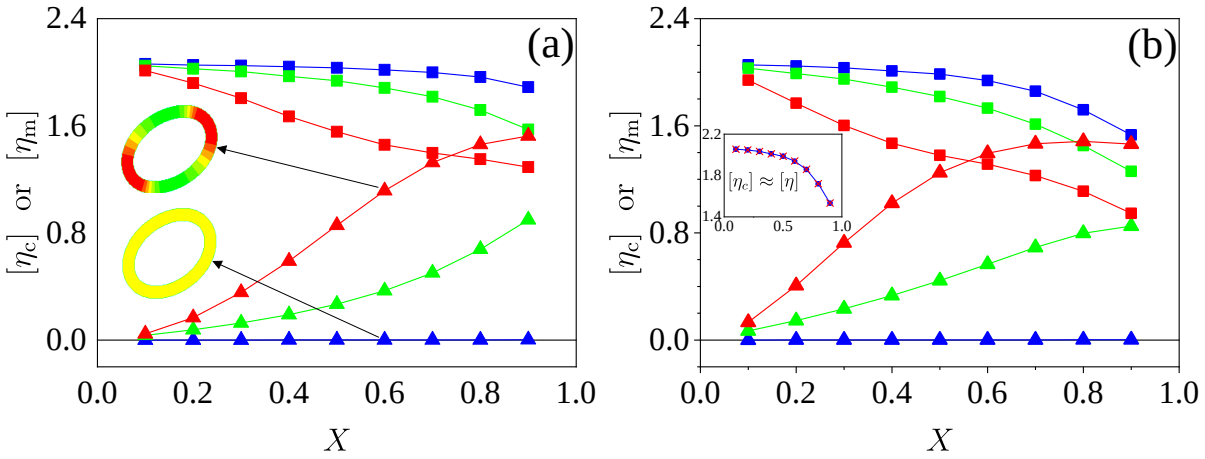

Figure 16 – Capillary viscosity (squares) and Marangoni viscosity (triangles) for (a) $E = 0.2$ and (b) $E = 0.4$. $Pe = 10^3$ (red), $Pe = 1$ (green), and $Pe = 10^{-3}$ (blue). The inset of (a) show the droplet contours colored by surfactant concentration for the same E and X. The inset of (b) show the parallel between the capillary viscosity and the reduced viscosity for $Pe = 10^{-3}$.

4.1.4 Effects of the surfactant coverage, elasticity, and Péclet number on the emulsion's rheology

In Figure 16 we present the capillary viscosity Eq. (2.35) and Marangoni viscosity (Eq. 2.37) as functions of the coverage factor, for (a) $E = 0.2$ and (b) $E = 0.4$, and $Pe = 10^3$ (red), $Pe = 1$ (green), and $Pe = 10^{-3}$ (blue).

For $Pe = 1$, the Marangoni viscosity grows significantly as X increases, becoming comparable to the capillary viscosity for $X > 0.8$. In the fully advective regime, at $Pe = 10^3$, $[\eta_m]$ becomes bigger than $[\eta_c]$ for a sufficient coverage. We observed that the value of X, from which the Marangoni viscosity becomes bigger than the capillary viscosity, becomes smaller for higher values of E. This can be observed when comparing the points where the red curves cross, between Fig.16(a) and (b). These effects are a consequence of the availability of insoluble surfactant on the droplet surface, under conditions where the surface flow maintains a convective transport rate dominant compared to diffusion. As the amount of surfactant on the surface increases, the reduction in the surface tension coefficient leads to a decrease in the capillary viscosity. However, if there is enough advection to induce strong concentration gradients, the increase in the Marangoni viscosity can compensate the reduction in the capillary viscosity.

Figure 17(a) and (b) shows the reduced viscosity as a function of the coverage parameter for $E = 0.2$ and $E = 0.4$, respectively. The inset show the droplet contours for the three Péclet numbers at the same X and E. It is clear that the droplet shapes are remarkably similar and the differences in the reduced viscosity are clearly not associated to the droplet elongation and inclination.

Since in this work we set $\lambda = 1$, the reduced viscosity $[\eta]$ is the sum of $[\eta_c]$ and $[\eta_m]$.

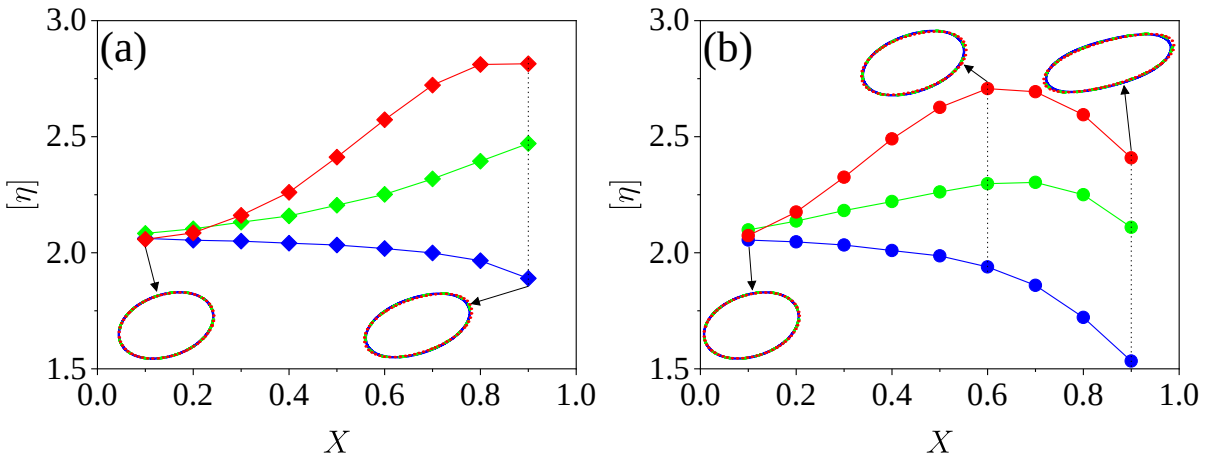

Figure 17 – Reduced viscosity as a function of X for (a) $E = 0.2$ and (b) $E = 0.4$. $Pe = 10^3$ (red), $Pe = 1$ (green), and $Pe = 10^{-3}$ (blue). The insets show droplets for all Péclet numbers.

In this way, the variations of the reduced viscosity as a function of Pe, X, and E can be analyzed in terms of the variations of $[\eta_c]$ and $[\eta_m]$ as a function of those parameters. For $\lambda \neq 1$, the influence of the surfactant parameters on the reduced viscosity will be similar (since we can expect $[\eta_c]$ and $[\eta_m]$ to behave in the same way), although the $[\eta]$ will be not given by the sum of the capillary and Marangoni viscosity.

Figure 17 shows that for $Pe = 10^{-3}$, the reduced viscosity is a decreasing function of X. It happens that the Marangoni viscosity is practically null and the capillary viscosity reduces as the amount of surfactant on the surface increases. Comparing the blue curves in Figure 17(a) and (b), we can see that, the more elastic the surfactant, the steeper the $[\eta]$ curve will be, which is not surprising since the reduction of the surface tension coefficient is more accentuated for higher E. On the other hand, for $Pe = 1$ and, more noticeably, for $Pe = 10^3$, $[\eta]$ increases as a function of X because the growth rate of $[\eta_m]$ relative to X ($\partial[\eta_m]/\partial X$) overcomes the decrease rate of $[\eta]_c$ relative to X ($\partial[\eta_c]/\partial X$). The critical points in the red curves in Figure 17(b) occur when $\|\partial[\eta_m]/\partial X\| = \|\partial[\eta_c]/\partial X\|$. The decreasing of $[\eta]$ in those curves might be caused by the relative reduction of the surfactant concentration gradients because the surface is near to the saturation, reducing $\partial[\eta_m]/\partial X$. In other words, the non-monotonic variation of the reduced viscosity arises from the antagonistic behavior of the capillary and the Marangoni viscosity in the function of the coverage and elasticity factors. The capillary viscosity is always a decreasing function of the coverage (X) and elasticity (E). On the other hand, the Marangoni viscosity is either constant, for the low Péclet regime, or a growing function of X and E, if Pe is high enough. In this sense, the Pe acts as an activation parameter of the Marangoni viscosity: for low Pe, the Marangoni viscosity is absent; for high Pe, the Marangoni viscosity shows a vigorous increase in function of X and E. As the reduced viscosity is the sum of the capillary and the Marangoni viscosities, the competition between these two parcels leads to a non-monotonic behavior of the bulk shear viscosity.

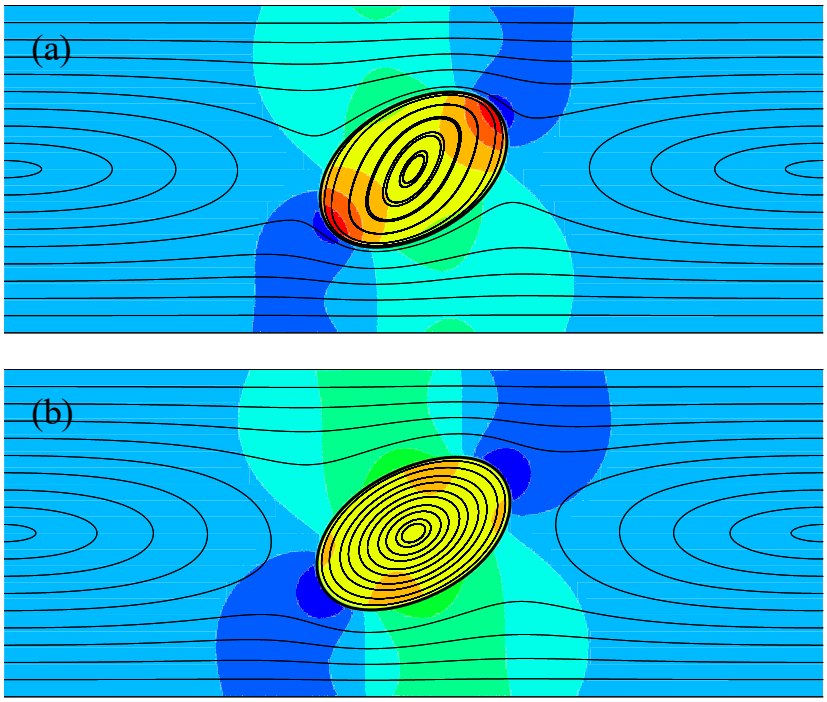

Figure 18 – Stream lines and pressure field for $X = 0.6$, $E = 0.4$, (a) $Pe = 10^{-3}$, and (b) $Pe = 10^{3}$.

Figure 18(a) and (b) shows the streamlines and pressure field for $X = 0.6$ in the conditions of the blue and red curves of Figure 17(b), respectively. The pressure levels are the same in the two figures. Although the droplet shape is virtually the same as can be seen in Figure 15, the different surfactant distributions over droplet surface affects the flow profile around and inside of the droplet. In Figure 10(a), as $Pe = 10^{-3}$, diffusion dominates, and surfactant is almost uniformly distributed. In this way, the interface behaves like a clean surface (with lower interfacial tension), such that the jump in the normal stress is more intense in the droplet's tips. At $Pe = 10^{3}$, advection moves the surfactant towards the droplet tips and reduces the normal stress jump in this location. As can be seen in the figures, the velocity and pressure fields are strongly influenced by the distinct surfactant action in diffusion or advection-dominated regimes.

Figure 19 shows the dependence of the reduced viscosity and it Marangoni and capillary parts on the elasticity for $Pe = 10^{3}$. Blue curves refers to $X = 0.3$ and red curves, to $X = 0.6$. The higher the surfactants sensibility, the lower the surface tension coefficient, in such a way that the deformation increases and the droplets align toward the flow direction for increasing E (as made clear in the insets of Fig.15). As the capillary viscosity relies heavily on deformation and inclination, it decreases monotonically with E, as can be seen in Figure 19(a) (curves with squares). The reduction is more accentuated for $X = 0.6$, due to the higher deformation and smaller inclination angle of the droplet.

On the other hand, the Marangoni viscosity does not behave monotonically in all situations. This effect might be a consequence of the larger interface area for higher E and X, as a consequence of higher deformation, which in turn tends to diminish the surface

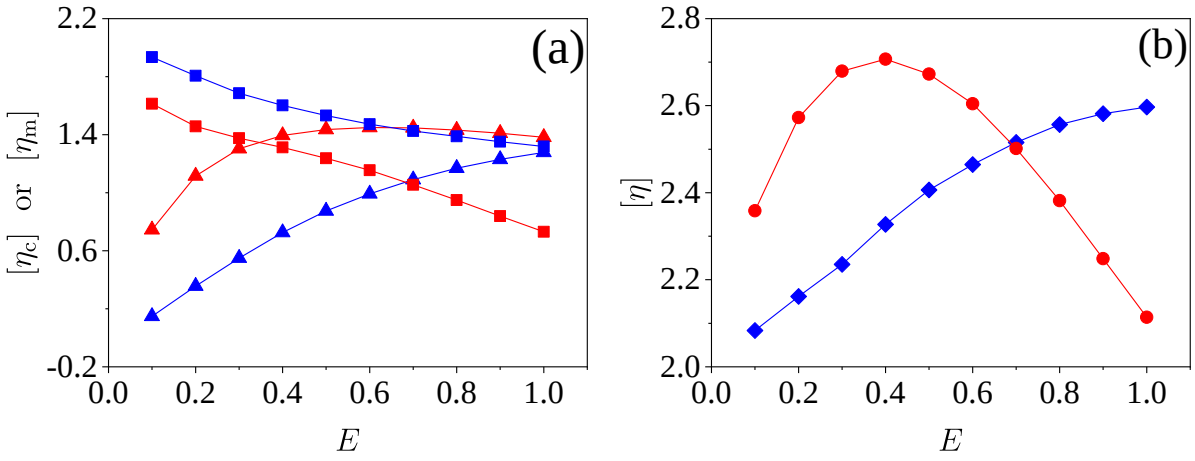

Figure 19 – (a) Capillary viscosity (squares) and Marangoni viscosity (triangles). (b) Reduced viscosity. $Pe = 10^3$, $X = 0.3$ (blue) and $X = 0.6$ (red).

gradients of σ, responsible for the Marangoni viscosity. In other words, the saturation (and even the slight reduction) of $[\eta_m]$ near to $E = 0.6$, observed for $X = 0.6$, might be a consequence of the surfactant's dilution in the deformed droplet. Therefore, the reduced viscosity for $X = 0.6$ (red curve in Figure 19(b)) assumes a maximum value with respect to E. After this critical point, the reduced viscosity of the emulsion decreases as a function of E. It is worth mentioning that variations of E can be induced by changing the emulsion temperature (see Eq.(2.28)).

4.1.5 Surfactant-covered droplets first normal stress difference

The first normal stress difference is a viscometric function strictly related to the elastic response of the fluid. It is defined as $N_1 = \sigma_{11} - \sigma_{22}$, where 1 stands for the fluid velocity direction and 2 for the direction of velocity variation. Considering the definitions in the present work, and that the contribution of the Newtonian part of the stress tensor to N_1 is exactly zero in shear flow, we compute the first normal stress difference using $N_1 = \sigma_{xx}^{(d)} - \sigma_{yy}^{(d)}$.

An emulsion can either exhibit positive or negative N_1 under simple shear, depending on different factors. The first theoretical prediction found positive N_1 for dilute emulsions under conditions of small deformation of droplets (SCHOWALTER; CHAFFEY; BRENNER, 1968). Various studies later confirmed this prediction for concentrated emulsions, highly deformed droplets, or high viscosity ratios (BRADY; BOSSIS, 1988; OLIVEIRA; CUNHA, 2015). For all those cases, the mechanism leading to the positiveness of N_1 arises from the deformation and relative inclination, towards the velocity direction, of the droplets in the emulsion. Inertia in the droplet scale might induce significant changes in the droplets' inclination angle, and induce negative N_1 in emulsions (SRIVASTAVA; MALIPEDDI; SARKAR, 2016). Clustering formation due to strong hydrodynamics forces also give rise to negative N_1 (FOSS; BRADY, 2000).

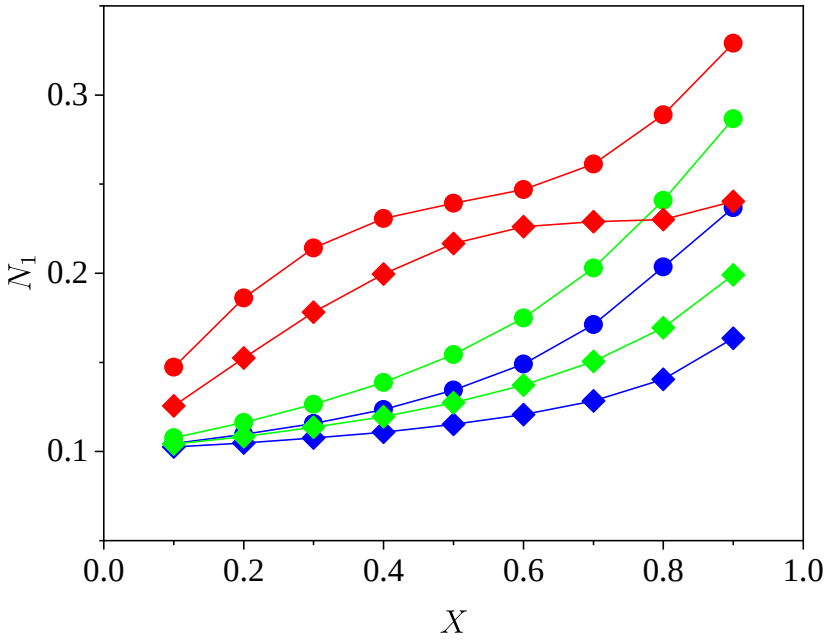

Figure 20 – First normal stress difference as a function of X, for $E = 0.2$ (diamonds) and $E = 0.4$ (circles). $Pe = 10^3$ (red), $Pe = 1$ (green), and $Pe = 10^{-3}$ (blue).

Figure 20 present N_1 as a function of X, for three Péclet numbers and two elasticity factors. Our results show that N_1 is positive for all cases we simulated. We found that N_1 increases with X. Figure 20 also shows that, for a given X, N_1 for $E = 0.4$ is greater than for N_1 for $E = 0.2$. As the droplet deformation and inclination increase with X and E, our results indicate that the N_1 behavior for dilute emulsion with insoluble surfactants is strongly depended on the droplet shape, as previously reported in the literature. In the conditions of the present work, the tangential stresses do not change the general macroscopic behavior of N_1 in a dilute emulsion as they do in the case of the reduced viscosity. In this sense, we believe that the presence of surfactants in dilute emulsions cannot change the signal of N_1.

We speculate that, for concentrated emulsion, the influence of the surfactants on the attractive/repulsive forces between the droplets can impact the cluster's formation. In such case, it is possible that the surfactant dynamics can have more pronounced influence on N_1, possibly changing its signal. This interesting question might be addressed in future works.

4.2 Surfactant-covered ferrofluid droplets under external magnetic field

In this section, we first reproduced some results of Cunha et al. (2020) for a single surfactant-free ferrofluid droplet subjected to an external magnetic field, placed at the center of a $[12 \times 12]$ non-dimensional domain, discretized by a regular 416×416 cell mesh.

This study was performed in order to verify the agreement with the physics of the magnetic problem. For this, we set $\varepsilon = 1.5h$, $Ca = 0.2$, $Re = 10^{-2}$, $\lambda = 1$, $\zeta = 2$ and a time step $\Delta t = 5 \times 10^{-4}$. Next, results on the effects of surfactant on ferrofluid droplets subjected to an external magnetic field are presented in terms of the droplet shape, emulsion rheology, and the mean magnetization of the system. Finally, we explore the rheology of this complex fluid in terms of the shear and rotational viscosities.

We considered $Ca = 0.1$ and $\lambda = 1$, allowing moderate deformation, but avoiding droplet breakup. We set $Re = 10^{-2}$ to minimize inertia effects on the flow at the droplet scale, and $\varepsilon = 2h$, $\zeta = 2$ and $\Delta t = 5 \times 10^{-4}$. These simulations were conducted in situations ranging from the absence of a magnetic field, $Ca_{mag} = 0$ to higher intensity fields, $Ca_{mag} = 10$, both in the absence and in the presence of surfactant in a series of conditions, $E = 0.2$ and $E = 0.4$, $X = 0$ (absence of surfactant) to $X = 0.9$, and $Pe = 10^{-3}$ to $Pe = 10^{3}$. For this, we have considered a $[8 \times 8]$ non-dimensional domain, discretized by a regular 320×320 cell mesh. It is a domain that, although smaller than the one used by Cunha et al. (2020), also minimizes the effects of confinement by the channel walls on the droplet dynamics and magnetic field. Choosing this domain allows for greater mesh resolution using fewer cells. If we quantify, here we have $h = 0.025$, while in a domain $[12 \times 12]$ discretized by 416×416 we have $h = 0.0288$. The presence of the surfactant and the magnetic field action require the solution of two extra equations in relation to the conventional problems of droplets under shear flow. In addition, the surfactant increases the unsteady period of the simulation, and the evolution of the surfactant concentration over droplets requires the use of the closest point method. All this increases the computational cost. Therefore, decreasing the number of cells without damage to the mesh resolution is a good alternative to the problem addressed in this work.

4.2.1 Surfactant-free ferrofluid droplet

Here, some results of the two-dimensional numerical study conducted by Cunha et al. (2020) are reproduced. The work of Cunha et al. (2020) discusses more extensively the results of this section. We will comment on some aspects of the flow of magnetic droplets without surfactants that will be instructive for future discussions of this thesis. Interested readers should refer to the work of Cunha et al. (2020) for more details on the rheology of surfactant-free magnetic emulsions.

Figure 21 presents the droplet deformation and inclination, emulsion reduced viscosity, hydrodynamic and magnetic torques (normalized by $\eta\dot{\gamma}\beta$), magnetization (normalized by $\beta\mathbf{H}_0$), and the angle between the magnetic field and magnetization of the emulsion as a bulk fluid, both as a function of Ca_{mag} under horizontal and vertical external magnetic fields. Red and black symbols correspond to the present model and the work of Cunha et al. (2020), respectively.

Figure 21 shows a good agreement between the results of the present work and those

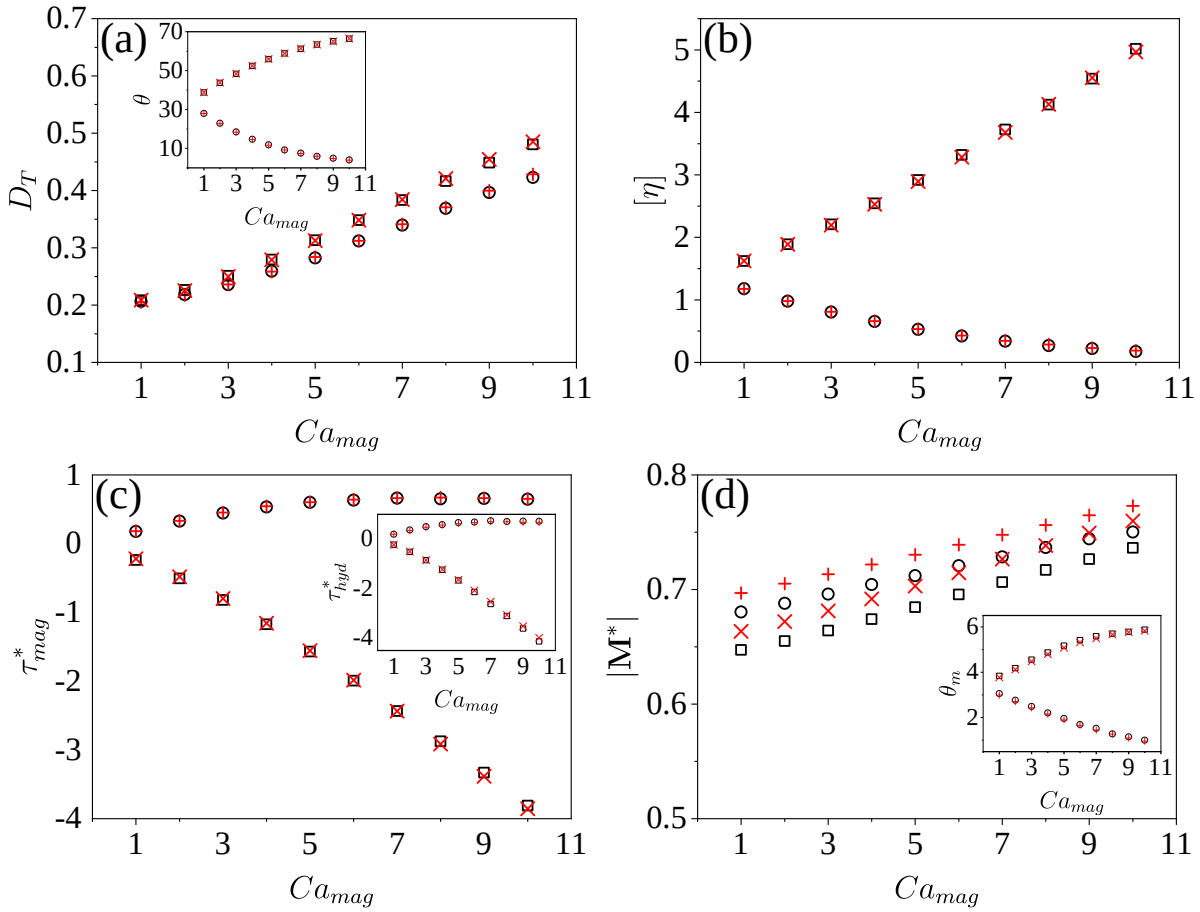

Figure 21 – (a) Taylor deformation, (b) reduced viscosity, (c) normalized magnetic torque, and (d) normalized magnetization. The insets of (a), (c) and (d), show the droplet inclination, hydrodynamic torque, and the misalignment angle between the bulk magnetization and the external magnetic field, respectively. Circles and cross (+) correspond to parallel external field; squares and cross (×) correspond to perpendicular external field. Results of Cunha et al. (2020) are represented by circles and squares.

of Cunha et al. (2020), suggesting good accuracy of the numerical methodology used. Table 2 shows the average deviation for Taylor deformation, droplet inclination, reduced viscosity, normalized magnetic and hydrodynamics torque, normalized magnetization, and angle between the magnetic field and the emulsion's magnetization when the external magnetic field is parallel and perpendicular to the main flow. It should be noted that although Cunha et al. (2020) have used the level set method, they did not use the area conservation procedure in the re-initialization of ϕ, which may explain some small differences between the results.

Figure 21(a) shows that as the magnetic field force increases, the Taylor deformation also increases, and the main droplet axis tends to become more aligned with the external field direction. Thus, when the external magnetic field is parallel to the flow direction, θ decreases with Ca_{mag} and approaches to zero for sufficiently large Ca_{mag} (at $Ca_{mag} = 10$, $\theta = 3.94°$, *vide* inset of Figure 21(a)). As the droplet is deformed along the field direction, it assumes a shape that imposes less resistance to the flow, both by weaker shear stress on

Table 2 – Average deviation for Taylor deformation, droplet inclination, reduced viscosity, normalized magnetic and hydrodynamics torque, normalized magnetization and angle between magnetic field and the emulsion's magnetization.

	Parallel field	Perpendicular field
D_T	0.50%	0.51%
θ	1.08%	0.18%
$[\eta]$	2.65%	0.61%
τ^*_{mag}	1.52%	2.26%
τ^*_{gyd}	4.00%	2.28%
$\lvert\mathbf{M}^*\rvert$	2.61%	2.79%
θ_m	2.73%	1.32%

the droplet and by reducing the sectional area in relation to the flow direction, decreasing the reduced viscosity, as presented in Figure 21(b). Although 21(d) shows the bulk magnetization increasing with Ca_{mag} in all cases, its inset shows that the angle between the magnetic field and the emulsion's magnetization has an opposite behavior for vertical and horizontal fields, increasing or decreasing, respectively, with Ca_{mag}. In fact, for a magnetic field parallel to the flow, the droplet is expected to become more aligned to the direction of the field, such that $\mathbf{M}^*$ and H_0 align to each other. Under these conditions, since the magnetic and hydrodynamic torques are proportional to $|\mathbf{M}*|$ and θ_m, the magnitude of magnetic and hydrodynamic torque is not an increasing function of Ca_{mag}, as can be seen in Figure 21(c).

On the other hand, when the external magnetic field is perpendicular to the flow direction, the opposite occurs. The external magnetic field magnetizes the ferrofluid droplet, while the shear rate rotates the bulk magnetization vector in the clockwise direction, leading to a misalignment between H_0 and $\mathbf{M}^*$ (CUNHA et al., 2020). The final equilibrium configuration depends on the balance between shear and magnetic forces. The magnetic field induces a droplet deformation in the vertical direction, increasing the magnitude of the magnetic and hydrodynamic torque, as can be seen, 21(c), that acts to rotate the droplet back to the flow direction. Thus, as the strength of the magnetic field increases, the droplet assumes a shape that imposes more resistance to the flow, both by stronger shear stresses in regions of high curvature and by presenting a larger cross-sectional area relative to the flow direction. The misalignment between the droplet and flow requires that the streamlines deflect to contour the droplet shape, increasing the reduced viscosity, as presented in Figure 21(b). Therefore, when the external magnetic field is perpendicular to the flow direction, D_T, θ, $[\eta]$, $|\tau^*_{mag}|$, $|\tau^*_{hyd}|$, $|\mathbf{M}^*|$, and θ_m increases with Ca_{mag}.

4.2.2 Effects of the magnetic field and surfactants on the surface properties

As shown in the section 4.1.2, the largest variations of surfactant concentration and forces on the interface occur when the surfactant transport is purely advective, $Pe = 10^3$. Therefore, here we considered this condition to study the effects of the magnetic field on these surface quantities. Another fundamental parameter to understand the surface quantities distribution in a two-dimensional problem is the droplet perimeter (or the Surface Area in a 3D case), which is directly related to the mean surface concentration due to the surfactant dilution. Figure 22 shows the droplet perimeter as function of X for $E = 0.2$, $Ca_{mag} = 0$ (+), $Ca_{mag} = 5$ (diamonds) and $Ca_{mag} = 10$ (circles). It is clear that the magnetic field action increases the droplet's perimeter, making its surface more elongated. However, the field direction has a small influence on the final perimeter of the droplet. On the other hand, increasing the surfactant coverage increases the droplet perimeter to the same Ca_{mag}, which is not surprising, since increasing X reduces the average surface tension coefficient over the droplet. However, none of these differences its compare to the effects of increasing Ca_{mag}, making it clear that the droplet perimeter is a stronger function of Ca_{mag} than the direction of the magnetic field and X.

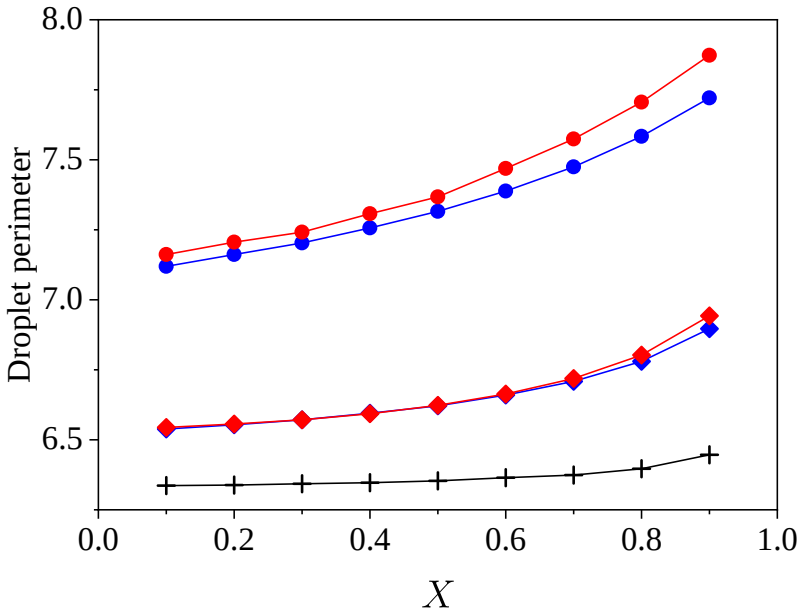

Figure 22 – Droplet perimeter at steady state under perpendicular (red) and parallel (blue) external magnetic field for $Ca_{mag} = 0$ (crosses), $Ca_{mag} = 5$ (diamonds) and $Ca_{mag} = 10$ (circles), when $Pe = 10^3$ and $E = 0.2$.

Increasing the droplet perimeter tends to globally decrease the surfactant concentration on its surface, this dilution process competes with the surfactant advection which tends to increase the surfactant concentration at the droplet tips. When Pe is low enough, no matter how much the flow sweeps the surfactant to the droplet's tips, the diffusion occurs instantaneously, reestablishing the concentration equilibrium. Under these conditions, increasing the perimeter causes a uniform decrease in the surfactant

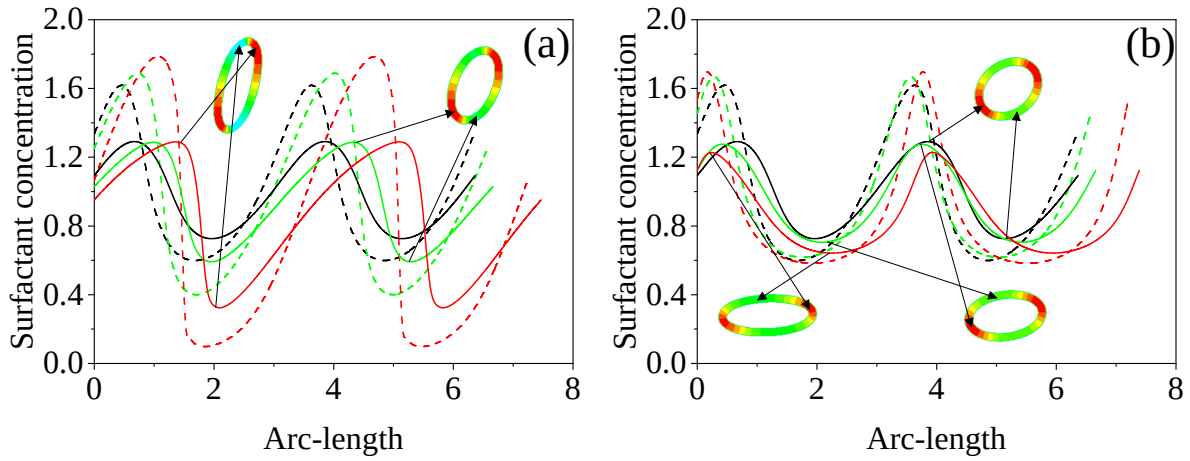

Figure 23 – Surfactant concentration under (a) vertical and (b) horizontal external magnetic field for $X = 0.3$ (dashed line) and $X = 0.6$ (continuous line), when $Pe = 10^3$, $E = 0.2$, $Ca_{mag} = 0$ (black), $Ca_{mag} = 5$ (green) and $Ca_{mag} = 10$ (red). The insets show droplets contours colored by surfactant concentration on a scale from (a) 0.1 (green) to 1.2 (red).

concentration over the droplet surface. As Pe increases, the surfactant behavior on the droplet surface deviates from that described previously, so that, for large Pe (which is the case in this work) the diffusion is not strong enough to rebalance the surfactant concentration, which will depend on both of the external flow conditions and the droplet perimeter growing. This behavior is discussed deeply in the following paragraphs.

Figures 23 and 24 present surfactant concentration and surface tension coefficient, respectively, as functions of the arc-length at the steady state for $E = 0.2$, $X = 0.3$ (dashed lines) and $X = 0.6$ (continuous lines), $Ca_{mag} = 0$ (black lines), $Ca_{mag} = 5$ (green lines), and $Ca_{mag} = 10$ red lines), where the arc-length coordinate starts at the point on the surface that crosses the x-axis and increases in the counterclockwise direction. In Figures 23 and 24, (a) and (b) correspond, respectively, to an external magnetic field perpendicular and parallel to the main flow direction.

Figure 23 shows that under an external magnetic field, the surfactant concentration presents a behavior different from that presented by non-magnetic droplets under shear flow. In the absence of a magnetic field, it is well known that the surfactant accumulates at the droplet tips. However, if the droplet is subjected to a perpendicular magnetic field, the inset of Figure 23(a) shows that the surfactant accumulates in a region posterior to the droplet tip (clockwise) because the droplet orientation causes the flow to sweep the surfactant, that would accumulate at the droplet tips, to a region that follows the vorticity direction. On the other hand, the inset of Figure 23(b) shows that when the magnetic field is parallel, the flow, which is weak near the channel center, sweeps the surfactant from regions of smaller curvature, accumulating in the anterior region of the droplet tips. In addition, note that although the concentration near the droplet tips is higher for $X = 0.3$ than for $X = 0.6$, the amount of surfactant is not, as c is normalized by the initial average surfactant concentration, as presented in section 2.3. This is evident in Figure 24, where

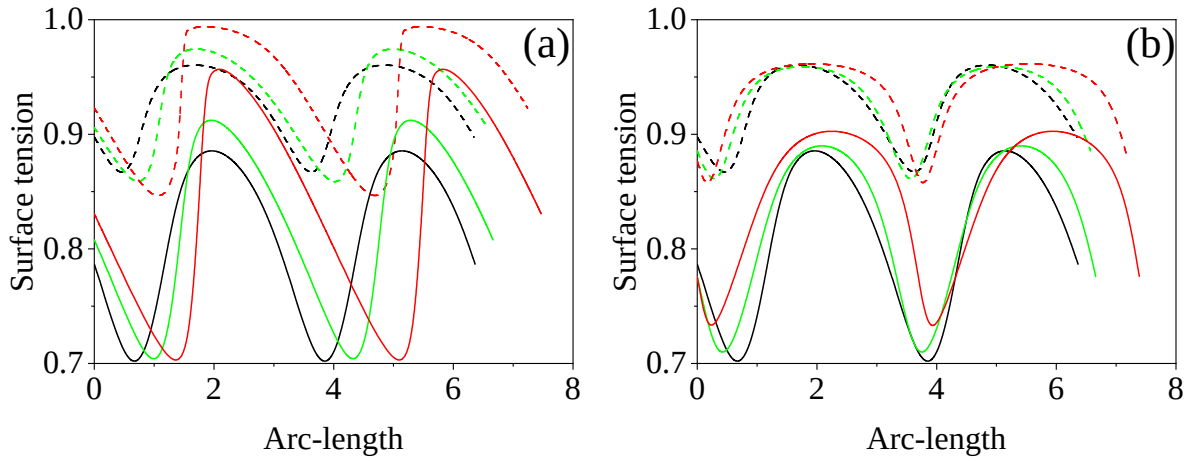

Figure 24 – Surface tension coefficient over droplet surface under (a) vertical and (b) horizontal external magnetic field for $X = 0.3$ (dashed line) and $X = 0.6$ (continuous line), when $Pe = 10^3$ and $E = 0.2$, $Ca_{mag} = 0$ (black), $Ca_{mag} = 5$ (green) and $Ca_{mag} = 10$ (red).

the lower surface tension coefficients occur for $X = 0.6$.

The droplet orientation is fundamental to understand this behavior of the surfactant concentration. If the magnetic field is perpendicular to the main flow direction, the droplet is elongated in a direction where its tips stay in regions that increases the shear rate on the droplet, making the advective effects more evident. This becomes clear by measuring the difference between the larger and the smaller concentration in each case. The bigger difference occurs for $X = 0.3$ and $Ca_{mag} = 10$, wherein the zones of smaller curvature the concentration approaches 0 and the surface tension coefficient approaches to 1 (Figure 24(a)). This condition is closer to a surfactant-free surface. Note that this difference is smaller when the magnetic field is parallel (Figure 23(b)), because the droplet is elongated in the flow direction, placing it in a flow region that decreases the local shear rate over its surface. Thus, the larger intensity of the magnetic field, the larger this effect. The flow weak action is not enough to sweep the same amount of surfactant to the droplet tip when compared to cases where the magnetic field is perpendicular.

In Figure 23(a) the peaks of higher surfactant concentration are close for both magnetic field intensities. The most significant differences are in the locations where these peaks occur and in the concentration of the more elongated regions. This behavior is a function of both the action of the external flow (which tends to sweep the surfactant) and dilution and the concentration at the maximum packing. As the flow sweeps the surfactant to near the droplet tips, it increases the surfactant concentration in these regions. If X is large enough, the amount of surfactant available on the droplet surface is also large and the droplet can have two maximum packing zones as the flow develops (provided Pe is also large enough). When the maximum packing is reached, the surfactant transport in this region is interrupted. This can be seen in Figure 23(a), where for $X = 0.6$ the maximum surfactant concentration is approximately the same for $Ca_{mag} = 0$, $Ca_{mag} = 5$

and $Ca_{mag} = 10$, suggesting that this is the maximum packing, as even with increasing surfactant dilution (due to increasing droplet perimeter with Ca_{mag}) the concentration peaks do not change. On the other hand, the surfactant dilution and transport to near the droplet tips decrease a lot the surfactant concentration in regions of small curvature as Ca_{mag} increases, considerably increasing the local surface tension coefficient (Figure 24(a)).

The same behavior is not observed for $X = 0.3$, where the surfactant amount on the droplet surface is not enough to achieve maximum packing concentration. Under these conditions, the surfactant concentration peaks are sensitive to changes in Ca_{mag} both for the parallel (Figure 23(b)) and perpendicular (Figure 23(a)), being that in this latter the sensibility is larger due to the increase in the shear rate over the droplet surface, caused by the droplet stretching towards the channel walls.

When the magnetic field is parallel (Figure 23(b)) and $X = 0.6$ the surfactant concentration peaks undergo small decreases as Ca_{mag} increases. This is due to the droplet configuration in a region of the channel where the shear rate is small, which reduces the flow capacity to sweep the surfactant to near of the droplet tips and offset the dilution effects. In this sense, it can be established that for a droplet whose maximum packing concentration is already reached at its tips when $Ca_{mag} = 0$, the action of the magnetic field can maintain these conditions when applied in a direction perpendicular to the main flow or disfavor it when applied in the same flow direction.

On the other hand, note in Figure 23(b) that when $X = 0.3$ the concentration peaks have an antagonistic behavior to those for $X = 0.6$ as Ca_{mag} increases, although the droplet is subject to the same conditions as external flow. This behavior suggests that it is easier to sweep surfactant when it is in small amounts along the droplet surface, so that even though the flow intensity decreases over the droplet surface when Ca_{mag} increases, the overall decrease of the surfactant concentration due to dilution facilitates the surfactant transport to near of the droplet tips, i.e., greater amounts of surfactant can be transported even at weaker flows, since X is small enough.

The surfactant distribution along the droplet surface directly affects the surface tension coefficient, as presented in Figure 24. Roughly speaking, for a given X, the higher the surfactant concentration, the lower the surface tension coefficient. In turn, the profile of σ along the droplet surface directly affects the profile of the normal and tangential components of the surface force. In this sense, Figures 25 and 26 present the signaled Marangoni and capillary forces, respectively, as functions of the arc-length at the steady state for $E = 0.2$, $X = 0.3$ (dashed lines) and $X = 0.6$ (continuous lines), $Ca_{mag} = 0$ (black lines), $Ca_{mag} = 5$ (green lines), and $Ca_{mag} = 10$ red lines), where (a) and (b) correspond, respectively, to an external magnetic field perpendicular and parallel to the main flow direction.

Figure 25(a) shows that near to the droplet tips, the signaled Marangoni force

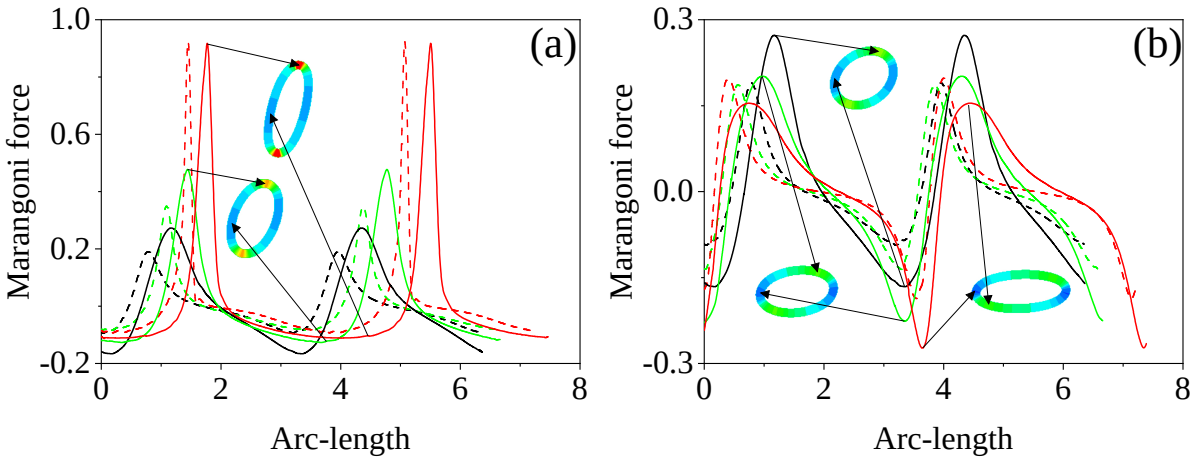

Figure 25 – Signaled Marangoni force magnitude under (a) vertical and (b) horizontal external magnetic field for $X = 0.3$ (dashed line) and $X = 0.6$ (continuous line), when $Pe = 10^3$, $E = 0.2$, $Ca_{mag} = 0$ (black), $Ca_{mag} = 5$ (green) and $Ca_{mag} = 10$ (red). The insets show droplets contours colored by Signaled Marangoni force on a scale from (a) -0.4 (blue) to 0.6 (red).

magnitude is zero due to symmetry and near these regions, presenting positive and negative peaks. In addition, the Marangoni forces variations increase with the surfactant coverage. When the magnetic field is perpendicular, the large variations of the surfactant concentration that occur at the droplet tips, as shown in Figure 23, lead to large values of $\nabla_s\sigma$ in these zones. A consequence of this is the positive peaks of the Marangoni force in Figure 25(a), which increases with Ca_{mag} and acts to resist the external flow, in the sense that the interface causes a shear stress slowing down the flow near the tips. Moreover, the insets of Figure 25(a) show that increasing Ca_{mag} move the point on the surface where $\mathbf{F}_m \cdot \hat{\mathbf{t}} > 0$ clockwise, that is, the resistance to the flow occurs in a smaller portion of the droplet surface as Ca_{mag} increases. However, this happens in a region where the flow intensity is stronger. This balance is fundamental to understanding the Marangoni stress effects on the emulsion rheology and will be discussed in more detail in the next sections.

When the magnetic field is parallel, Figure 25 (b) shows a different behavior of the Marangoni forces than those presented for a perpendicular field. Looking for the solid curves ($X = 0.6$) one observes that as the magnetic field gets stronger, the minimum value of the Marangoni force gets progressively smaller. As $\mathbf{F}_m \cdot \hat{\mathbf{t}}$ is negative, in these regions the tangential stress favors the external flow. As for the vertical field the maximum $\mathbf{F}_m \cdot \hat{\mathbf{t}}$ increases with Ca_{mag}, for a horizontal field, the minimum of $\mathbf{F}_m \cdot \hat{\mathbf{t}}$ decreases with Ca_{mag}. As already reported for the parallel field, the variations of the surfactant concentration along the arc-length become smaller as the droplet elongates in the flow direction. Therefore $\nabla_s\sigma$ decreases as Ca_{mag} increases, i. e., the absolute value of the Marangoni force decreases as the magnetic field becomes stronger in the flow direction. Comparing the insets in Figure 25(a) and (b), it is clear that $\mathbf{F}_m \cdot \hat{\mathbf{t}} < 0$ (blue zones) in a smaller portion of the droplet surface when the magnetic field is parallel, however in locations where $\mathbf{F}_m \cdot \hat{\mathbf{t}} > 0$ the shear stress is smaller than when the magnetic field magnetic is perpendicular.

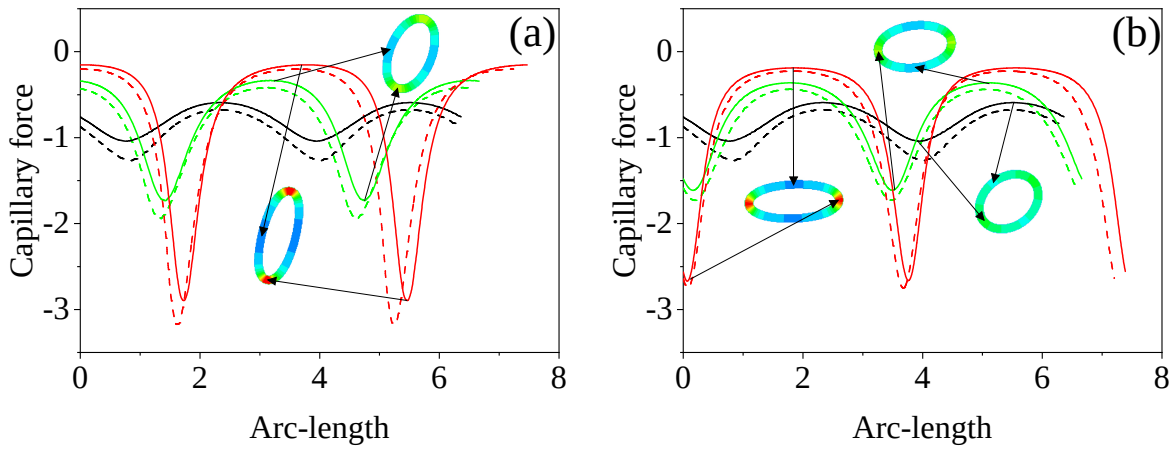

Figure 26 – Signaled capillary force magnitude under (a) vertical and (b) horizontal external magnetic field for $X = 0.3$ (dashed line) and $X = 0.6$ (continuous line), when $Pe = 10^3$, $E = 0.2$, $Ca_{mag} = 0$ (black), $Ca_{mag} = 5$ (green) and $Ca_{mag} = 10$ (red). The insets show droplets contours colored by Signaled capillary force on a scale from (a) -2.6 (red) to 0 (blue).

In contrast to the Marangoni forces, Figure 26 shows that the signal of the signaled capillary force magnitude doesn't change along the interface, and for the same Ca_{mag} is a weak function of the surfactant coverage and the magnetic field direction, which practically only changes the location of the force peaks. These results indicate that the signaled capillary force is a stronger function of local curvature than of surfactant distribution. As $\mathbf{F}_c \cdot \hat{\mathbf{n}} = -\sigma\kappa$, the decreasing σ due to the increasing concentration is compensated as the curvature increase. Note in Figure 26 that the signed magnitude of the capillary force is larger at the droplet tips due to the high curvature. As the droplet is elongated (Ca_{mag} increasing), the force magnitude increases, which indicates the tendency to compress the droplet fluid. Thus, variations in capillary force along the surface increase with the magnetic field intensity.

4.2.3 Effects of the surfactant and magnetic field in the droplet shape

It is well known that the shape of a magnetic droplet is influenced by the action of surfactants over the interface and by an external magnetic field. In this section, we study the combined influence of surfactants and the external field on droplet deformation and inclination. In all results presented in the next sections, the red, green, and blue lines correspond, respectively, to $Pe = 10^3$, $Pe = 1$, and $Pe = 10^{-3}$.

Figure 27(a-b) and (c-d) present, respectively, the Taylor deformation parameter and droplet inclination angle as functions of the surfactant coverage for three magnetic field intensities, $Ca_{mag} = 0$ (triangles), $Ca_{mag} = 5$ (squares), and $Ca_{mag} = 10$ (diamonds). In (a) and (c), (b) and (d) the droplet is subjected to perpendicular and parallel external magnetic fields, respectively. Figure 27 makes it clear that the Péclet number does not influence the droplet shape. The same was observed for non-magnetic emulsions (section

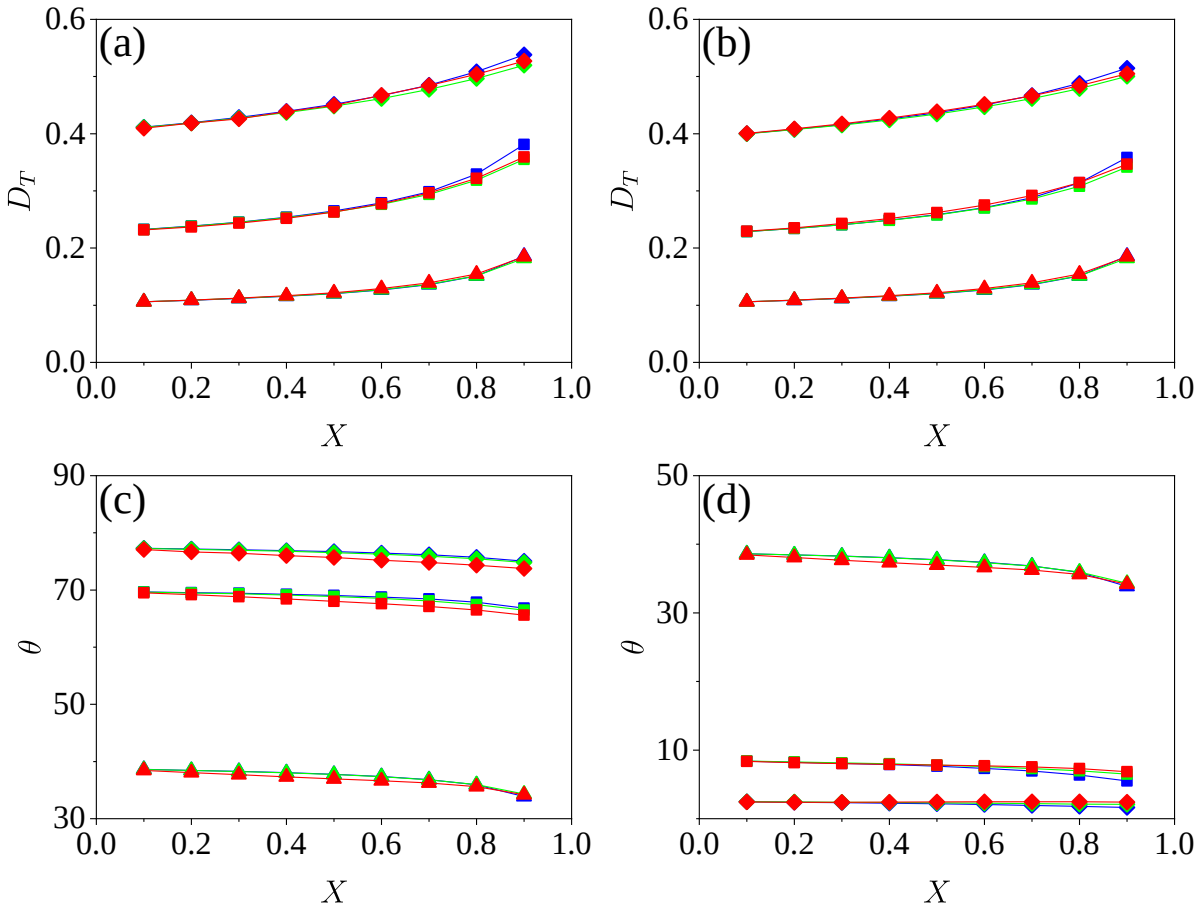

Figure 27 – Taylor deformation and droplet inclination as functions of surfactant coverage X for $E = 0.2$. (a) and (c) perpendicular field, (b) and (d) parallel field; $Pe = 10^3$ (red), $Pe = 1$ (green), and $Pe = 10^{-3}$ (blue); $Ca_{mag} = 0$ (triangles), $Ca_{mag} = 5$ (squares), and $Ca_{mag} = 10$ (diamonds).

4.1.3. Therefore, the presence of magnetic fields does not affect this particular aspect of the surfactant-covered droplet dynamics. For the same Ca_{mag}, D_T increases and θ decreases with X, regardless of the Pe and the magnetic field direction. On the other hand, increasing Ca_{mag} results in parallel deformation and inclination curves, i. e, the magnetic field displaces vertically the curves of D_T and θ as a function of X.

The contributions of X and Ca_{mag} to D_T and θ are given in different ways. The overall increase of X decreases the surface tension because higher X means more surfactant on the interface, favoring to deformation and aligning the droplet in the flow direction. In the presence of the magnetic field, the droplet is stretched in the field direction, and increasing X facilitates this process. The shear flow tends to decrease the droplet inclination as D_T (or X) increases. Moreover, if the magnetic field is perpendicular to the main flow direction, the magnetic force tends to increase the droplet inclination, as presented in Figure 27. When the magnetic field is parallel, Figure 27(d), both the flow and magnetic force tend to decrease the droplet inclination.

To explain these results, we plot in Figure 28 D_T and θ (insets) as a function of Ca_{mag} for (a) perpendicular and (b) parallel external magnetic field when $E = 0.4$,

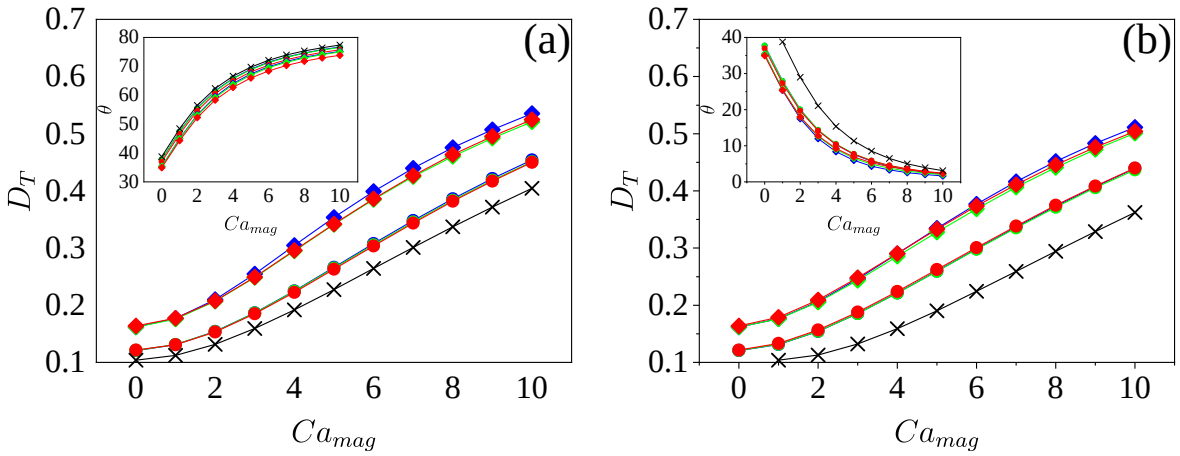

Figure 28 – Taylor deformation parameter as function of Ca_{mag} for $Pe = 10^3$ (red), $Pe = 1$ (green), and $Pe = 10^{-3}$ (blue) when $E = 0.4$, $X = 0.3$ (circles) $X = 0.6$ (diamonds), under (a) perpendicular and (b) parallel external magnetic field. The insets show the droplet inclination as function of Ca_{mag}. Black crosses corresponds to surfactant-free surface.

$X = 0.3$ (circles) and $X = 0.6$ (diamonds), under the same range of Péclet number as the Figure 27. The black curves correspond to surfactant-free ferrofluid droplets.

As a general rule, the droplet shape is a stronger function of Ca_{mag} than of X and E. The insets of Figure 28 make it clear that $|\partial\theta/\partial(Ca_{mag})|$ decreases as Ca_{mag} increases, i. e., the magnetic field effects on the droplet inclination gets weaker as it approaches to 90° (perpendicular field) and 0° (parallel field). As the droplet deforms towards the channel walls (perpendicular field), the flow's force (from the regions of higher velocity), which acts to bend the droplet, increases. Thus, the magnetic field effects on θ become weaker as Ca_{mag} increases. When the magnetic field is parallel, both the flow action and the magnetic field bend the droplet to the horizontal axis. So θ is closer to zero (under parallel field) than 90° (under perpendicular field). On the other hand, $\partial D_T/\partial(Ca_{mag})$ undergoes few changes along the Ca_{mag} range. Logically, by increasing the magnetic field strength we would obtain a behavior of D_T similar to that of θ, and for some cases (depending on Ca), even the droplet breakup would be reached (CUNHA et al., 2018).

The results of this section showed that the droplet shape is not a function of Pe, either for magnetic or non-magnetic emulsions. On the other hand, the direction of the magnetic field does not (or little affects) the Taylor deformation. Already the behavior of θ depends on the field direction. These patterns of D_T and θ are the same as those observed for surfactant-free droplets. Although the surfactant presence increases the droplet deformation and decreases its inclination, i. e. vertically displaces the curves of D_T and θ versus Ca_{mag}.

4.2.4 Combined effect of surfactant and magnetic field on the emulsion rheology

In section 4.1.4 we presented results of surfactant effects on the rheology of non-magnetic emulsions. On the other hand, magnetic field effects were presented by Cunha et al. (2018), Cunha et al. (2020). Here, we study how the magnetic field affects the rheology of surfactant-covered ferrofluid droplet emulsions in terms of the Marangoni, capillary, magnetic and reduced viscosities. These material functions are presented in terms of Ca_{mag} for $E = 0.4$ and two coverage factors, $X = 0.3$ (circles) and $X = 0.6$ (diamonds). In addition, we consider $Pe = 10^{-3}$ (blue), $Pe = 1$ (green), and $Pe = 10^{3}$ (red).

4.2.4.1 Marangoni viscosity

Figures 29 and 30 presents the Marangoni viscosity as a function of (a) Ca_{mag} and (b) θ when the droplet is subjected to a perpendicular and parallel external magnetic field, respectively. The insets of Figures 29(a) and 30(a) show the Marangoni viscosity as function of surfactant coverage, X, for $E = 0.2$, $Ca_{mag} = 0$ $(+)$, $Ca_{mag} = 5$ $(\times)$ and $Ca_{mag} = 10$ $(*)$. In addition, some droplet contours, colored by the signaled Marangoni force magnitude, are shown in (a) and (b).

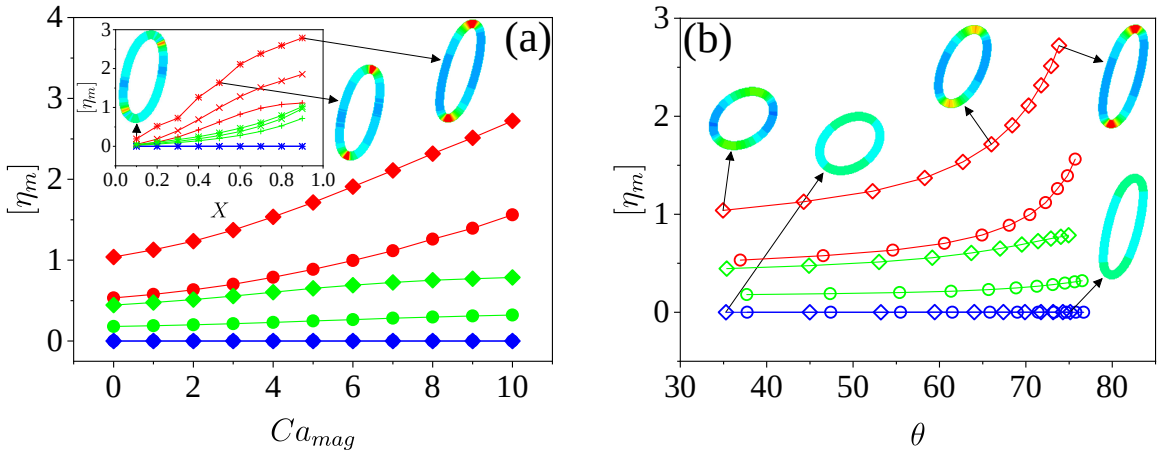

Figure 29 – Marangoni viscosity as function of (a) Ca_{mag} and (b) θ for $E = 0.4$, $X = 0.3$ (circles) and $X = 0.6$ (diamonds), $Pe = 10^{-3}$ (blue), $Pe = 1$ (green), and $Pe = 10^{3}$ (red) under a perpendicular external magnetic field. The insets show Marangoni viscosity as function of X, for $E = 0.2$, $Ca_{mag} = 0$ $(+)$, $Ca_{mag} = 5$ $(\times)$ and $Ca_{mag} = 10$ $(*)$; and some droplets contours colored by Signaled Marangoni force from -0.4 (blue) to 0.6 (red).

Figure 29 shows that when the advective effects cannot be neglected ($Pe = 1$ and, mainly, $Pe = 10^{3}$) the Marangoni viscosity increases with the magnetic field intensity over the entire range of X and E. As a general rule, the magnetic field changes the surfactant distribution on the droplet surface, which in turn changes the Marangoni forces and consequently the $[\eta_m]$, i.e., the emulsion rheology. This is a combined effect of the droplet

orientation, deformation and the signaled Marangoni force magnitude over the interface. It should be noted that the inclination angle varies just slightly with X (Figure 27) and the variations of $[\eta_m]$ are not correlated to the relative inclination of the droplet along the X range.

As presented in the previous section, the action of a perpendicular magnetic field increases the droplet inclination and deformation, delays the decrease of θ with X, and increases the Marangoni force peaks at the droplet tips. Thus, the increase of Ca_{mag} leads these peaks to regions of higher local shear rate inside the flow, as seen in the droplet contours colored by signaled Marangoni force magnitude. As these forces act to resist the flow, $[\eta_m]$ increases with Ca_{mag}. This happens for any E and X, becoming more significant as E and/or X grows (see Figure 25), due to the increases of the droplet deformation, of the $\mathbf{F}_m \cdot \hat{\mathbf{t}}$ peaks, and of the surface portion where $\mathbf{F}_m \cdot \hat{\mathbf{t}} > 0$.

Figure 29(b) makes it clear that, for $Pe = 10^3$, $[\eta_m]$ becomes a stronger function of θ as Ca_{mag} increases. As shown in Figure 28, $\partial\theta/\partial Ca_{mag}$ decreases as θ approaches to $\pi/2$, due to the competition between the magnetic field (which tends to bend the droplet to the vertical direction) and the flow (which tends to bend the droplet to the horizontal direction). On the other hand, $\partial D_T/\partial Ca_{mag}$ tends to remain almost constant over the studied range of Ca_{mag}. In other words, the droplet tends to stop skewing as Ca_{mag} increases, but it keeps stretching. Combining this with the results of the Marangoni force presented in section 4.2.2, it is noted that the intensity of $\nabla_s\sigma$ near the droplet tips increases significantly with Ca_{mag} by the combined action of the droplet elongation, which causes the surfactant dilution, and by the flow action, which becomes stronger at the droplet tips as D_T increases.

On the other hand, if the advective effects are small, $Pe = 10^{-3}$, the Marangoni viscosity tends to zero regardless of E, X, and Ca_{mag}. The droplet contours in Figure 29 show that there is a small difference between the Marangoni forces that act in large and small curvature regions since at low Pe, the surfactant tends to uniformly distribute, reducing the surface tension, and hence the $\nabla_s\sigma$ on the entire interface. Our results make it clear that the Marangoni viscosity is a stronger function of Pe than of Ca_{mag}, X or E, that is, η_m is a function of the surfactant distribution over droplet surface.

When the magnetic field is parallel to the main flow direction, Figure 30(a) shows that increasing the field intensity results in an opposite behavior to that observed for $[\eta_m]$ when the magnetic field is perpendicular, i. e., $[\eta_m]$ becomes a decreasing function of Ca_{mag}, although remains increasing with E, X, Pe, and θ (Figure 30(b)). This is because the Marangoni forces along the surface decrease with Ca_{mag} (see Figure 25), resulting in larger negative peaks of $\mathbf{F}_m \cdot \hat{\mathbf{t}}$, that act in favor to the flow and tend to decrease $[\eta_m]$. Furthermore, the droplet elongation in the flow direction leads the droplet surface locations where $\mathbf{F}_m \cdot \hat{\mathbf{t}} > 0$ (green region of the droplet contours) to regions of smaller local shear rate, decreasing the contribution from the tangential stress jump to the reduced viscosity.

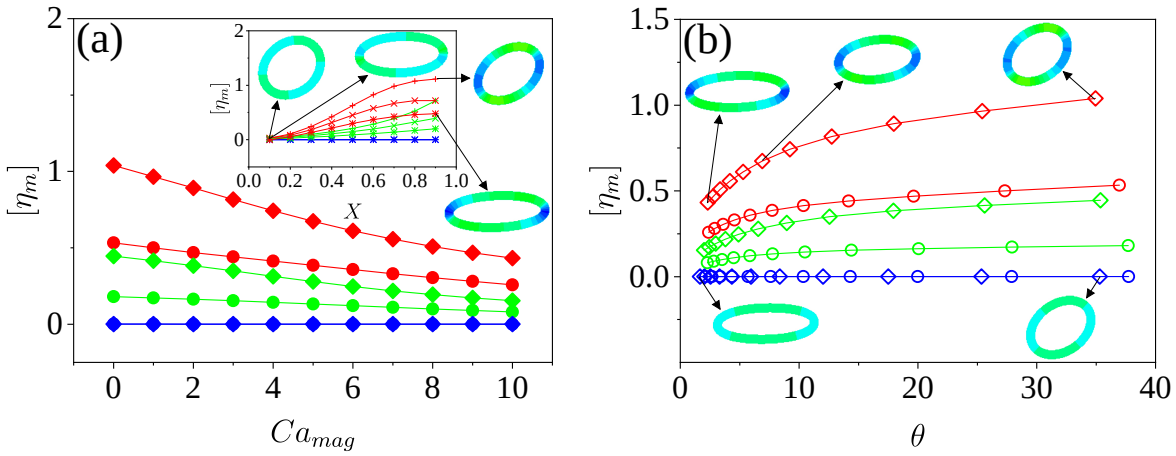

Figure 30 – Marangoni viscosity as function of (a) Ca_{mag} and (b) θ for $E = 0.4$, $X = 0.3$ (circles) and $X = 0.6$ (diamonds), $Pe = 10^{-3}$ (blue), $Pe = 1$ (green), and $Pe = 10^3$ (red) under a parallel external magnetic field. The insets show Marangoni viscosity as function of X, for $E = 0.2$, $Ca_{mag} = 0$ (+), $Ca_{mag} = 5$ ($\times$) and $Ca_{mag} = 10$ ($*$); and some droplets contours colored by Signaled Marangoni force from -0.4 (blue) to 0.6 (red).

Figures 29(b) and 30(b) show that $[\eta_m]$ is always an increasing function of θ, since η_m is directly related to the relative position of the droplet surfaces regions where $\mathbf{F}_m \cdot \hat{\mathbf{t}} > 0$ inside the flow. The insets of Figures 29(a) and 30(a) illustrate the behavior of $[\eta_m]$ for different magnetic field direction. For perpendicular fields, increasing Ca_{mag} results in a positive vertical displacement of the curves $[\eta_m] \times X$ due to the relationship between increasing shear rate over the droplet and the location of the positive peaks of Marangoni force, which acts to resist the flow. When the field is parallel this displacement is negative, because in addition to the Marangoni forces along the droplet surface (see Figure 25) are smaller than when the magnetic field is perpendicular, the droplet configuration inside the channel decreases the shear rate over it.

On the other hand, Figure 30 shows that the variations of E, X, and Pe result in similar effects (although of lower intensity) to those shown in Figure 29, since η_m remains an increasing function of these quantities. Even though the parallel magnetic field elongates the droplet in the flow direction, decreasing the shear rate on the droplet, the increase of the surfactant elasticity (E) and/or the amount (X), as well of the advective effects (Pe), result in the growth of $\nabla_s \sigma$ and consequently of η_m.

4.2.4.2 Capillary viscosity

Figures 31 and 32 present the capillary viscosity as a function of (a) Ca_{mag} and (b) D_T when the droplet is subjected to a perpendicular and parallel external magnetic field, respectively. Some droplet contours colored by the signaled capillary force magnitude are indicated in both (a) and (b), in the scale from 0 (blue) to -2.6 (red). In addition, the insets of Figures 31(a) and 32(a) show the capillary viscosity as a function of surfactant

coverage, X, under same conditions of the previous section.

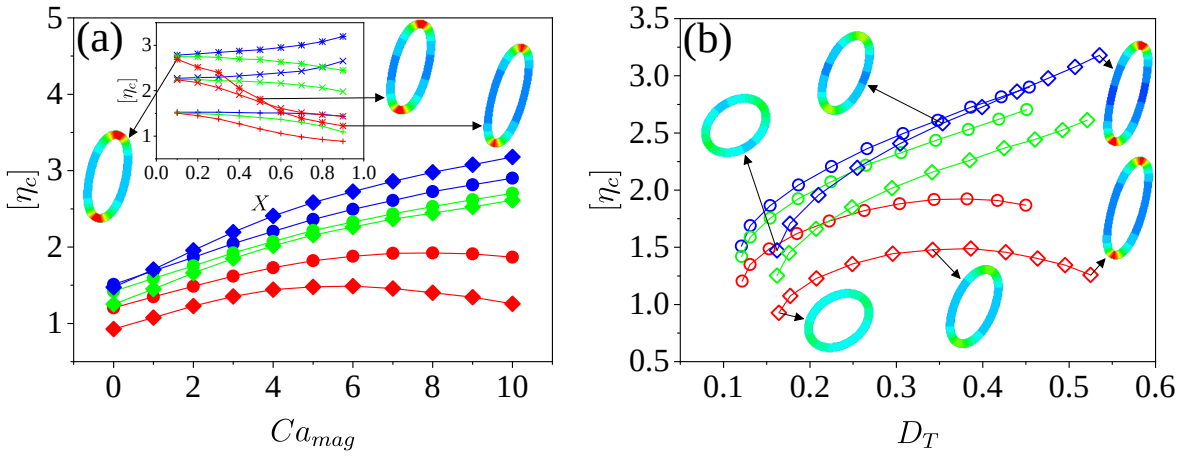

Figure 31 – Capillary viscosity as function of (a) Ca_{mag} and (b) D_T for $E = 0.4$, $X = 0.3$ (circles) and $X = 0.6$ (diamonds), $Pe = 10^{-3}$ (blue), $Pe = 1$ (green), and $Pe = 10^3$ (red) under a perpendicular external magnetic field. The insets show capillary viscosity as function of X, for $E = 0.2$, $Ca_{mag} = 0$ (+), $Ca_{mag} = 5$ ($\times$) and $Ca_{mag} = 10$ ($*$); and some droplets contours colored by absolute capillary force from 0 (blue) to -2.6 (red).

Figure 31(a) shows that the presence of the magnetic field alters the effects of X on $[\eta_c]$ in the Pe range studied. When $Pe = 10^{-3}$, increasing Ca_{mag} results in lower $[\eta_c]$ for $X = 0.3$ (circles) than for $X = 0.6$ (diamonds). The opposite is observed when $Pe = 1$ and especially when $Pe = 10^3$. In addition, the inset of Figure 31(a) makes it evident that in the absence of a magnetic field, $[\eta_c]$ is a decreasing function of E and X. That is, when the amount of surfactant increases or a more elastic surfactant is used, the surface tension coefficient decreases, leading to a decrease of $[\eta_c]$. If the surface flow maintains a convective

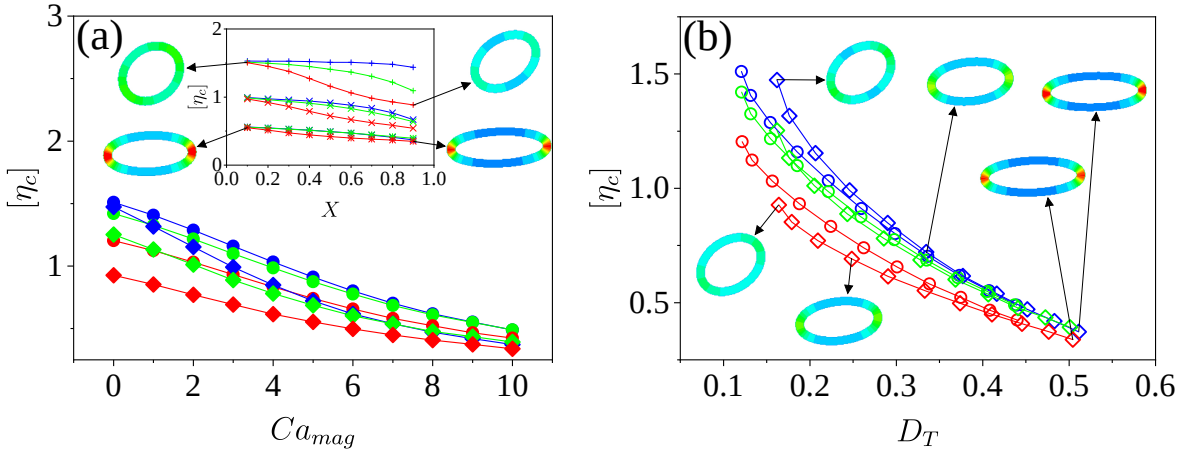

Figure 32 – Capillary viscosity as function of (a) Ca_{mag} and (b) D_T for $E = 0.4$, $X = 0.3$ (circles) and $X = 0.6$ (diamonds), $Pe = 10^{-3}$ (blue), $Pe = 1$ (green), and $Pe = 10^3$ (red) under a parallel external magnetic field. The insets show capillary viscosity as function of X, for $E = 0.2$, $Ca_{mag} = 0$ (+), $Ca_{mag} = 5$ ($\times$) and $Ca_{mag} = 10$ ($*$); and some droplets contours colored by absolute capillary force from 0 (blue) to -2.6 (red).

transport rate of surfactant dominant compared to diffusion, these effects become more evident, because the concentration peaks near the droplet tips cause abrupt reductions in σ in these regions and a small increase of σ in regions of low curvature. These differences can be observed by comparing the droplets contours colored by signaled capillary force magnitude, although the differences are not as evident as in the case of Marangoni forces. This is because even under the effect of external magnetic fields, Pe has little effect on the droplet shape, that is, on κ. On the other hand, the effects of Pe on σ are significant. It should be noted that the variations in the numerical values of κ along a deformed droplet are significantly larger than in the numerical values of σ. Thus, since $\mathbf{F}_c = -\sigma\kappa\hat{\mathbf{n}}\delta_\varepsilon(\phi)$, variations of σ cause smaller numerical variations in $\mathbf{F}_c \cdot \hat{\mathbf{n}}$ than κ, although this does not mean less effect on rheology.

Figure 31(b) shows that the behavior of $[\eta_c]$ is directly related to the surfactant distribution on the droplet surface, unlike what occurs in surfactant-free droplets, where $[\eta_c]$ is a direct function of the droplet shape. This behavior becomes even clearer when analyzing the contours of droplets of the inset of Figure 31(a). Note that the droplet becomes more elongated in the perpendicular flow direction as X increases. If we just look at the droplet shape, leaving aside the surfactant distribution on the surface, the highest flow resistance would occur for $Ca_{mag} = 10$ and $X = 0.9$, which is precisely the case where $[\eta_c]$ presents the smallest values.

As the droplet shape is not a function of Pe, there are no significant variations in the curvature at the droplet tips for the Pe range studied, and the behavior of $[\eta_c]$ is an exclusive function of the surfactant concentration in these regions. When $Pe = 10^{-3}$ the diffusive effects tend to maintain a constant concentration along the droplet surface, evidencing the effects of the surfactant dilution caused by the droplet elongation. These phenomena reduce the surfactant concentration at the droplet tips in relation to the cases of $Pe > 1$, increasing the surface tension coefficient in these regions. Thus, the increase of Ca_{mag} increases $|\mathbf{F}_c \cdot \hat{\mathbf{n}}|$ at the droplet tips, i. e., increases the droplet surface normal stress jump and consequently $[\eta_c]$.

For $Pe = 1$, and mainly $Pe = 10^3$, the curves of $[\eta_c]$ are a decreasing function of X regardless of the magnetic field, which in turn causes a positive vertical displacement of these curves as its intensity increases. These effects are a combination of the surfactant advection and droplet deformation. It is well known that a greater amount of surfactant is swept to near the droplet tips as Pe increases, reducing $|\mathbf{F}_c \cdot \hat{\mathbf{n}}|$ in these regions. In turn, the magnetic field action increases the droplet deformation, reducing κ at the regions of smaller surfactant concentration and increasing it at larger concentration regions. Thus, it is possible to divide the droplet into two regions as Ca_{mag} increases: one in which the local shear rate is smaller, κ decreases (longer droplet portion), and σ increases (due to the surfactant being swept to the droplet tips); and another in which the local shear rate is higher, κ increases (droplet tips) and σ decreases by surfactant accumulation. The balance of this antagonistic behavior is what determines $[\eta_c]$. When the surfactant advection

cannot be neglected, an increase of X under the same Ca_{mag} causes the σ reduction effects near the droplet tips to overcome those of the curvature increase in these regions and, therefore, $[\eta_c]$ decreases with X, as presented in inset of Figure 31(a). This decrease is more pronounced in the curve of $Ca_{mag} = 10$ and $Pe = 10^3$, where for $X = 0.8$ $[\eta_c]$ is the same order as those of a surfactant-free emulsion. In a way, this result indicates that the magnetic field cancels out the mechanical (or rheological) effects of surfactant with respect to $[\eta_c]$. However, we expect that other effects, such as emulsion stabilization, will remain preserved.

Fixing the surfactant coverage factor and elasticity, Figures 31(a) and (b) show that for $Pe \leq 1$ $[\eta_c]$ increases with Ca_{mag} and D_T. As surfactant advection is at most equivalent to diffusion under these conditions, the amount of surfactant transported to near the droplet tips is not sufficient to reduce $|\mathbf{F}_c \cdot \hat{\mathbf{n}}|$ in these regions to the point of to decrease $[\eta_c]$ when the field intensity increase. Furthermore, as the droplet deformation/inclination is a stronger function of Ca_{mag} than other quantities related to surfactant, the dilution effects, which increase σ over the droplet, become more evident as Pe decreases and Ca_{mag} increases.

On the other hand, when Pe is high, the surfactant dilution is restricted to the most elongated parts of the droplets, being overcome by the surfactant advection near the droplet tips. Thus, more surfactant is swept to these regions, decreasing $|\mathbf{F}_c \cdot \hat{\mathbf{n}}|$. For $Ca_{mag} \geq 5$, the effects of this reduction overcome the growth of $|\mathbf{F}_c \cdot \hat{\mathbf{n}}|$ on the more elongated part of the droplet, and therefore $[\eta_c]$ which starts decreasing with Ca_{mag}. In other words, the surfactant effects on the droplet regions of larger curvature become dominant over $[\eta_c]$ from a critical Ca_{mag}. For example, when $E = 0.4$, $X = 0.6$ and $Ca_{mag} = 10$ the maximum and minimum absolute values of $\mathbf{F}_c \cdot \hat{\mathbf{n}}$ are, respectively, 2.70 and 0.10 for $Pe = 10^3$, while for $Pe = 10^{-3}$ these values are 3.01 and 0.09. Therefore, non-monotonic variation of the $[\eta_c]$ when $Pe = 10^3$ arises from the antagonistic behavior of κ and σ. Furthermore, note that this critical Ca_{mag} only occurs in curves of $Pe = 10^3$ (see Figure 31(a)), evidencing that there is also a critical Pe between 0 and 10^3 from which the curves $[\eta_c] \times Ca_{mag}$ invert its behavior.

When the magnetic field is parallel to the main flow direction, Figure 32 shows an inverse behavior to that observed when the field is perpendicular. Here, $[\eta_c]$ is always a decreasing function of E, X, Pe and Ca_{mag}. In the inset of Figure 32(a) the action of the magnetic field displaces negatively the curves of $[\eta_c]$ as a function of X, in addition, to reduce the effects of Pe, so that for $Ca_{mag} = 10$ the results for $Pe = 10^{-3}$ and $Pe = 10^3$ are almost identical. This is because the droplet is localized in a flow region where there is no effective $\dot{\gamma}$ to promote surfactant transportation. So, even though the advective effects are strong, the shear rate is not enough to cause the same variations in the surfactant concentration and, consequently, in the surface tension coefficient that occurs when the magnetic field is perpendicular. Therefore, $|\mathbf{F}_c \cdot \hat{\mathbf{n}}|$ becomes a stronger function of curvature than of σ. Associated with this, the changes of the droplet shape with the growth of Ca_{mag}

decreases the shear rate on the droplet, reducing the normal voltage jump at the interface and consequently $[\eta_c]$.

This behavior becomes more evident comparing the Figures 32(a) and (b), where the increasing of magnetic field intensity decreases the variations of $[\eta_c]$ with X and Pe. It is clear that when the magnetic field is parallel to the main flow direction, the contributions of capillary forces to the reduced viscosity are much more related to droplet deformation than to the previously mentioned parameters. As D_T increases (due to increasing of Ca_{mag}), the amount of surfactant on the droplet surface, as well its elasticity or advection rate, cease to influence $[\eta_c]$, which tends to its minimum value when the deformation tends to the maximum since under these conditions the droplet assumes the shape that imposes less resistance to the flow.

4.2.4.3 Magnetic viscosity

Now, Figures 33 and 34 present the magnetic viscosity as a function of (a) Ca_{mag} and (b) D_T when the droplet is subjected to perpendicular and parallel external magnetic field, respectively. The insets of Figures 31(a) and 32(a) show the magnetic viscosity as a function of surfactant coverage, X, under same conditions of section 4.2.4.1. Note that in all curves shown the effects of Pe are very small, that is, the magnetic viscosity is independent of the surfactant distribution on the droplet surface.

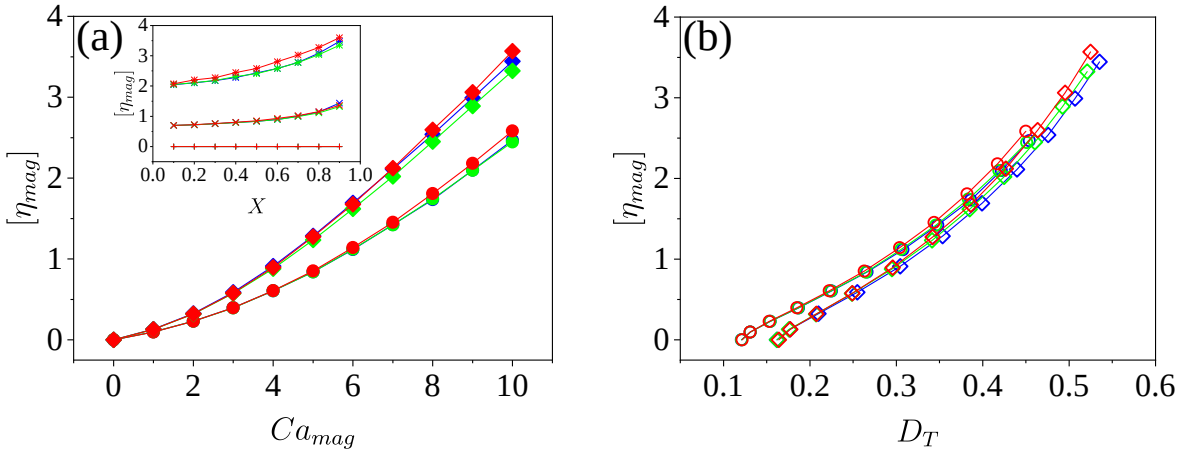

Figure 33 – Magnetic viscosity as function of (a) Ca_{mag} and (b) D_T for $E = 0.4$, $X = 0.3$ (circles) and $X = 0.6$ (diamonds), $Pe = 10^{-3}$ (blue), $Pe = 1$ (green), and $Pe = 10^3$ (red) under a perpendicular external magnetic field. The inset of (a) shows magnetic viscosity as function of X, for $E = 0.2$, $Ca_{mag} = 0$ $(+)$, $Ca_{mag} = 5$ $(\times)$ and $Ca_{mag} = 10$ $(*)$.

When the magnetic field is perpendicular, Figures 33(a) shows that $[\eta_{mag}]$ increases with Ca_{mag} and X, because these parameters directly influence the droplet deformation. This behavior is easily explained in Figure 33(b), where the plotted curves tend to coincide regardless of the surfactant related parameters, making it clear that $[\eta_{mag}]$ is a quasi-exclusive function of D_T. Also, note that the positive values of $[\eta_{mag}]$ contribute to

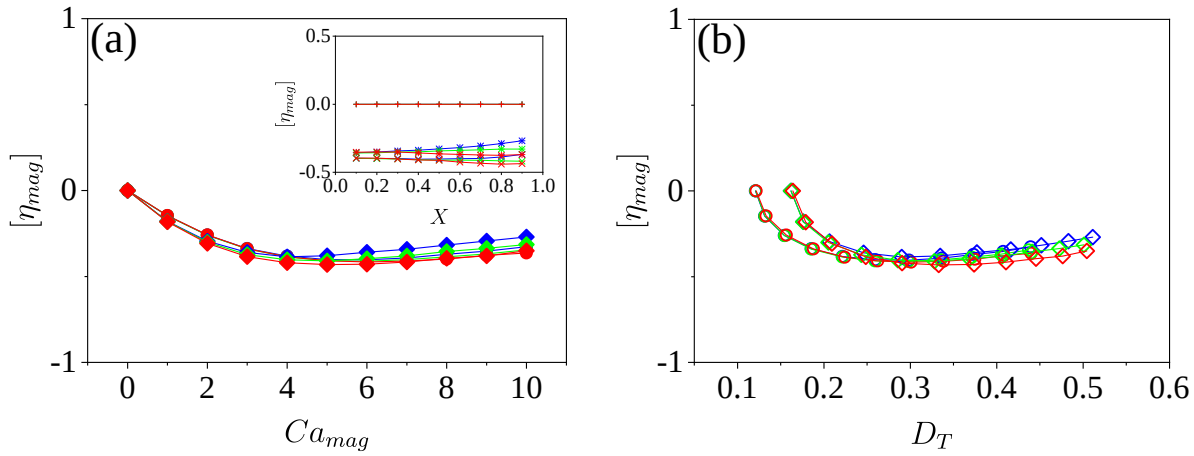

Figure 34 – Magnetic viscosity as function of (a) Ca_{mag} and (b) D_T for $E = 0.4$, $X = 0.3$ (circles) and $X = 0.6$ (diamonds), $Pe = 10^{-3}$ (blue), $Pe = 1$ (green), and $Pe = 10^3$ (red) under a parallel external magnetic field. The inset of (a) shows magnetic viscosity as function of X, for $E = 0.2$, $Ca_{mag} = 0$ (+), $Ca_{mag} = 5$ ($\times$) and $Ca_{mag} = 10$ ($*$).

increasing the reduced viscosity of the emulsion because the action of the perpendicular magnetic field puts the droplet in a position that increases the resistance to the flow.

On the other hand, when the magnetic field is parallel, Figures 34(a) and (b) show that $[\eta_{mag}]$ is a weak function of Ca_{mag} and consequently D_T since the droplet configuration within the channel does not have large effects on the flow. Under these conditions, the droplet alignment facilitates the flow, so that $[\eta_{mag}]$ has negative values of small magnitude. Therefore, the magnetic viscosity contributes to decreasing the emulsion reduced viscosity.

4.2.4.4 Reduced viscosity

The reduced viscosity $[\eta]$ is the sum of $[\eta_c]$, $[\eta_m]$, and $[\eta_{mag}]$. So that, its variations can be analyzed in terms of the $[\eta_c]$, $[\eta_m]$ and $[\eta_{mag}]$ as a function of Ca_{mag}, Pe and X. Figures 35(a) and (b) show the reduced viscosity as a function of Ca_{mag} and X, respectively, when the droplet is subjected to a perpendicular magnetic field. Figures 36(a) and (b) correspond to the same previous conditions under a parallel magnetic field. It is clear that the behavior of $[\eta]$ presented in section 4.1.4 is largely affected by the magnetic field action, which has a direct effect on the droplet shape and the surfactant distribution.

When the magnetic field is perpendicular, the surfactant effects always cause a positive displacement of the curves of $[\eta]$ as a function of Ca_{mag} [Figure 35(a)]. This is not surprising, since the surfactant reduces the surface tension, increasing the droplet's deformation in the external magnetic field direction and consequently its resistance to the flow. This happens even when the surfactant is evenly distributed over the droplet surface ($Pe = 10^{-3}$), and the Marangoni viscosity tends to zero. In this specific case, the growth of $[\eta]$ is due to the increase of $[\eta_c]$ and $[\eta_{mag}]$. However, the effects of Ca_{mag} on $[\eta]$ become more evident when X or Pe increase, since in this case the Marangoni viscosity cannot

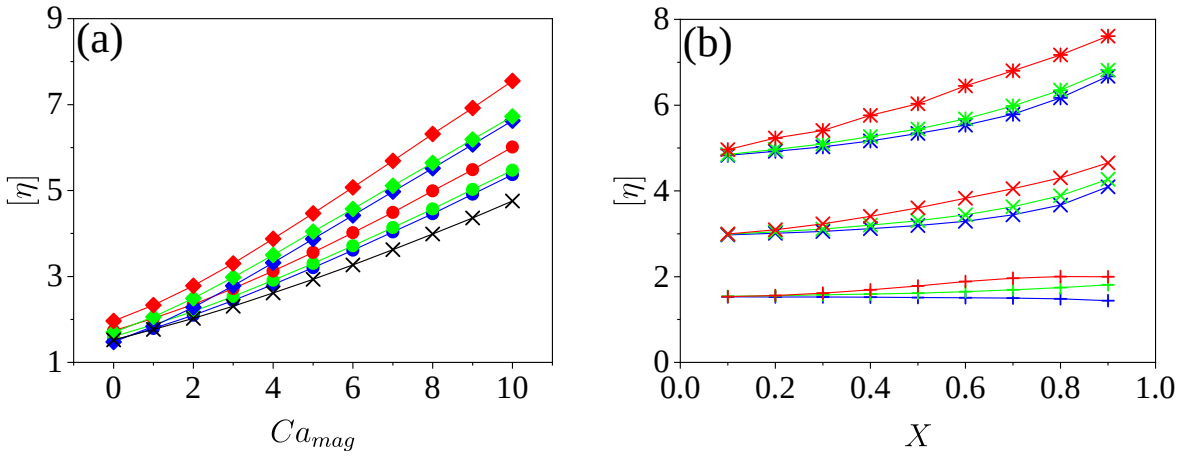

Figure 35 – (a) Reduced viscosity as function of Ca_{mag} for $E = 0.4$, $X = 0.3$ (circles) and $X = 0.6$ (diamonds). Black crosses corresponds to surfactant-free surface. (b) Reduced viscosity as function of X, for $E = 0.2$, $Ca_{mag} = 0$ (+), $Ca_{mag} = 5$ (×) and $Ca_{mag} = 10$ (∗). Perpendicular field for $Pe = 10^3$ (red), $Pe = 1$ (green), and $Pe = 10^{-3}$ (blue).

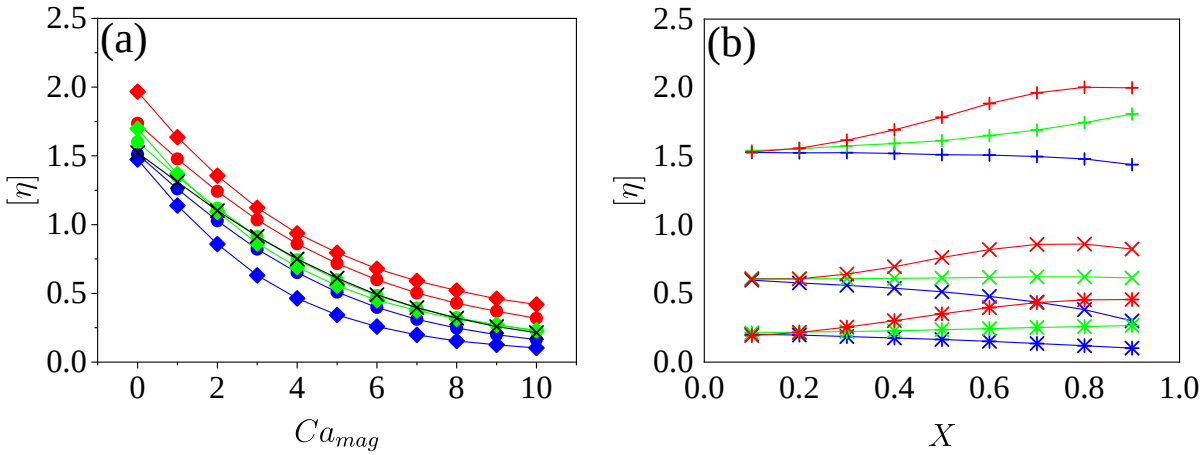

Figure 36 – (a) Reduced viscosity as function of Ca_{mag} for $E = 0.4$, $X = 0.3$ (circles) and $X = 0.6$ (diamonds). Black crosses corresponds to surfactant-free surface. (b) Reduced viscosity as function of X, for $E = 0.2$, $Ca_{mag} = 0$ (+), $Ca_{mag} = 5$ (×) and $Ca_{mag} = 10$ (∗). Parallel field for $Pe = 10^3$ (red), $Pe = 1$ (green), and $Pe = 10^{-3}$ (blue).

be neglected. So, even in the specific case where $\partial[\eta_c]/\partial Ca_{mag} \leq 0$ (for $Ca_{mag} \geq 5$ and $Pe = 10^3$), the reduced viscosity continues to be a growing function of Ca_{mag} due to the magnetic and Marangoni viscosities. Figure 35(b) makes it clear how the magnetic field affects the $[\eta] \times X$ curves, positively displacing them as Ca_{mag} increases. This is due to the increase of $[\eta_m]$ and $[\eta_{mag}]$ with X, since under magnetic field and $Pe \geq 1$, $[\eta_c]$ is a decreasing function of X [see inset of Figure 31(a)]. Also note that $\partial[\eta]/\partial X$ increases with X and Ca_{mag}, which is due to $\partial[\eta]_m/\partial X$, which is larger than $\partial[\eta]_{mag}/\partial X$.

The same behavior is not observed when the magnetic field is parallel to the main flow direction (Figure 36). Under these conditions, Marangoni, capillary, and magnetic viscosities are decreasing functions of Ca_{mag}, and consequently, the reduced viscosity has

the same behavior. The difference is that, here, it is possible to separate the curves as functions of Pe. Note that for $Pe = 1$, $[\eta]$ curve gets closer to those for a surfactant-free droplet as Ca_{mag} increases, being positively displaced when $Pe = 10^3$ and negatively displaced when $Pe = 10^{-3}$. As shown in section 4.2.3, for the same X, E and Ca_{mag}, the droplet shape does not change with Pe. Thus, our results show that in such cases, the reduced viscosity is closely linked with the surfactant distribution over the droplet surface, such that $[\eta]$ increases as the surfactant concentration becomes less uniform. In other words, $[\eta]$ becomes a stronger function of $[\eta_m]$ as Ca_{mag} increases, because $[\eta_c]$ and $[\eta_{mag}]$ are stronger functions of the droplet shape, which does not change with Pe. Figure 36(b) shows that the magnetic field negatively displaces the curves $[\eta] \times X$, but without changing its patterns. Note that the differences between the curves from $Ca_{mag} = 0$ to $Ca_{mag} = 5$ are greater than those between $Ca_{mag} = 5$ to $Ca_{mag} = 10$, showing that, as Ca_{mag} increases, the viscosities become less sensitive to these variations, as the droplet assumes a shape that, in addition to offering low resistance to the flow, leaves it in a channel region where there is no effective $\dot{\gamma}$ to promote surfactant transportation.

4.2.4.5 Shear and rotational viscosities

Figures 37 and 38 present, respectively, the shear and rotational viscosities in their reduced form, as functions of X under (a) perpendicular and (b) parallel external field, for $E = 0.2$, $Ca_{mag} = 0$ $(+)$, $Ca_{mag} = 5$ $(\times)$ and $Ca_{mag} = 10$ $(*)$.

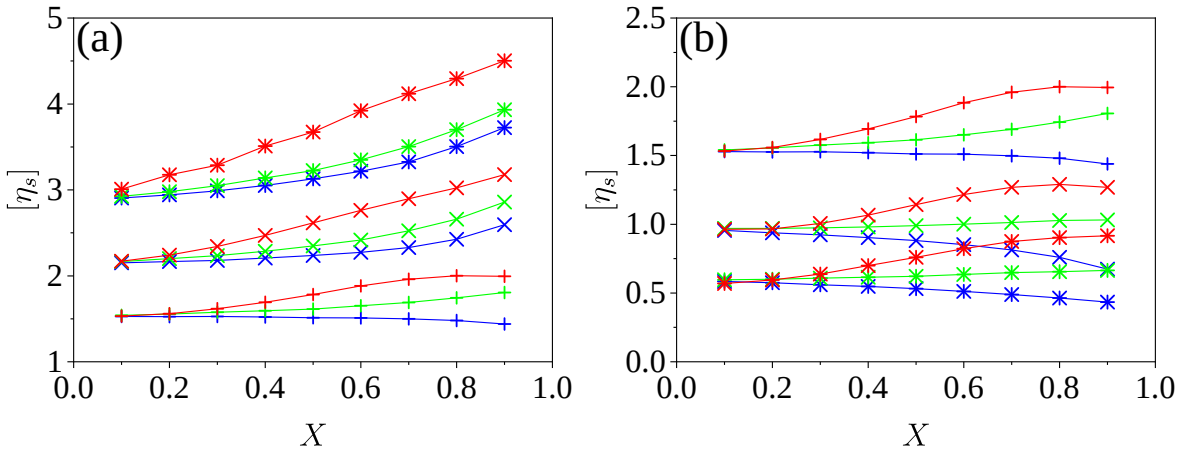

Figure 37 – Shear viscosity as functions of surfactant coverage, X, for $Pe = 10^3$ (red), $Pe = 1$ (green), and $Pe = 10^{-3}$ (blue) when $E = 0.2$, $Ca_{mag} = 0$ $(+)$, $Ca_{mag} = 5$ $(\times)$ and $Ca_{mag} = 10$ $(*)$. (a) and (b) correspond to perpendicular and parallel external magnetic field, respectively.

When the external field is perpendicular to the flow, $[\eta_s]$ and $[\eta_r]$ continuously increase with X and both have positive values [Figures 37(a) and 38(a)]. This is due to both the increase of the droplet deformation and Marangoni stresses. Increasing Ca_{mag} causes a positive displacement of the $[\eta_s]$ and $[\eta_r]$ curves, which is linked to the increase of D_T and θ, that is, it is closely related to the droplet length projected in the perpendicular

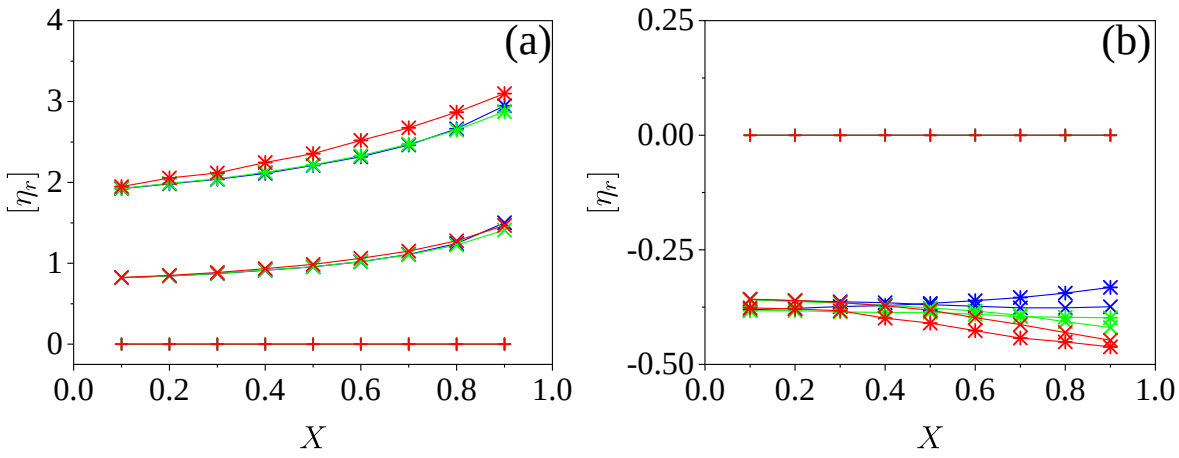

Figure 38 – Rotational viscosity as functions of surfactant coverage, X, for $Pe = 10^3$ (red), $Pe = 1$ (green), and $Pe = 10^{-3}$ (blue) when $E = 0.2$, $Ca_{mag} = 0$ (+), $Ca_{mag} = 5$ (×) and $Ca_{mag} = 10$ (∗). (a) and (b) correspond to perpendicular and parallel external magnetic field, respectively.

direction to the main flow. Increasing Pe positively displaces the curves of $[\eta_s]$ as X increases. This is due to the increase of Marangoni forces that occurs near the droplet tips, as shown in the 4.2.2 section. As these forces act in the opposite direction to the shear flow, the greater D_T and θ (which occurs when Ca_{mag} increases), the greater the effect of this resistance, and therefore, the greater $[\eta_s]$. On the other hand, the surfactant distribution along the droplet surface has a small (or no) effect on $[\eta_r]$. When $Ca_{mag} = 10$, there is a small positive displacement of the $[\eta_r]$ curves, which may be related to the small variations of the droplet shape when Pe and Ca_{mag} are sufficiently large.

The phenomena are remarkably different when the external field is parallel. The droplet deformation and alignment in the direction of flow causes less distortion in streamlines as the magnetic force increases. In fact, what is observed in Figures 37(b) and 38(b) are smaller absolutes values of $[\eta_s]$ and $[\eta_r]$ than when the magnetic field is perpendicular. Besides, can be seen that $[\eta_s]$ decreases with the intensity of the magnetic field, following the same trend as the reduced viscosity of the emulsion itself. This can be explained by the decrease of capillary and Marangoni stress, as already presented in section 4.2.4. In addition, as in Figure 37(a), increasing Pe also causes a positive displacement in the curves of $[\eta_s]$. However, this displacement is smaller than when the magnetic field is perpendicular since the droplet shape variations are smaller.

In turn, negative values of $[\eta_r]$ indicate that the internal magnetic torque tends to rotate the droplet along with the vorticity, becoming more pronounced as Pe increases. This increase of the absolute value of $[\eta_r]$ with Pe when X increases is a function of the projected droplet length decrease in the perpendicular direction to the flow, which decreases as the droplet is elongated in the flow direction.

Comparing Figures 38(a) and (b) with insets of Figures 33(a) and 34(a), respectively, it can be seen that the results of $[\eta_r]$ and $[\eta_{mag}]$ have the same behavior, although,

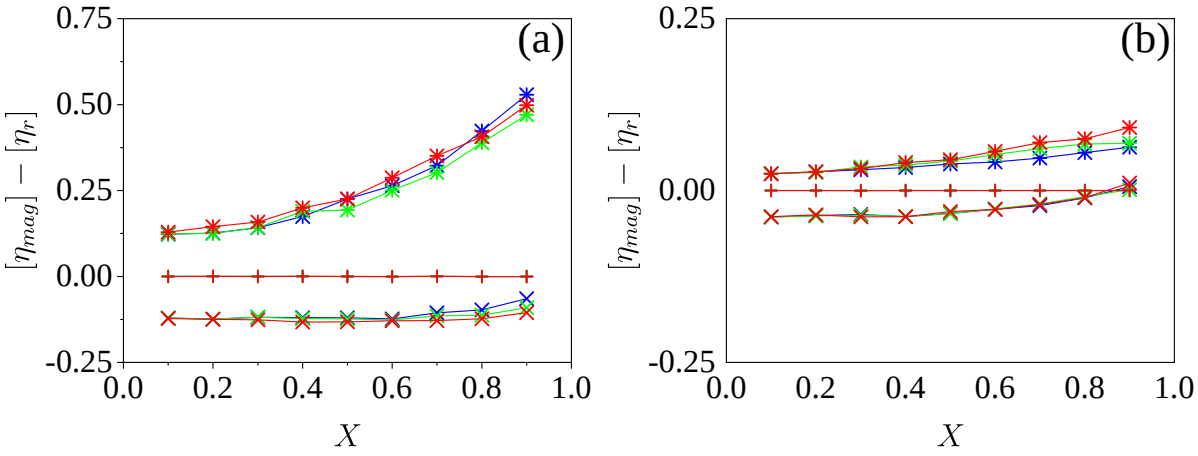

Figure 39 – Difference between magnetic and rotational viscosities as functions of surfactant coverage, X, for $Pe = 10^3$ (red), $Pe = 1$ (green), and $Pe = 10^{-3}$ (blue) when $E = 0.2$, $Ca_{mag} = 0$ (+), $Ca_{mag} = 5$ ($\times$) and $Ca_{mag} = 10$ ($*$). (a) and (b) correspond to perpendicular and parallel external magnetic field, respectively.

$[\eta_r] \neq [\eta_{mag}]$. Figure 39 shows $[\eta_{mag}] - [\eta_r]$ as functions of X at the same conditions of Figure 38. Note that the differences between magnetic and rotational viscosities are a function of surfactant coverage and magnetic field force, being more pronounced when the magnetic field is perpendicular to the main flow direction. Note in Figure 38, that in the absence of a magnetic field (symbols +) the surfactant does not affect $[\eta_r]$, that as $[\eta_{mag}]$ (see section 4.2.4.3) is equal to zero. Under these conditions $[\eta] = [\eta_s] = [\eta_c] + [\eta_m]$. The presence of the magnetic field invalidates this relationship, as the surfactant affects both the antisymmetric part and the symmetric part of the tensor stress, i. e., $[\eta_r] \neq [\eta_{mag}]$ and $[\eta_s] \neq [\eta_c] + [\eta_m]$.

Note in Figure 39 that $[\eta_{mag}] - [\eta_r]$ is not a function of Pe, so Marangoni stresses have no effect on $[\eta_r]$. This becomes clearer recalling the Figures insets 29(a) and 30(a), where for $Pe = 0$ the Marangoni stress and $[\eta_m]$ tend to zero. If the differences between $[\eta_{mag}]$ and $[\eta_r]$ were due to Marangoni stresses, the blue curves ($Pe = 0$) of Figure 39 should be coincident with the curves of $Ca_{mag} = 0$. However, there is an overlap of curves for different Pe, evidencing that the surfactant effects on the antisymmetric part of the stress tensor are due to the normal stresses at the interface.

Generally, $[\eta_r]$ decreases with respect to $[\eta_{mag}]$ is the extent to which X increases. There is the critical Ca_{mag} (called $Ca_{mag,s}$) above which $[\eta_r]$ is always smaller than $[\eta_{mag}]$, and another (called $Ca_{mag,i}$) below which $[\eta_r]$ is always bigger than $[\eta_{mag}]$. Between $Ca_{mag,i}$ and $Ca_{mag,s}$, $[\eta_r]$ is greater than $[\eta_{mag}]$ for small coverage factors and this reverses as that X increases, indicating the existence of a critical X when $Ca_{mag,i} < Ca_{mag} < Ca_{mag,s}$, where $[\eta_r] = [\eta_{mag}]$. However, even knowing that $[\eta_s] + [\eta_r] = [\eta_m] + [\eta_c] + [\eta_{mag}]$, the only relationship that can be established is that $[\eta_m]$ is implicit in $[\eta_s]$. In other cases, the relationships between $[\eta_s]$ or $[\eta_r]$ with $[\eta_c] + [\eta_{mag}]$ are unknown and may be a good subject for future work.

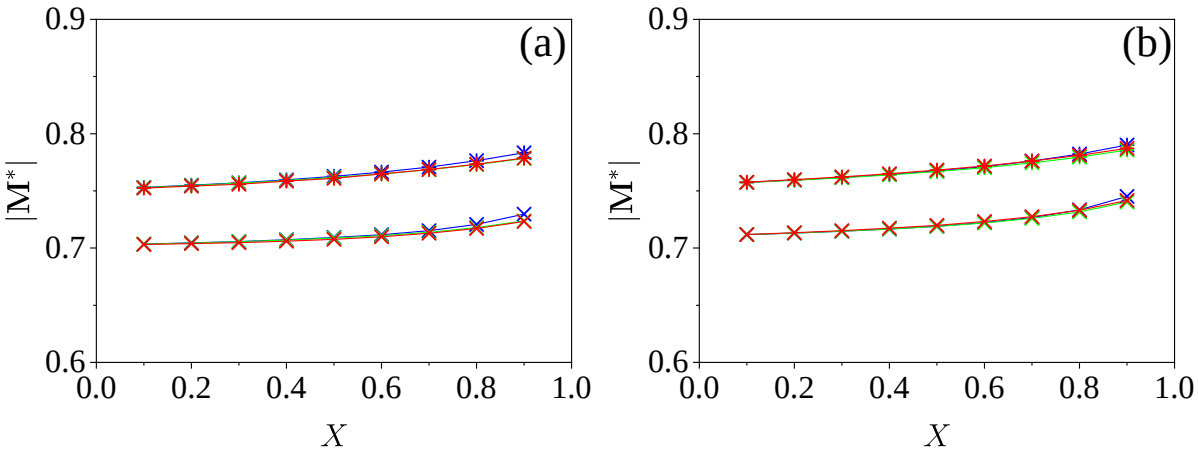

Figure 40 – Magnetization as function of surfactant coverage, X, for $Pe = 10^3$ (red), $Pe = 1$ (green), and $Pe = 10^{-3}$ (blue) when $E = 0.2$, $Ca_{mag} = 0$ $(+)$, $Ca_{mag} = 5$ $(\times)$ and $Ca_{mag} = 10$ $(*)$. (a) and (b) correspond to perpendicular and parallel external magnetic field, respectively.

4.2.5 Combined effect of surfactant and magnetic field on the emulsion magnetization

In this section, we present a complementary analysis to the work of Cunha et al. (2020), who performed a numerical investigation of the configuration and magnetization of the suspended ferrofluid droplet as a function of the intensity and direction of the external magnetic field. Here, the surfactant effects are also considered. The results are displayed as functions of X, for $E = 0.2$, $Ca_{mag} = 0$ $(+)$, $Ca_{mag} = 5$ $(\times)$ and $Ca_{mag} = 10$ $(*)$.

Figures 40 and 41 show the magnetization and magnetic torque, respectively, when the droplet is subjected to (a) perpendicular and (b) parallel external magnetic field. The insets of Figure 40 show the misalignment angle between the bulk magnetization and the external field. Note that the presence of the surfactant has a weak effect on magnetization. The curve $|\mathbf{M}^*| \times X$ is slightly upward, making it clear that, as shown by Cunha et al. (2020), $|\mathbf{M}^*|$ depends on its length projected in the direction of the external field. In both directions of the external field, D_T tends to increase while θ tends to decrease as X increases, however, the variations are smaller than in the absence of a magnetic field. Thus, small variations of the droplet shape over the range of X result in small variations of $|\mathbf{M}^*|$. Finally, as expected, increasing the field intensity positively displaces the curves of $|\mathbf{M}^*|$.

On the other hand, the internal torques do not have the same behavior. When the magnetic field is perpendicular, Figure 41(a) shows that the increase of X results in an increasing magnitude of τ^*_{mag} (The negative value indicates just the torque direction, which in this case is opposite to the shear flow). This can be explained using the inset of Figure 41(a), where the misalignment angle between the bulk magnetization and the vertical external field increases with X due to the increasing of droplet deformation, which increases the shear flow effects, tending to bend the droplet in the x-direction. Under

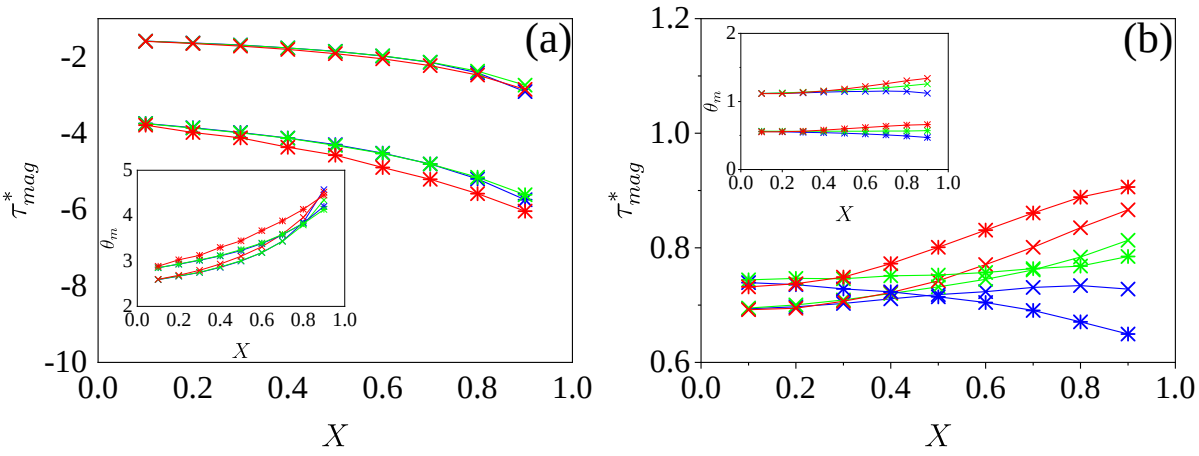

Figure 41 – Magnetic torque as function of surfactant coverage, X, for $Pe = 10^3$ (red), $Pe = 1$ (green), and $Pe = 10^{-3}$ (blue) when $E = 0.2$, $Ca_{mag} = 0$ (+), $Ca_{mag} = 5$ ($\times$) and $Ca_{mag} = 10$ ($*$). (a) and (b) correspond to perpendicular and parallel external magnetic field, respectively. The insets show the misalignment angle as function of X.

these conditions, the internal torque, τ^*_{mag}, that tends to rotate the droplet in the field direction, has its magnitude increased as X increases. When the magnetic field is parallel [Figure 41(b)], both the magnetic field and the shear flow tend to align the droplet in the flow direction, therefore, the increase of X has a small effect on θ_m [inset of Figure 41(b)] and, consequently, on τ^*_{mag}. In this case, the relationship between advection and surfactant diffusion changes the pattern of the curves from τ^*_{mag} as X increases, making them ascend for $Pe \geq 1$. This can be explained by the relationship between Marangoni forces and internal torques, because when the magnetic field is parallel to the flow, the internal torques are small, making the Marangoni stress effects evident. On the other hand, when the magnetic field is perpendicular, the Marangoni forces are relatively small compared to the internal torques, so changes in Pe have a small effect on τ^*_{mag}.

5 Conclusions

We presented a computational study on the combined effects of surfactant coverage, elasticity, Péclet number, and magnetic field on the dynamics of surfactant-covered ferrofluid droplets, the rheology of dilute emulsions in simple shear flow and the mean magnetization of this system. The continuum model was solved by combining the level set method to capture the evolution of the interface and the closest point method to solve the surfactant concentration equation on the surface. We presented a formulation for the stress tensor separating the stresslet into capillary, Marangoni, and magnetic stresses. Based on these stress tensors, we defined the capillary, Marangoni, and magnetic viscosities, which summed, return the convectional reduced viscosity. Finally, we explored the rheology of this non-symmetric complex fluid in terms of the shear viscosity and rotational viscosities.

In the absence of a magnetic field, our results indicate that droplet shape is more affected by the elasticity and coverage than by the Péclet number. On the other hand, the Péclet number is decisive for the rheology in such a manner that emulsions of droplets of the same shape present remarkably distinct reduced viscosity. The definition of the capillary and Marangoni viscosity helped us understand the mechanisms in the droplet scale responsible for the bulk viscosity variations, under surfactant related parameter changes. An increase of E or X leads to higher deformation, regardless of the Pe, as a consequence of the reduction of the surface tension. However, the reduced viscosity can either increase or decrease as a function of E and X, depending on Pe, due to the more complex relation between the Marangoni and capillary viscosity, under different elasticity and coverage. Our results also indicate that, for dilute emulsions, the surfactant cannot change the signal of the first normal stress difference.

The presence of the magnetic field has a direct effect on the observations in the previous paragraph. Its action directly affects the surfactant accumulation regions, sweeping it to a posterior or anterior region to the droplet tips, respectively, when the field is perpendicular or parallel. These effects are more evident when the magnetic field is perpendicular, where the Marangoni force peaks increase with Ca_{mag}, opposite to when the magnetic field is parallel. The increase in the intensity of the external field increases the strain, and decreases or increases the droplet inclination, respectively, when applied in the direction parallel or perpendicular to the main flow, but does not change the behavior of these quantities with relation to X. As a general rule, the droplet shape is a stronger

function of Ca_{mag} than of X and E.

For $Pe \geq 1$ $[\eta_m]$ increases with X and decreases with Ca_{mag} when the field is parallel and increases with X and Ca_{mag} when the magnetic field is perpendicular. In this latter, the droplet surface locations where $\mathbf{F}_m \cdot \hat{\mathbf{t}} > 0$ are in a flow region in which the local shear rate is greater than those locations in which the parallel magnetic field moves these regions. Since $\mathbf{F}_m \cdot \hat{\mathbf{t}} > 0$ acts to resist yielding, η_m increases. The behavior is opposite when Ca_{mag} increases under perpendicular and parallel fields. On the other hand, when $Pe \ll 1$, the surfactant tends to be uniformly distributed, and the Marangoni viscosity always tends to zero. Thus, we can conclude that the Marangoni viscosity is a stronger function of Pe than of Ca_{mag}, X, or E.

The capillary viscosity is a function of the competition between surfactant advection and droplet deformation (or σ and κ). A greater amount of surfactant is swept near the droplet tips as Pe increases, reducing $|\mathbf{F}_c \cdot \hat{\mathbf{n}}|$ in these regions. In turn, the magnetic field action increases the droplet deformation, reducing and increasing κ, in regions of lower and higher surfactant concentration, respectively. Under a perpendicular field, it is possible to divide the droplet into two regions as Ca_{mag} increases: one in which the local shear rate is smaller, κ decreases (longer droplet portion) and σ increases (due to the surfactant being swept to the droplet tips); and another in which the local shear rate is higher, κ increases (droplet tips) and σ decreases by surfactant accumulation. The balance of this antagonistic behavior is what determines $[\eta_c]$. If the magnetic field is parallel, the local shear rate is not enough to cause the same variations in the surfactant concentration and, consequently, in the surface tension coefficient, even if the advective effects are large. Thus, $|\mathbf{F}_c \cdot \hat{\mathbf{n}}|$ becomes a stronger function of curvature than of σ. In turn, the magnetic viscosity contributes to decreasing or increasing the emulsion reduced viscosity when the magnetic field is parallel or perpendicular, respectively. The magnetic viscosity is independent of the surfactant distribution on the droplet surface, being the quasi-exclusive function of D_T. Thus, the reduced viscosity $[\eta]$ can be defined as the sum of $[\eta_c]$, $[\eta_m]$, and $[\eta_{mag}]$. So, its variations can be analyzed in terms of these components.

Another way of defining viscosity is the sum of $[\eta_s]$ and $[\eta_r]$. These viscosities parcels are functions of the symmetric and antisymmetric parts of the stress tensor, respectively. In general, we find that $[\eta_s]$ is a stronger function of $[\eta_c]$ and $[\eta_m]$, regardless of the direction and magnetic field intensity. In the absence of a magnetic field ($Ca_{mag} = 0$), the surfactant does not affect η_r, which is equal to $[\eta_{mag} = 0]$. The magnetic field action "set" the surfactant effects on $[\eta_r]$. However $[\eta_r]$ is not a function of Pe, that is, $[\eta_m]$ is implicit in $[\eta_s]$, indicating that the surfactant effects on $[\eta_r]$ are due to the normal stresses. Finally, it should be noted that although they have the same pattern, $[\eta_r] \neq [\eta_m]$ and $[\eta_s] \neq [\eta_{mag}] + [\eta_m]$.

Regarding the system mean magnetization, $|\mathbf{M}^*|$ is a stronger function of the length projected in the direction of the external field, where the variations along of X range are due to the droplet shape. The magnitude of the magnetic torque increases with X when

the magnetic field is perpendicular due to the increase of misalignment angle, increasing the shear flow effects. When the field is parallel, both the magnetic field and the shear flow tend to align the droplet in the direction of the flow, and therefore, X has a small effect on θ_m and τ^*_{mag}.

The present work showed innovative contributions to the understanding of the effects of surfactant and magnetic field in the rheology of ferrofluid droplet emulsions in shear flows. In addition, the new methodology presented was efficient for simulating the dynamics of surfactant-covered ferrofluid droplets under shear flow.

Bibliography

ABICALIL, V.; ABDO, R.; CUNHA, L. D.; OLIVEIRA, T. D. On the magnetization of dilute ferrofluid emulsions in shear flows. *Physics of Fluids*, v. 33, n. 5, 2021.

ABICALIL, V. G. *Rheology and magnetization of dilute ferrofluid emulsions*. Dissertação (M.S. thesis) — University of Brasília, "Department of Mechanical Engineering (ENM) - FT, august 2021.

AHMED, A.; FLECK, B. A.; WAGHMARE, P. R. Maximum spreading of a ferrofluid droplet under the effect of magnetic field. *Physics of Fluids*, v. 30, n. 7, p. 077102, 2018. ISSN 10897666.

BATCHELOR, G. The stress system in a suspension of force-free particles. *Journal of fluid mechanics*, v. 41, p. 545, 1970.

BAZHLEKOV, I.; ANDERSON, P.; MEIJER, H. Numerical investigation of the effect of insoluble surfactants on drop deformation and breakup in simple shear flow. *Journal of Colloid and Interface Science*, v. 298, n. 1, p. 369–394, 2006.

BEAUCOURT, J.; RIOUAL, F.; SéON, T.; BIBEN, T.; MISBAH, C. Steady to unsteady dynamics of a vesicle in a flow. *Physical Review E*, v. 69, n. 1, p. 17, 2004.

BLAWZDZIEWICZ, J.; VLAHOVSKA, P.; LOEWENBERG, M. Rheology of a dilute emulsion of surfactant-covered spherical drops. *Physica A: Statistical Mechanics and its Applications*, v. 276, n. 1, p. 50–85, 2000.

BRADY, J. F.; BOSSIS, G. Stokesian dynamics. *Annual review of fluid mechanics*, Annual Reviews 4139 El Camino Way, PO Box 10139, Palo Alto, CA 94303-0139, USA, v. 20, n. 1, p. 111–157, 1988.

CAPOBIANCHI, P.; LAPPA, M.; OLIVEIRA, M. S. Deformation of a ferrofluid droplet in a simple shear flow under the effect of a constant magnetic field. *Computers and Fluids*, Elsevier Ltd, v. 173, p. 313–323, 2018. ISSN 00457930.

CHANDRASEKHARAIAH, D. S.; DEBNATH, L. *Continuum Mechanics*. London: Academic Press, 1994.

CUNHA, L. H.; SIQUEIRA, I. R.; CUNHA, F. R.; OLIVEIRA, T. F. Effects of external magnetic fields on the rheology and magnetization of dilute emulsions of ferrofluid droplets in shear flows. *Physics of Fluids*, AIP Publishing, LLC, v. 32, n. 7, p. 073306, 2020. ISSN 10897666.

CUNHA, L. H.; SIQUEIRA, I. R.; OLIVEIRA, T. F.; CENICEROS, H. D. Field-induced control of ferrofluid emulsion rheology and droplet break-up in shear flows. *Physics of Fluids*, v. 30, n. 12, p. 122110, 2018. ISSN 10897666.

DANDEKAR, R.; ARDEKANI, A. Effect of interfacial viscosities on droplet migration at low surfactant concentrations. *Journal of Fluid Mechanics*, v. 902, 2020.

DAS, S.; BHATTACHARJEE, A.; CHAKRABORTY, S. Influence of interfacial slip on the suspension rheology of a dilute emulsion of surfactant-laden deformable drops in linear flows. *Physics of Fluids*, v. 30, n. 3, 2018.

DAS, S.; CHAKRABORTY, S. Influence of complex interfacial rheology on the thermocapillary migration of a surfactant-laden droplet in poiseuille flow. *Physics of Fluids*, v. 30, n. 2, 2018.

DAS, S.; MANDA, S.; CHAKRABORTY, S. Cross-stream migration of a surfactant-laden deformable droplet in a poiseuille flow. *Physics of Fluids*, v. 29, n. 8, p. 082004, 2017.

DAS, S.; MANDAL, S.; SOM, S.; CHAKRABORTY, S. Migration of a surfactant-laden droplet in non-isothermal poiseuille flow. *Physics of Fluids*, v. 29, n. 1, p. 012002, 2017.

DRUMRIGHT-CLARKE, M. A.; RENARDY, Y. The effect of insoluble surfactant at dilute concentratiion on drop breakup under shear with inertia. *Physics of Fluids*, v. 16, n. 1, p. 14–21, 2004. ISSN 10706631.

EGGLETON, C.; TSAI, T.-M.; STEBE, K. Tip streaming from a drop in the presence of surfactants. *Physical Review Letters*, v. 87, n. 4, p. 48302–1–48302–4, 2001.

FEIGL, K.; MEGIAS-ALGUACIL, D.; FISCHER, P.; WINDHAB, E. Simulation and experiments of droplet deformation and orientation in simple shear flow with surfactants. *Chemical Engineering Science*, v. 62, n. 12, p. 3242–3258, 2007.

FOSS, D.; BRADY, J. Structure, diffusion and rheology of brownian suspensions by stokesian dynamics simulation. *Journal of Fluid Mechanics*, v. 407, p. 167–200, 2000.

GHIGLIOTTI, G.; BIBEN, T.; MISBAH, C. Rheology of a dilute two-dimensional suspension of vesicles. *Journal of Fluid Mechanics*, v. 653, p. 489–518, 2010.

GUO, K.; LV, Y.; HE, L.; LUO, X.; YANG, D. Separation Characteristics of Water-in-Oil Emulsion under the Coupling of Electric Field and Magnetic Field. *Energy and Fuels*, American Chemical Society, v. 33, n. 3, p. 2565–2574, 2019. ISSN 15205029.

HASSAN, M. R.; WANG, C. Magnetic field induced ferrofluid droplet breakup in a simple shear flow at a low Reynolds number. *Physics of Fluids*, AIP Publishing, LLC, v. 31, n. 12, 2019. ISSN 10897666.

HASSAN, M. R.; WANG, C. Lateral migration of a ferrofluid droplet in a plane Poiseuille flow under uniform magnetic fields. *Physical Review E*, American Physical Society, v. 102, n. 2, p. 1–15, 2020. ISSN 24700053.

HASSAN, M. R.; ZHANG, J.; WANG, C. Deformation of a ferrofluid droplet in simple shear flows under uniform magnetic fields. *Physics of Fluids*, v. 30, n. 9, p. 092002, 2018. ISSN 10897666.

HEDAYATI, N.; RAMIAR, A.; LARIMI, M. M. Investigating the effect of external uniform magnetic field and temperature gradient on the uniformity of nanoparticles in drug delivery applications. *Journal of Molecular Liquids*, Elsevier B.V., v. 272, p. 301–312, 2018. ISSN 01677322.

HELFRICH, W. Elastic properties of lipid bilayers: Theory and possible experiments. *Zeitschrift fur Naturforschung - Section C Journal of Biosciences*, v. 28, n. 11-12, p. 693–703, 1973.

HILL, R.; AFUWAPE, G. Dynamic mobility of surfactant-stabilized nano-drops: Unifying equilibrium thermodynamics, electrokinetics and marangoni effects. *Journal of Fluid Mechanics*, v. 895, 2020.

HIRT, C.; NICHOLS, B. Volume of fluid (vof) method for the dynamics of free boundaries. *Journal of Computational Physics*, v. 39, n. 1, p. 201–225, 1981.

HSU, S. H.; CHU, J.; LAI, M. C.; TSAI, R. A coupled grid based particle and implicit boundary integral method for two-phase flows with insoluble surfactant. *Journal of Computational Physics*, Elsevier Inc., v. 395, p. 747–764, 2019. ISSN 10902716.

ISHIDA, S.; MATSUNAGA, D. Rheology of a dilute ferrofluid droplet suspension in shear flow: Viscosity and normal stress differences. *Physical Review Fluids*, American Physical Society, v. 5, n. 12, p. 1–17, 2020. ISSN 2469990X.

JALILI DARBANDI SOFLA, M.; NOROUZI-APOURVARI, S.; SCHAFFIE, M. The effect of magnetic field on stability of conventional and pickering water-in-crude oil emulsions stabilized with fumed silica and iron oxide nanoparticles. *Journal of Molecular Liquids*, Elsevier B.V., v. 314, p. 113629, 2020. ISSN 01677322.

JAMES, A. J.; LOWENGRUB, J. A surfactant-conserving volume-of-fluid method for interfacial flows with insoluble surfactant. *Journal of Computational Physics*, v. 201, n. 2, p. 685–722, 2004. ISSN 00219991.

JESUS, W. C.; ROMA, A. M.; CENICEROS, H. D. Deformation of a Sheared Magnetic Droplet in a Viscous Fluid. *Communications in Computational Physics*, v. 24, n. 2, p. 1–26, 2018. ISSN 18152406.

JESUS, W. de; ROMA, A.; PIVELLO, M.; VILLAR, M.; SILVEIRA-NETO, A. da. A 3d front-tracking approach for simulation of a two-phase fluid with insoluble surfactant. *Journal of Computational Physics*, v. 281, p. 403–420, 2015.

JO, Y.; AHN, H.; SHIN, K.; LEE, H. Effects of pulsed magnetic field on the flowing red blood cells using microvascular model. *IEEE Transactions on Magnetics*, IEEE, v. 54, n. 11, p. 1–3, 2018. ISSN 00189464.

KAOUI, B.; RISTOW, G.; CANTAT, I.; MISBAH, C.; ZIMMERMANN, W. Lateral migration of a two-dimensional vesicle in unbounded poiseuille flow. *Physical Review E - Statistical, Nonlinear, and Soft Matter Physics*, v. 77, n. 2, 2008.

KENNEDY, M.; POZRIKIDIS, C.; SKALAK, R. Motion and deformation of liquid drops, and the rheology of dilute emulsions in simple shear flow. *Computers and Fluids*, v. 23, n. 2, p. 251–278, 1994.

KRUIJT-STEGEMAN, Y.; VOSSE, F. van de; MEIJER, H. Droplet behavior in the presence of insoluble surfactants. *Physics of Fluids*, v. 16, n. 8, p. 2785–2796, 2004.

LAI, M.-C.; TSENG, Y.-H.; HUANG, H. An immersed boundary method for interfacial flows with insoluble surfactant. *Journal of Computational Physics*, v. 227, n. 15, p. 7279–7293, 2008.

LANGAVANT, C. Cleret de; GUITTET, A.; THEILLARD, M.; TEMPRANO-COLETO, F.; GIBOU, F. Level-set simulations of soluble surfactant driven flows. *Journal of Computational Physics*, v. 348, p. 271–297, 2017.

LI, S.; ZHANG, R.; WANG, D.; FENG, L.; CUI, K. Synthesis of hollow maghemite (<gamma>-Fe2O3) particles for magnetic field and pH-responsive drug delivery and lung cancer treatment. *Ceramics International*, Elsevier Ltd, v. 47, n. 6, p. 7457–7464, 2021. ISSN 02728842.

LI, X.; POZRIKIDIS, C. The effect of surfactants on drop deformation and on the rheology of dilute emulsions in stokes flow. *Journal of Fluid Mechanics*, v. 341, p. 165–194, 1997.

LI, Z.; ITO, K. *The immersed interface method: numerical solutions of PDEs involving interfaces and irregular domains*. [S.l.]: SIAM, 2006.

LIU, H.; BA, Y.; WU, L.; LI, Z.; XI, G.; ZHANG, Y. A hybrid lattice Boltzmann and finite difference method for droplet dynamics with insoluble surfactants. *Journal of Fluid Mechanics*, v. 837, p. 381–412, 2018. ISSN 14697645.

LIU, H.; ZHANG, J.; BA, Y.; WANG, N.; WU, L. Modelling a surfactant-covered droplet on a solid surface in three-dimensional shear flow. *Journal of Fluid Mechanics*, 2020.

LIU, H.; ZHANG, Y. Phase-field modeling droplet dynamics with soluble surfactants. *Journal of Computational Physics*, v. 229, n. 24, p. 9166–9187, 2010.

LU, J.; MURADOGLU, M.; TRYGGVASON, G. Effect of insoluble surfactant on turbulent bubbly flows in vertical channels. *International Journal of Multiphase Flow*, Elsevier Ltd, v. 95, p. 135–143, 2017. ISSN 03019322.

LUO, X.; LUO, Z. Y.; BAI, B. F. Effect of thermal convection on thermocapillary migration of a surfactant-laden droplet in a microchannel. *Physics of Fluids*, AIP Publishing, LLC, v. 32, n. 9, 2020. ISSN 10897666.

LUO, Z.; SHANG, X.; BAI, B. Marangoni effect on the motion of a droplet covered with insoluble surfactant in a square microchannel. *Physics of Fluids*, v. 30, n. 7, 2018.

LUO, Z. Y.; SHANG, X. L.; BAI, B. F. Influence of pressure-dependent surface viscosity on dynamics of surfactant-laden drops in shear flow. *Journal of Fluid Mechanics*, v. 858, p. 91–121, 2019. ISSN 14697645.

MACDONALD, C. B.; RUUTH, S. J. The implicit closest point method for the numerical solution of partial differential equations on surfaces. *SIAM Journal on Scientific Computing*, SIAM, v. 31, n. 6, p. 4330–4350, 2010.

MANDAL, S.; BANDOPADHYAY, A.; CHAKRABORTY, S. Dielectrophoresis of a surfactant-laden viscous drop. *Physics of Fluids*, v. 28, n. 6, 2016.

MANDAL, S.; DAS, S.; CHAKRABORTY, S. Effect of marangoni stress on the bulk rheology of a dilute emulsion of surfactant-laden deformable droplets in linear flows. *Physical Review Fluids*, v. 2, n. 11, 2017.

MARTÍNEZ-SANTIAGO, C. J.; QUIÑONES, E. On matching the magnetic torque exerted by a rotating magnetic field to the torsional stiffness of braided DNA molecules for torque estimations. *Chemical Physics*, Elsevier, v. 519, n. November 2018, p. 74–84, 2019. ISSN 03010104.

MILLIKEN, W.; STONE, H.; LEAL, L. The effect of surfactant on the transient motion of newtonian drops. *Physics of Fluids A*, v. 5, n. 1, p. 69–79, 1992.

MONDAL, A.; SHIT, G. C. Transport of magneto-nanoparticles during electro-osmotic flow in a micro-tube in the presence of magnetic field for drug delivery application. *Journal of Magnetism and Magnetic Materials*, Elsevier B.V., v. 442, p. 319–328, 2017. ISSN 03048853.

MURADOGLU, M.; TRYGGVASON, G. A front-tracking method for computation of interfacial flows with soluble surfactants. *Journal of Computational Physics*, v. 227, n. 4, p. 2238–2262, 2008.

MURADOGLU, M.; TRYGGVASON, G. Simulations of soluble surfactants in 3D multiphase flow. *Journal of Computational Physics*, Elsevier Inc., v. 274, p. 737–757, 2014. ISSN 10902716.

OLIVEIRA, T.; CUNHA, F. Emulsion rheology for steady and oscillatory shear flows at moderate and high viscosity ratio. *Rheologica Acta*, v. 54, n. 11-12, p. 951–971, 2015.

OSHER, S.; FEDKIW, R. Level set methods and dynamic implicit surfaces. In: _____. New York: Springer, 2003. v. 153, p. 31–33.

OSHER, S.; SETHIAN, J. Fronts propagating with curvature-dependent speed: Algorithms based on hamilton-jacobi formulations. *Journal of Computational Physics*, v. 79, n. 1, p. 12–49, 1988.

PÅLSSON, S.; SIEGEL, M.; TORNBERG, A. K. Simulation and validation of surfactant-laden drops in two-dimensional Stokes flow. *Journal of Computational Physics*, Elsevier Inc., v. 386, p. 218–247, 2019. ISSN 10902716.

PANIGRAHI, D.; DAS, S.; CHAKRABORTY, S. Deformation of a surfactant-laden viscoelastic droplet in a uniaxial extensional flow. *Physics of Fluids*, v. 30, n. 12, 2018.

PANIGRAHI, D.; SANTRA, S.; BANUPRASAD, T.; DAS, S.; CHAKRABORTY, S. Interfacial viscosity-induced suppression of lateral migration of a surfactant laden droplet in a nonisothermal poiseuille flow. *Physical Review Fluids*, v. 6, n. 5, 2021.

PENG, D.; MERRIMAN, B.; OSHER, S.; ZHAO, H.; KANG, M. A pde-based fast local level set method. *Journal of Computational Physics*, v. 155, n. 2, p. 410–438, 1999.

PETRAS, A.; LING, L.; PIRET, C.; RUUTH, S. A least-squares implicit rbf-fd closest point method and applications to pdes on moving surfaces. *Journal of Computational Physics*, v. 381, p. 146–161, 2019.

PETRAS, A.; RUUTH, S. Pdes on moving surfaces via the closest point method and a modified grid based particle method. *Journal of Computational Physics*, v. 312, p. 139–156, 2016.

PODDAR, A.; MANDAL, S.; BANDOPADHYAY, A.; CHAKRABORTY, S. Sedimentation of a surfactant-laden drop under the influence of an electric field. *Journal of Fluid Mechanics*, v. 849, p. 277–311, 2018.

PODDAR, A.; MANDAL, S.; BANDOPADHYAY, A.; CHAKRABORTY, S. Electrorheology of a dilute emulsion of surfactant-covered drops. *Journal of Fluid Mechanics*, v. 881, p. 524–550, 2019.

PONCE-TORRES, A.; MONTANERO, J.; HERRADA, M.; VEGA, E.; VEGA, J. Influence of the surface viscosity on the breakup of a surfactant-laden drop. *Physical Review Letters*, v. 118, n. 2, 2017.

ROMANOVA, Y. N.; MARYUTINA, T.; MUSINA, N. S.; YURTOV, E. V.; SPIVAKOV, B. Y. Demulsification of water-in-oil emulsions by exposure to magnetic field. *Journal of Petroleum Science and Engineering*, Elsevier B.V., v. 179, n. May, p. 600–605, 2019. ISSN 09204105.

ROSENSWEIG, R. E. *Ferrohydrodynamics*. [S.l.]: Courier Corporation, 2013.

RUUTH, S.; MERRIMAN, B. A simple embedding method for solving partial differential equations on surfaces. *Journal of Computational Physics*, v. 227, n. 3, p. 1943–1961, 2008.

SALAC, D.; MIKSIS, M. A level set projection model of lipid vesicles in general flows. *Journal of Computational Physics*, v. 230, n. 22, p. 8192–8215, 2011.

SCHOWALTER, W.; CHAFFEY, C.; BRENNER, H. Rheological behavior of a dilute emulsion. *Journal of Colloid And Interface Science*, v. 26, n. 2, p. 152–160, 1968.

SHAIK, V.; VASANI, V.; ARDEKANI, A. Locomotion inside a surfactant-laden drop at low surface péclet numbers. *Journal of Fluid Mechanics*, v. 851, p. 187–230, 2018.

SHI, Y.; TANG, G. H.; CHENG, L. H.; SHUANG, H. Q. An improved phase-field-based lattice Boltzmann model for droplet dynamics with soluble surfactant. *Computers and Fluids*, Elsevier Ltd, v. 179, p. 508–520, 2019. ISSN 00457930.

SHU, C.-W.; OSHER, S. Efficient implementation of essentially non-oscillatory shock-capturing schemes. *Journal of Computational Physics*, v. 77, n. 2, p. 439–471, 1988.

SHYAM, S.; MONDAL, P. K.; MEHTA, B. Magnetofluidic mixing of a ferrofluid droplet under the influence of a time-dependent external field. *Journal of Fluid Mechanics*, v. 917, p. 1–29, 2021. ISSN 14697645.

SODAGAR, H.; SHAKIBA, A.; NIAZMAND, H. Numerical investigation of drug delivery by using magnetic field in a 90-degree bent vessel: a 3D simulation. *Biomechanics and Modeling in Mechanobiology*, Springer Berlin Heidelberg, v. 19, n. 6, p. 2255–2269, 2020. ISSN 16177940.

SODAGAR, H.; SODAGAR-ABARDEH, J.; SHAKIBA, A.; NIAZMAND, H. Numerical study of drug delivery through the 3D modeling of aortic arch in presence of a magnetic field. *Biomechanics and Modeling in Mechanobiology*, Springer Berlin Heidelberg, v. 20, n. 2, p. 787–802, 2021. ISSN 16177940.

SOLIGO, G.; ROCCON, A.; SOLDATI, A. Breakage, coalescence and size distribution of surfactant-laden droplets in turbulent flow. *Journal of Fluid Mechanics*, v. 881, p. 244–282, 2019. ISSN 14697645.

SOLIGO, G.; ROCCON, A.; SOLDATI, A. Coalescence of surfactant-laden drops by phase field method. *Journal of Computational Physics*, v. 376, p. 1292–1311, 2019.

SOLIGO, G.; ROCCON, A.; SOLDATI, A. Deformation of clean and surfactant-laden droplets in shear flow. *Meccanica*, v. 55, n. 2, p. 371–386, 2020.

SORGENTONE, C.; TORNBERG, A. K. A highly accurate boundary integral equation method for surfactant-laden drops in 3D. *Journal of Computational Physics*, Elsevier Inc., v. 360, p. 167–191, 2018. ISSN 10902716.

SORGENTONE, C.; TORNBERG, A. K.; VLAHOVSKA, P. M. A 3D boundary integral method for the electrohydrodynamics of surfactant-covered drops. *Journal of Computational Physics*, Elsevier Inc., v. 389, p. 111–127, 2019. ISSN 10902716.

SORGENTONE, C.; VLAHOVSKA, P. Pairwise interactions of surfactant-covered drops in a uniform electric field. *Physical Review Fluids*, v. 6, n. 5, 2021.

SRIVASTAVA, P.; MALIPEDDI, A.; SARKAR, K. Steady shear rheology of a viscous emulsion in the presence of finite inertia at moderate volume fractions: Sign reversal of normal stress differences. *Journal of Fluid Mechanics*, v. 805, p. 494–522, 2016.

STONE, H. A.; LEAL, L. G. The effects of surfactants on drop deformation and breakup. *Journal of Fluid Mechanics*, Cambridge University Press, v. 220, p. 161–186, 1990.

SUSSMAN, M. A level set approach for computing solutions to incompressible two-phase flow. *Journal of Computational Physics*, v. 114, n. 1, p. 146–159, 1994.

SUSSMAN, M.; FATEMI, E. Efficient, interface-preserving level set redistancing algorithm and its application to interfacial incompressible fluid flow. *SIAM Journal on Scientific Computing*, v. 20, n. 4, p. 1165–1191, 1999.

TAMBASCO, M.; PANG, G.; FULLER, L.; BRESCIA, E. L.; MARDIROSSIAN, G. Impact of a 1.5 T magnetic field on DNA damage in MRI-guided HDR brachytherapy. *Physica Medica*, Elsevier, v. 76, n. July, p. 85–91, 2020. ISSN 1724191X.

TAYLOR, G. I. The formation of emulsions in definable fields of flow. *Proceedings of the Royal Society of London. Series A, containing papers of a mathematical and physical character*, The Royal Society London, v. 146, n. 858, p. 501–523, 1934.

TITTA, A.; Le Merrer, M.; DETCHEVERRY, F.; SPELT, P. D.; BIANCE, A. L. Level-set simulations of a 2D topological rearrangement in a bubble assembly: Effects of surfactant properties. *Journal of Fluid Mechanics*, v. 838, p. 222–247, 2018. ISSN 14697645.

VLAHOVSKA, P.; BLAWZDZIEWICZ, J.; LOEWENBERG, M. Nonlinear rheology of a dilute emulsion of surfactant-covered spherical drops in time-dependent flows. *Journal of Fluid Mechanics*, v. 463, p. 1–24, 2002.

VOGL, C. The curvature-augmented closest point method with vesicle inextensibility application. *Journal of Computational Physics*, v. 345, p. 818–833, 2017.

VORST, H. A. Van der. Bi-cgstab: A fast and smoothly converging variant of bi-cg for the solution of nonsymmetric linear systems. *SIAM Journal on scientific and Statistical Computing*, SIAM, v. 13, n. 2, p. 631–644, 1992.

XU, J.-J.; LI, Z.; LOWENGRUB, J.; ZHAO, H. A level-set method for interfacial flows with surfactant. *Journal of Computational Physics*, v. 212, n. 2, p. 590–616, 2006.

XU, J. J.; REN, W. A level-set method for two-phase flows with moving contact line and insoluble surfactant. *Journal of Computational Physics*, Elsevier Inc., v. 263, p. 71–90, 2014. ISSN 10902716.

XU, J.-J.; SHI, W.; LAI, M.-C. A level-set method for two-phase flows with soluble surfactant. *Journal of Computational Physics*, v. 353, p. 336–355, 2018.

XU, J. J.; YANG, Y.; LOWENGRUB, J. A level-set continuum method for two-phase flows with insoluble surfactant. *Journal of Computational Physics*, Elsevier Inc., v. 231, n. 17, p. 5897–5909, 2012. ISSN 10902716.

XU, J.-J.; ZHAO, H.-K. An eulerian formulation for solving partial differential equations along a moving interface. *Journal of Scientific Computing*, v. 19, n. 1-3, p. 573–594, 2003.

ZHANG, J.; LIU, H.; ZHANG, X. Modeling the deformation of a surfactant-covered droplet under the combined influence of electric field and shear flow. *Physics of Fluids*, v. 33, n. 4, 2021.

ZHU, G.; KOU, J.; SUN, S.; YAO, J.; LI, A. Numerical approximation of a phase-field surfactant model with fluid flow. *Journal of Scientific Computing*, v. 80, n. 1, p. 223–247, 2019.

ZINCHENKO, A.; DAVIS, R. General rheology of highly concentrated emulsions with insoluble surfactant. *Journal of Fluid Mechanics*, v. 816, p. 661–704, 2017.

Appendix

A - Suggestion to future work: magnetic vesicles

Vesicle problems require the same numerical tools as the surfactant-covered droplets. However, it is necessary to use a projection method at the interface to determine the surface tension. From this point of view, as it is simpler, the methodology behind the simulations performed in this work is an ideal starting point for the development of a consistent methodology for the study of magnetic vesicle dynamics. The main advantage is that the numerical tools were extensively tested in this work, showing excellent performance.

In this appendix, the mathematical formulation suggested to the physics behind a magnetic vesicle under shear flow and an external magnetic field is presented. The problem statement is detailed, defining all relevant aspects and variables involved. Then the incompressible Navier-Stokes equations with additional terms that take into account the influence of the inextensible membrane and the magnetic field, are presented. It is necessary to compute the surface tension at the interface necessary to guarantee the membrane's inextensibility. Following, the governing equations are non-dimensionalized and a brief discussion about the influence of vesicles on the viscosity of diluted suspensions is presented. Finally, we present the numerical methodology suggested for the projection method with an additional step to compute the surface tension coefficient needed to ensure membrane inextensibility.

This problem is similar to that presented in the section 2.1 exchanging the droplet for a vesicle, as shown in Figure 42. The vesicle is confined in the region Ω_2 and the continuous phase occupies the region Ω_1, separated by an inextensible membrane Γ. The continuous phase has viscosity η, and magnetic permeability μ_0, which is assumed to be equal to the magnetic permeability of the free space ($\mu_0 = 4\pi \times 10^{-7}\text{H/m}$), while the vesicle, which is placed at the center of the channel, has viscosity $\lambda\eta$ and magnetic permeability $\zeta\mu_0$, where ζ is the permeability ratio between the dispersed and continuous phases. Both phases are assumed to be Newtonian and incompressible and the two-phase fluid can be seen as a diluted suspension of fluids vesicles of the same density ρ, ensuring that the drop remains in the center of the channel. The system is subjected to the same conditions set out in the section 2.1 in addition to an external uniform magnetic field $\mathbf{H}_0$, which is applied either parallel or perpendicular to the plates.

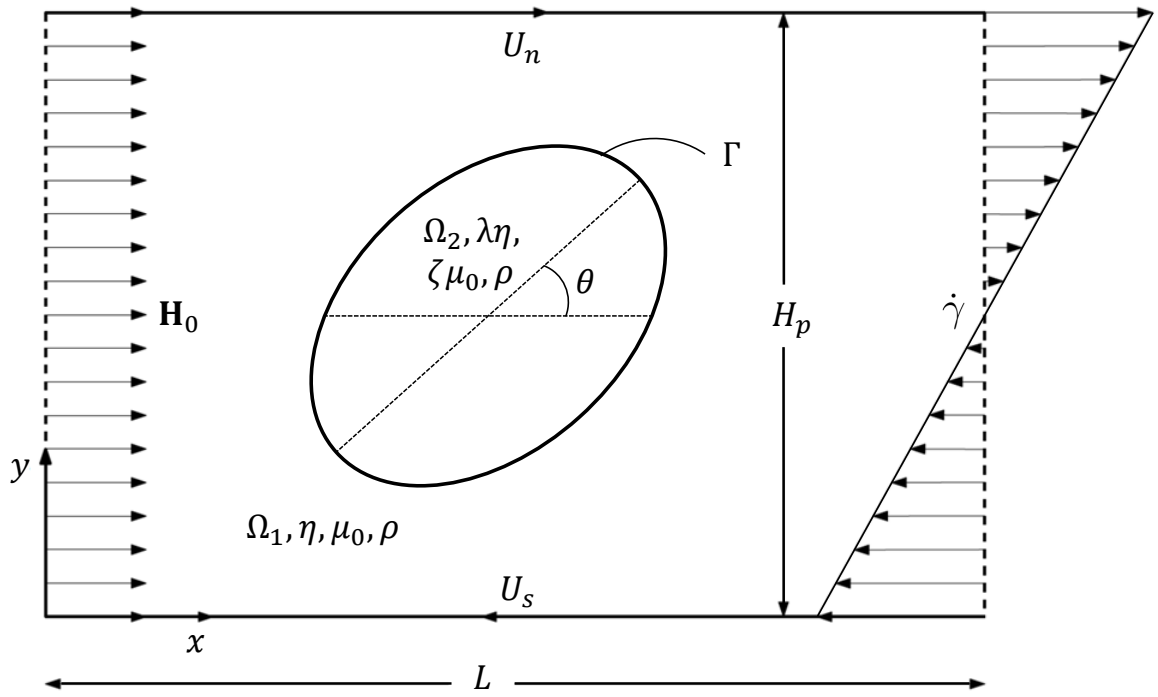

Figure 42 – Schematic illustration of a magnetic vesicle under simple shear flow. Ω_2 corresponds to the vesicle region and Ω_1 corresponds the continuous phase, Γ is the inextensible membrane, η is the continuous phase viscosity, $\lambda\eta$ is the vesicle viscosity, μ_0 is the continuous phase magnetic permeability, $\zeta\mu_0$ is the vesicle magnetic permeability, ρ is the vesicle and continuous phase density, $\dot{\gamma}$ is the shear rate $\dot{\gamma}$, $U_n = \dot{\gamma}H_p/2 = -U_s$ is the canal walls velocity, $\mathbf{H}_0$ is the external uniform magnetic field, H_p is the distance between the channel walls and L is the length of the channel walls.

A.1 Physics formulation

As for surfactant-covered droplets, the governing equations are also the Eqs. (2.2) and (2.3). The difference is the term $\mathbf{F}_s$, which must take into account the membrane inextensibility. Depending on the temperature, and the chemical nature of the surfactants, the molecular organization of the membrane can be of the liquid type, corresponding to a crystal, or even form a gel-like structure. At a mesoscopic scale, the mechanical properties of the membrane can vary from a two-dimensional liquid to an elastic solid (BEAUCOURT et al., 2004). In these conditions, the membrane extensibility is very low and is generally assumed to be inextensible, this assumption is used here.

The response of the vesicle to the external flow will depend on the various forces acting on the vesicle membrane. These forces can be determined by examining the free energy of the closed membrane (HELFRICH, 1973). As described by Salac and Miksis (2011), for the systems of interest, there is not enough energy in the system to change the number of lipids in the membrane or the closed volume, that is, these two quantities are considered fixed for a given vesicle. Thus, starting from the simplest model suggested by Helfrich (1973) since the vesicle is not subjected to topological changes, like budding, the

membrane energy can be modeled by

$$E_H = \frac{b_n}{2} \int_S \kappa^2 dS \tag{A.1}$$

where, b_n is the bending rigidity.

To minimize energy, the restriction of local inextensibility of the membrane is considered using the surface tension, σ, which acts as a Lagrange's multiplier to enforce the membrane inextensibility, as follows:

$$E = \frac{b_n}{2} \int_S \kappa^2 dS + \int_S \sigma(S) dS, \tag{A.2}$$

it is important to note that the first term corresponds to the Helfrich theory and the second term expresses the constraint of fixed area, that is, the absence of local dilatation of the membrane.

Therefore, the response of the fluid in each domain is coupled by conditions imposed on the membrane. Assume continuity of the velocity field and a jump in the hydrodynamic stress, the force per unit area on the membrane can be calculated by taking the variational derivative to the surface energy with respect to a membrane displacement, Eq. (A.2). This procedure is detailed by (KAOUI et al., 2008). Thus, using the Dirac-delta function to enforce these contributions around the interface and level set method leads to

$$\mathbf{F}_s = \delta_\varepsilon(\phi)|\nabla\phi| \left[b_n \left(\nabla_s^2 \kappa + \frac{1}{2}\kappa^3 \right) \mathbf{n} + (\nabla_s \sigma - \kappa\sigma\mathbf{n}) \right], \tag{A.3}$$

or

$$\mathbf{F}_s = \mathbf{F}_b + \mathbf{F}_\sigma, \tag{A.4}$$

where $\mathbf{F}_b$ is the bending force term from the membrane bending rigidity and $\mathbf{F}_\sigma$ is the bending force by removing the portion of the surface force term from the normal and tangential stress jump.

Eq. (A.3) is composed of a normal as well as a tangential contribution. If σ is constant, the tension force associated with σ is tangential to the curve and has the same magnitude at both ends of an arc element $d\Gamma$, presented in Figure 2. Thus, the sum of the two forces is directed in the normal direction. If σ is not constant so the two values at the ends of $d\Gamma$ are different, and the force has, in addition to a normal part, a tangential one, which is given by $\nabla_s\sigma$. On the other hand, the bending energy depends on the curvature, which is a geometric quantity. Logically, the only force that can change the shape of a geometrical surface must be normal to the surface. Finally, the term $-\kappa\sigma\mathbf{n}$ has the same structure as the force due to the surface tension of a drop. However, for a drop σ is an intrinsic quantity that represents the cost in energy for moving a molecule from the bulk to the surface. For vesicles, σ is a Lagrange multiplier that must be determined by requiring a constant local area.

In general, Eq. (A.3) has implicit numerical challenges: the surface Laplacian of curvature, which is a fourth-order derivative on the surface; curvature the third power, which is a non-linear and rapidly changing term in space; and the surface tension term, which, unlike the surfactant problem where the surface tension is a function of the surfactant concentration, given by a state equation, in the case of vesicles this surface tension needs to be calculated to enforce surface incompressibility, modulating it according to the local area restriction, that is, imposing that the time rate of change of a material surface element is 0. Thus, using Eq. (2.19), it is concluded that the velocity at the interface must also be surface-divergence-free,

$$\nabla_s \cdot \mathbf{u} = 0. \tag{A.5}$$

Therefore, replacing Eqs. (A.3), (2.5) in Eq. (2.3), the fluid motion equation is:

$$\begin{aligned} \rho\frac{D\mathbf{u}}{Dt} = &-\nabla p + \nabla\cdot[\lambda(\mathbf{x})\eta(\nabla\mathbf{u}+\nabla\mathbf{u}^T)] + \delta_\varepsilon(\phi)|\nabla\phi|(\nabla_s\sigma - \kappa\sigma\mathbf{n}) \\ &+\delta_\varepsilon(\phi)|\nabla\phi|\left[b_n\left(\nabla_s^2\kappa + \frac{1}{2}\kappa^3\right)\mathbf{n}\right] + \mu_0\left(\zeta_\varepsilon(\phi)-1\right)\mathbf{H}\cdot\nabla\mathbf{H} \end{aligned} \tag{A.6}$$

A.2 Vesicles equations normalization

Consider now a three-dimensional vesicle of enclosed volume V which has a membrane area A_m and the characteristic length defined as $R_0 = \sqrt{A/(4\pi)}$. This vesicle is characterized by a reduced volume parameter, $\nu = V/(4\pi R_0^3/3)$, which relates the encapsulated volume of a vesicle to that of a sphere with the same membrane area. For a sphere $R_0 = a$ and $\nu = 1$. The following dimensionless variables are used: $t^* = t\dot{\gamma}$, $\mathbf{x}^* = \mathbf{x}/R_0$, $\mathbf{u}^* = \mathbf{u}/(\dot{\gamma}R_0)$, $p^* = p/(\rho R_0^2\dot{\gamma}^2)$, $\mathbf{H}^* = \mathbf{H}/\left|\mathbf{H}\right|_0$ and $\sigma^* = \sigma/\sigma_0$, where $\sigma_0 = \rho R_0^3\dot{\gamma}^2$. For convenience, the superscript $*$ is also omitted here. Thus, the dimensionless form of Eqs. (2.2), (A.5) and (A.6) became, respectively,

$$\nabla\cdot\mathbf{u} = 0, \tag{A.7}$$

$$\nabla_s\cdot\mathbf{u} = 0, \tag{A.8}$$

$$\begin{aligned} \frac{D\mathbf{u}}{Dt} = &-\nabla p + \frac{1}{Re}\nabla\cdot[\lambda(\mathbf{x})(\nabla\mathbf{u}+\nabla\mathbf{u}^T)] + \delta_\varepsilon(\phi)|\nabla\phi|(\nabla_s\sigma - \kappa\sigma\mathbf{n}) \\ &+\frac{1}{Ca_{b_n}Re}\delta_\varepsilon(\phi)|\nabla\phi|\left(\nabla_s^2\kappa + \frac{1}{2}\kappa^3\right)\mathbf{n} + \frac{Ca_{bmag}}{Ca_{b_n}Re}\left(\zeta_\varepsilon(\phi)-1\right)\mathbf{H}\cdot\nabla\mathbf{H}, \end{aligned} \tag{A.9}$$

in which the dimensionless groups are:

$$Re = \frac{\rho\dot{\gamma}R_0^2}{\eta}, \quad Ca_{b_n} = \frac{\eta\dot{\gamma}R_0^3}{b_n} \quad \text{and} \quad Ca_{bmag} = \frac{\mu_0 R_0^3|\mathbf{H}_0|^2}{b_n}.$$

where the capillary bending number, Ca_{b_n}, expresses the intensity of the flow compared to the bending forces on the membrane and the magnetic capillary bending number, Ca_{bmag}, expresses the ratio between magnetic and bending forces. The latter differs from the magnetic capillary number presented by Cunha et al. (2018), which corresponds to the ratio between magnetic and capillary forces and is used to study magnetic droplet problems.

A.3 Projection method for magnetic vesicles

For the problem involving magnetic vesicles, an additional step must be added to the projection method to conserve the surface area of the vesicle, determining the surface tension at each time step necessary to impose the area restriction. The general idea of the method is similar to that presented previously, however, there is an additional complication, which is the membrane incompressibility.

As previously mentioned, a major difficulty in solving the Navier-Stokes equations is the application of conditions free of divergences, which in this case are two conditions, Eqs. (A.7), (A.8). As the surfactant problem, in the first step, the trial velocity field, $\mathbf{u}^*$, is computed using the non-linear viscous portion and the contribution from the bending of the membrane to the motion equation, Eq. (A.9), as follows:

$$\begin{aligned}\frac{\mathbf{u}^* - \mathbf{u}^n}{\Delta t} = &-[(\mathbf{u}\cdot\nabla)\mathbf{u}]^{n+1/2} + \frac{1}{Re}\nabla\cdot[\lambda_\varepsilon(\phi)(\nabla\mathbf{u} + \nabla\mathbf{u}^T)]^{n+1/2} \\ &+\frac{\bar{\lambda}}{2Re}\nabla^2\mathbf{u}^* - \frac{\bar{\lambda}}{2Re}\nabla^2\tilde{\mathbf{u}}^{n+1} + \frac{Ca_{bmag}}{Ca_{b_n}Re}\left[(\zeta_\varepsilon(\phi) - 1)\,\mathbf{H}\cdot\nabla\mathbf{H}\right]^{n+1/2} \\ &+\frac{1}{Ca_{b_n}Re}\left[\delta_\varepsilon(\phi)\nabla\phi\left(\nabla_s^2\kappa + \frac{1}{2}\kappa^3\right)\right]^{n+1/2}.\end{aligned} \tag{A.10}$$

where,

$$\frac{\mathbf{u}^{n+1} - \mathbf{u}^*}{\Delta t} = -\nabla\chi^{n+1} + \left[\delta_\varepsilon(\phi)\left(|\nabla\phi|\nabla_s\sigma - \kappa\sigma\nabla\phi\right)\right]^{n+1} \tag{A.11}$$

or, according to the Eq. (A.3), in which $\mathbf{F}_\sigma = \delta_\varepsilon(\phi)\left(|\nabla\phi|\nabla_s\sigma - \kappa\sigma\nabla\phi\right)$,

$$\frac{\mathbf{u}^{n+1} - \mathbf{u}^*}{\Delta t} = -\nabla\chi^{n+1} + \mathbf{F}_\sigma^{n+1}. \tag{A.12}$$

The second step is the standard trial pressure-projection step to enforce the incompressibility of the velocity field, thus applying the divergent operator on the left and right sides of Eq. (A.12). Respecting the condition $\nabla \cdot \mathbf{u}^{n+1} = 0$, it is obtained that

$$\nabla^2 \chi^{n+1} = \nabla \cdot \mathbf{F}_\sigma^{n+1} + \frac{\nabla \cdot \mathbf{u}^*}{\Delta t}. \tag{A.13}$$

Eq. (A.13) is used to compute χ^{n+1}.

In the third step, the Eq. (A.11) is placed into the Eq. (A.10), obtaining the pressure field

$$p^{n+1/2} = \chi^{n+1} - \frac{1}{2Re}\nabla \cdot \mathbf{u}^* \tag{A.14}$$

In addition, the velocity field $\mathbf{u}^{n+1}$, is computed by Eq. (A.12).

The fourth step is the surface area conserving step of the projection method. Thus, the surface divergent operator is applied on the left and right sides of Eq. (A.12), respecting the condition imposed by Eq. (A.8), as follows:

$$\nabla_s \cdot \mathbf{F}_\sigma^{n+1} = \nabla_s \cdot \nabla \chi^{n+1} - \frac{\nabla_s \cdot \mathbf{u}^*}{\Delta t}. \tag{A.15}$$

Assuming that the level set field is maintained as a signed distance function, thus $|\nabla \phi| = 1$, Eq. (A.15) is simplified by obtaining an equation that determines the surface tension following the membrane's inextensibility restrictions,

$$\nabla_s^2 \sigma^{n+1} - \kappa^2 \sigma^{n+1} = \frac{1}{\delta(0)} \nabla_s \cdot \left(\nabla \chi^{n+1} - \frac{\mathbf{u}^*}{\Delta t} \right). \tag{A.16}$$

This equation is only valid on the interface and therefore must be solved using the closest point method to discretize it, and the Bi-conjugate gradient stabilized method to solve the linear system.

Therefore, the flow governing equations are solved in the following order:

- Eq. (A.10) to compute the trial velocity field, $\mathbf{u}^*$;
- Eq. (A.13) to compute the trial pressure field, χ^{n+1}, and Eq. (A.16) to compute σ^{n+1} on the surface. This equations are directly linked, because Eq. (A.16) is function of σ^{n+1} and Eq. (A.13) is function of χ^{n+1}. Thus, this equations are solved iteratively until the residual of both equation are less than 10^{-9} in the same iteration;
- Eq. (A.12) to compute velocity field, $\mathbf{u}^{n+1}$;
- Eq. (A.14) to compute pressure field, $p^{n+1/2}$.

A.4 Implementation difficulties/suggestions

The described methodology was implemented and tested, however, the initial tests showed problems related to the membrane length conservation, which starts to increase after a certain point (depending on the parameters tested). Although the governing equations have been successfully solved, the condition $\nabla_s \cdot \mathbf{u} = 0$ has not been satisfied. This is somewhat intriguing, since Eqs. (A.13) and (A.16) are resolved interactively.

The re-initialization process has contributed to the membrane length increase, being directly affected by the number of re-initialization steps. We are still not sure how this has happened, but we believe that since ϕ directly affects the closest point chosen in the linear system solution, this has cumulatively affected our results since the errors become more evident as where time increases. For this, we suggest using a more elaborate method for determining the closest point, which uses the current method as "kick" to determine it more precisely.

In addition, we found that rising the numerical width of the interface from $3/2h$ to $3h$ makes a significant difference in the area (length) conservation. It seems that having more points in the normal direction of the surface improves the numerical results. We also observed that when our vesicles reach a stationary shape (in tank treading), the area and length start to increase faster, another indication that the re-initialization has failed.

It is already known that in the absence of a magnetic field and viscosity ratio $\lambda > 1$, the vesicle begins to tip end to end in a rigid manner, following the tumbling motion pattern, with the inclination angle suffering periodic repetitions of 0 to 180°. By solving the aforementioned problems, it is expected that as the magnetic field force is increased, the vesicle fails to follow the tumbling pattern, reaching a balance in the inclination angle of the tank-treading regime. For this, it is also necessary to evaluate the variation of the angle of equilibrium of the vesicle in relation to the time. If it remains constant over time, it means that the movement will occur in the tank-treading pattern and it will be possible to control the pattern of movement of the vesicle.

As the rheology of a vesicle suspension is directly influenced by the vesicle motion pattern (GHIGLIOTTI; BIBEN; MISBAH, 2010), it is expected that under the action of a magnetic field, it is possible to control the suspension rheology. For example, considering a vesicles suspension in which the tumbling motion pattern is observed, it is expected that the sudden application of a magnetic field (parallel or perpendicular to the main flow direction) will result in the abrupt change in the vesicles motion pattern, tumbling to tank-treading, also changing the rheological properties of the suspension.

Annex

A - Direct solution via Fourier Analysis

For brevity, only a two-dimensional deduction from the solver is presented here, where i is reserved to represent the imaginary unit. A more detailed approach can be found in the work of (ABICALIL, 2021). Thus, a general linear system of equations, arising from a finite difference discretization of the 2D governing equations, can be written in a stenciled form as:

$$a_{p,q}u_{p-1,q} + b_{p,q}u_{p,q-1} + c_{p,q}u_{p,q} + d_{p,q}u_{p+1,q} + e_{p,q}u_{p,q+1} - f_{p,q} = 0, \tag{A.1}$$

for $p = [1, P]$, $q = [1, Q]$, where the discrete inverse Fourier transform, in one direction, is defined as

$$u_p = \frac{1}{M}\sum_{m=0}^{M-1} \hat{u}_m e^{i\frac{2\pi}{M}mp}, \tag{A.2}$$

with $M = P$.

Applying the inverse Fourier transform in the x direction to Eq. (A.1), and assuming that all coefficients (a, b, c, d, e) are constant in the transformation direction, we have

$$\begin{aligned} &\frac{1}{M}\sum_{m=0}^{M-1}\Big(a_q\hat{u}_{m,q}e^{i\frac{2\pi}{M}m(p-1)} + b_q\hat{u}_{m,q-1}e^{i\frac{2\pi}{M}mp} + c_q\hat{u}_{m,q}e^{i\frac{2\pi}{M}mp} \\ +\quad &d_q\hat{u}_{m,q}e^{i\frac{2\pi}{M}m(p+1)} + e_q\hat{u}_{m,q+1}e^{i\frac{2\pi}{M}mp} - \hat{f}_{m,q}e^{i\frac{2\pi}{M}mp}\Big) = 0. \end{aligned} \tag{A.3}$$

Thus, for $m = [0, M-1]$, $q = [1, Q]$

$$\begin{aligned} &a_q\hat{u}_{m,q}e^{i\frac{2\pi}{M}m(p-1)} + b_q\hat{u}_{m,q-1}e^{i\frac{2\pi}{M}mp} + c_q\hat{u}_{m,q}e^{i\frac{2\pi}{M}mp} \\ +\quad &d_q\hat{u}_{m,q}e^{i\frac{2\pi}{M}m(p+1)} + e_q\hat{u}_{m,q+1}e^{i\frac{2\pi}{M}mp} = \hat{f}_{m,q}e^{i\frac{2\pi}{M}mp} \end{aligned} \tag{A.4}$$

Splitting the exponential functions in the terms containing a_q and d_q, respectively,

$$\begin{aligned} e^{i\frac{2\pi}{M}m(p-1)} &= e^{i\frac{2\pi}{M}mp}e^{-i\frac{2\pi}{M}m}, \\ e^{i\frac{2\pi}{M}m(p+1)} &= e^{i\frac{2\pi}{M}mp}e^{i\frac{2\pi}{M}m}. \end{aligned} \tag{A.5}$$

By imposing that $a_q = d_q$, we have

$$a_q \hat{u}_{m,q} e^{i\frac{2\pi}{M}m(p-1)} + d_q \hat{u}_{m,q} e^{i\frac{2\pi}{M}m(p+1)} = a_q \hat{u}_{m,q} e^{i\frac{2\pi}{M}mp} \left(e^{-i\frac{2\pi}{M}m} + e^{i\frac{2\pi}{M}m} \right). \tag{A.6}$$

Finally, using Euler's equation and recalling that cosines and sines are even and odd functions, respectively, we find

$$e^{-i\frac{2\pi}{M}m} + e^{i\frac{2\pi}{M}m} = 2\cos\left(\frac{2\pi}{M}m\right). \tag{A.7}$$

Substituting Eq. (A.7) in Eq. (A.6),

$$a_q \hat{u}_{m,q} e^{i\frac{2\pi}{M}m(p-1)} + d_q \hat{u}_{m,q} e^{i\frac{2\pi}{M}m(p+1)} = 2a_q \cos\left(\frac{2\pi}{M}m\right) \hat{u}_{m,q} e^{i\frac{2\pi}{M}mp}. \tag{A.8}$$

Now, substituting this result in Eq. (A.4), we find that

$$e^{i\frac{2\pi}{M}m} \left(2a_q \cos\left(\frac{2\pi}{M}m\right) \hat{u}_{m,q} + b_q \hat{u}_{m,q-1} + c_q \hat{u}_{m,q} + e_q \hat{u}_{m,q+1} \right) = \hat{f}_{m,q} e^{i\frac{2\pi}{M}mp} \tag{A.9}$$

Therefore, the original system of equations is reduced to the following set of tridiagonal systems of equations:

$$b_q \hat{u}_{m,q-1} + \left(2a_q \cos\left(\frac{2\pi}{M}m\right) + c_q \right) \hat{u}_{m,q} + e_q \hat{u}_{m,q+1} = \hat{f}_{m,q}. \tag{A.10}$$

In order to solve the above tridiagonal system of equations, we use the following methods (ABICALIL, 2021):

1. Apply a Fourier transform in the y direction, in a similar way to what was previously described, with similar restrictions to the coefficients. This reduces the problem to a set of diagonal systems of equations, with trivial solutions;
2. Solve the system by using Thomas' algorithm for tridiagonal matrices, which is a simplified form of Gaussian elimination. This alternative is more efficient than employing an additional Fourier transform and doesn't impose such strict restrictions on the coefficients of the linear system.

As such, the solution process of the method described above is:

1. Apply a Fourier transform in the x direction to the right-hand side of Eq. (A.1);
2. Solve the M tridiagonal systems described in Eq. (A.10), in order to determine the values of $\hat{u}$;
3. Apply an inverse Fourier transform in the x direction to $\hat{u}$, in order to determine the values of the original unknowns u.

B - Biconjugate gradient method

The Biconjugate Gradient Stabilized method was developed to solve non-symmetric linear systems, avoiding the often irregular convergence patterns of the conjugate gradient squared method (VORST, 1992). Thus, a linear system $A\mathbf{x} = \mathbf{b}$ is solved by the steps presented in Algorithm 1.

Algorithm 1 : Biconjugate Gradient Stabilized method

1 : Compute $\mathbf{r}_0 = \mathbf{b} - A\mathbf{x}_0$, choose $\mathbf{r}'_0$ such that $\mathbf{r}_0 \cdot \mathbf{r}'_0 \neq 0$
2 : Set $\mathbf{p}_0 = \mathbf{r}_0$
3 : **for** $j = 0, 1, ...$ **do**
4 : $\quad \alpha_j = (\mathbf{r}_j \cdot \mathbf{r}'_0)/((A\mathbf{p}_j) \cdot \mathbf{r}'_0)$
5 : $\quad \mathbf{s}_j = \mathbf{r}_j - \alpha_j A\mathbf{p}_j$
6 : $\quad \omega_j = ((A\mathbf{s}_j) \cdot \mathbf{s}_j)/((A\mathbf{s}_j) \cdot (A\mathbf{s}_j))$
7 : $\quad \mathbf{x}_{j+1} = \mathbf{x}_j + \alpha_j \mathbf{p}_j + \omega_j \mathbf{s}_j$
8 : $\quad \mathbf{r}_{j+1} = \mathbf{s}_j - \omega_j A\mathbf{s}_j$
9 : $\quad$ **if** $||\mathbf{r}_{j+1}|| < \varepsilon_0$ **then**
10: $\quad\quad$ Break;
11: $\quad$ **end if**
12: $\quad \beta_j = (\alpha_j/\omega_j) \times (\mathbf{r}_{j+1} \cdot \mathbf{r}'_0)/(\mathbf{r}_j \cdot \mathbf{r}'_0)$
13: $\quad \mathbf{p}_{j+1} = \mathbf{r}_{j+1} + \beta_j(\mathbf{p}_j - \omega_j A\mathbf{p}_j)$
14: **end for**
15: Set $\mathbf{x} = \mathbf{x}_{j+1}$